学位論文（要約）

A Study of Non-Inductive Plasma Current Start-Up Using the Lower Hybrid Wave in the TST-2 Spherical Tokamak

（TST-2 球状トカマクにおける低域混成波を用いた非誘導プラズマ電流立ち上げに関する研究）

平成 25 年 12 月　博士（理学）申請

東京大学大学院理学系研究科
物理学専攻
若月　琢馬

Doctoral Thesis

A Study of Non-Inductive Plasma Current Start-Up Using the Lower Hybrid Wave in the TST-2 Spherical Tokamak

Takuma Wakatsuki

Department of Physics, Graduate School of Science
The University of Tokyo

December 19, 2013

Abstract

Radio frequency (RF) waves are used in many tokamak experiments for heating, current drive, and plasma start-up. RF and other non-inductive techniques play more important roles in spherical tokamaks (STs) compared to conventional tokamaks, because of the crucial need for eliminating the central solenoid. In conventional tokamaks, the lower hybrid wave (LHW) has demonstrated high efficiency for driving current [1]. Plasma start-up and current ramp-up to 100 kA has also been achieved [2]. Waves in spherical tokamak plasmas behave very differently from those in conventional tokamak plasmas because of very high dielectric constants ($\sim \omega_{\mathrm{pe}}^2/\Omega_{\mathrm{e}}^2$) associated with the ability of the ST to confine high density plasmas at low magnetic fields. Although a deterioration of the current drive efficiency of the LHW is known to occur at high densities [3, 4], an effective current drive should be possible if the LHW is utilized keeping the density low during the plasma current ramp-up phase. Therefore, in this thesis, the feasibility of plasma current start-up and ramp-up by the LHW to a sufficient level needed for further heating is investigated.

The 200 MHz RF power was utilized to excite the LHW in TST-2. This frequency is one order of magnitude lower compared with typical frequencies utilized for LHW in conventional tokamaks. Three types of antennas with distinctive features were used in this thesis: the (inductively-coupled) combline antenna, the dielectric-loaded waveguide array antenna (a.k.a. grill antenna), and the electrostatically-coupled combline antenna (ECC antenna).

Initial plasma start-up and plasma current ramp-up to 15 kA were achieved by the combline antenna but the current drive efficiency was lower than other antennas. The current drive efficiency could be improved by using the grill antenna and the ECC antenna which can excite the LHW with suitable polarization efficiently. The ability of the grill antenna to excite the LHW with different $n_{\parallel} = ck_{\parallel}/\omega$ was used to identify the most favorable $n_{\parallel}$ spectrum for plasma current ramp-up. It was found that effective current drive can be achieved by the LHW with $n_{\parallel}$ less than 6. However, even in this case, the energetic electrons which account for a large fraction of the driven current,

are lost rapidly because the poloidal field generated by the plasma current is not sufficient to confine these electrons.

The antenna-plasma coupling of the grill antenna deteriorates as the input power exceeds several kW. It was found that this is a consequence of the density depletion due to the ponderomotive force. The ECC antenna overcame this problem because the coupling characteristics of this antenna are not as sensitive as the grill antenna. The highest current drive figure of merit was achieved using the ECC antenna. This is because the ECC antenna can launch the LHW with better defined traveling wave spectrum than the grill antenna.

Contents

List of Figures

List of Tables

Chapter 1

Introduction

1.1 Nuclear Fusion

Nuclear fusion is the reaction which occurs in the sun to produce energy. It is a reaction in which nuclei with small masses fuse to form a heavier nucleus. When this reaction occurs, a large amount of energy, equal to the mass defect ($E = \Delta mc^2$), is released.

The fusion reactor utilizes this reaction [5, 6]. The fuel for the fusion reactor is a mixture of deuterium (D) and tritium (T), and the main reaction which produces energy is (cf. Fig.1.1)

$$\mathrm{D} \ + \ \mathrm{T} \ \rightarrow \ {}^{4}\mathrm{He}\ (3.52\ \mathrm{MeV}) \ + \ \mathrm{n}\ (14.06\ \mathrm{MeV}). \tag{1.1}$$

There are several advantages of nuclear fusion. The first advantage is that the fuel is virtually inexhaustible and ubiquitous. The second advantage is the capability of producing massive amounts of energy because of its high energy density. The third advantage is inherent safety, because runaway reactions can never occur in a fusion reactor.

In order to utilize nuclear fusion as a source of energy, fusion reaction must occur continuously. The nuclei repel each other because of the Coulomb force. Therefore, only nuclei with sufficient kinetic energy can come into close contact and induce the fusion reaction. The fusion reaction rate can be increases by confining a plasma with high temperature and density. When sufficient reaction rate is achieved, the plasma can be heated by the fusion reaction itself, and the reaction can continue. This state is called ignition.

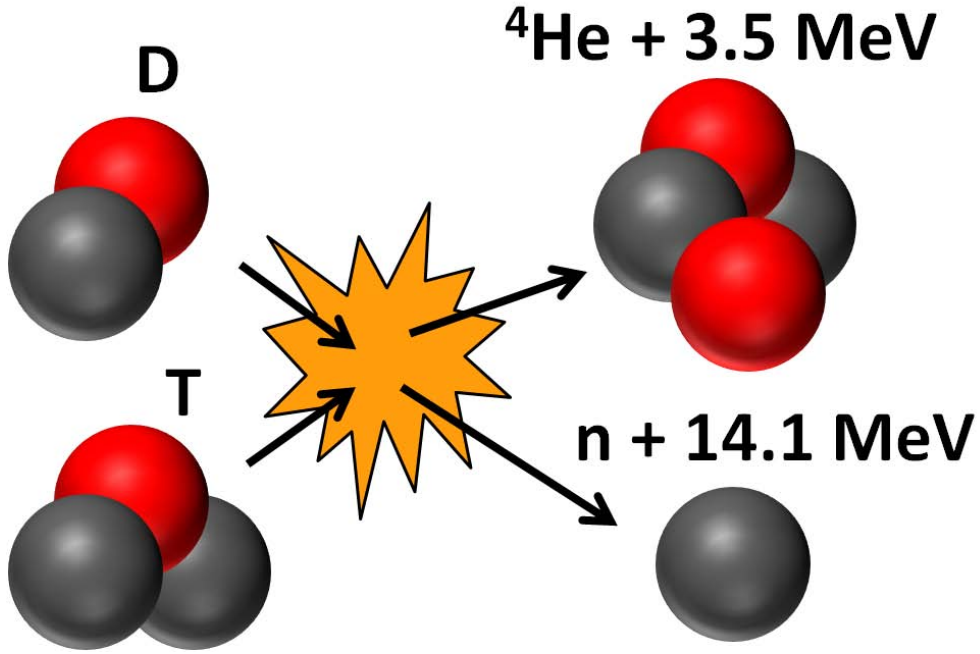

Figure 1.1: D-T fusion reaction.

1.2 Tokamak

The most general method to achieve plasma confinement is to use the magnetic field. The tokamak is the most successful magnetic confinement concept named after Russian "torodailnaya kamera magnitmaya" which means toroidal magnetic container [7, 8].

Charged particles gyrate around a magnetic field line. Therefore, a rapid loss of plasma is prevented by making a toroidal configuration of magnetic field. However, in a simple toroidal configuration with the magnetic field only in the toroidal direction, ions and electrons drift in vertically in opposite directions, and the resultant electric field induces an outward drift of both ions and electrons, and the plasma is lost quickly. When the plasma current flows through the torus in the toroidal direction, the poloidal magnetic field is generated. The addition of this field forms a toroidal surface covered by helical magnetic field lines, and the charge separation is cancelled. This is the fundamental concept of the tokamak.

In the conventional tokamak, the plasma current is induced by the air-core transformer coil threading through the central hole of the torus. This coil is called the central solenoid (CS). When the current is induced in the plasma by the transformer effect, the plasma is heated by Joule heating. However, as the plasma temperature becomes higher, the electrical resistance of the plasma decreases, and the plasma heating efficiency decreases. In order to achieve a fusion relevant temperature, some other form of heating (auxiliary heating) is needed. Two main methods of auxiliary heating are the neutral beam injection (NBI) and radio frequency (RF) wave heating.

1.3 Spherical Tokamak

The spherical tokamak (ST) is a tokamak with a very small aspect ratio (the ratio of the major radius to the minor radius of the torus), typically $A < 2$. It is sometimes referred to as the spherical torus. The plasma becomes magnethydrodynamically (MHD) stable when the magnetic field curvature points toward the plasma. Therefore, the ST plasma is more MHD stable than the conventional tokamak plasma because the dominant field lines have good curvature on the inboard side of the torus for ST. As a result, the ST has a potential of confining a high pressure plasma with moderate magnetic field strength. In other words, high β plasma can be confined stably (where β is the ratio of the plasma kinetic pressure to the pressure of the confining magnetic field). The ST has the potential of achieving high power densities taking advantage of its high β capability [9–11]. However, it is preferable to

avoid inductive current drive by the CS in fusion applications which require inboard wall shielding against fusion-produced neutrons. Therefore, the establishment of non-inductive plasma start-up and plasma current ramp-up scenarios is the main issue for the future of the ST.

1.4 Fundamentals of Plasma Physics

1.4.1 Definition of the Plasma

The plasma is an ionized gas. When the gas is heated up, the atoms collide with each other and their electrons are stripped. This state is called the plasma, "the fourth state of matter" following the solid, liquid and gas. The plasma has a very high electric conductivity, because the electrons can stream freely with very rare Coulomb collisions. The high electric conductivity results in the shielding of the electric field in the plasma. This is called Debye shielding [12]. Consider the plasma which obeys the Maxwell-Boltzmann distribution function in the electrostatic potential $\phi = \phi_0$ at $x = 0$ and $\phi = 0$ at $x = \infty$. The electron and ion densities can be written as

$$n_{\mathrm{e}}(x) = n_{\mathrm{e}\infty} \exp(e\phi/T_{\mathrm{e}}) \tag{1.2}$$

$$Zn_{\mathrm{i}}(x) = n_{\mathrm{e}\infty} \exp(-eZ\phi/T_{\mathrm{i}}), \tag{1.3}$$

where $n_{\mathrm{e}\infty}$ is the electron density at $x = \infty$, e is the electron charge, Z is the ion charge number and $T_{\mathrm{e,i}}$ are the electron and ion temperatures, respectively. The Poisson equation can be written as

$$\epsilon_0 \frac{\mathrm{d}^2\phi}{\mathrm{d}x^2} = e(n_{\mathrm{e}} - Zn_{\mathrm{i}}) = en_{\mathrm{e}\infty}[\exp(e\phi/T_{\mathrm{e}}) - \exp(-eZ\phi/T_{\mathrm{i}})], \tag{1.4}$$

where ϵ_0 is the permittivity of vacuum. If we assume that $e\phi \leq T$, the exponential term can be expanded and Eq. (1.4) becomes

$$\frac{\mathrm{d}^2\phi}{\mathrm{d}x^2} = \frac{e^2 n_{\mathrm{e}\infty}(1 + ZT_{\mathrm{e}}/T_{\mathrm{i}})}{\epsilon_0 T_{\mathrm{e}}}\phi. \tag{1.5}$$

This equation can be solved easily to give

$$\phi(x) = \phi_0 \exp(-x/\lambda_{\mathrm{D}}), \tag{1.6}$$

where

$$\lambda_{\mathrm{D}} = \left(\frac{\epsilon_0 T_{\mathrm{e}}}{n_{\mathrm{e}} e^2 (1 + ZT_{\mathrm{e}}/T_{\mathrm{i}})}\right)^{1/2}. \tag{1.7}$$

Therefore, the electrostatic potential is shielded in a characteristic length λ_{D}. As a result, quasi-neutrality is usually satisfied in the plasma for distances greater than λ_{D} in equilibrium.

1.4.2 Single Particle Motion in the Plasma

Guiding Center Theory

Consider a uniform magnetic field along the z-direction, $\boldsymbol{B_0} = B_0\hat{\boldsymbol{z}}$. The equation of motion of a charged particle is described by

$$m\frac{\mathrm{d}\boldsymbol{v}}{\mathrm{d}t} = q\left(\boldsymbol{E} + \boldsymbol{v}\times\boldsymbol{B_0}\right), \tag{1.8}$$

where m, $\boldsymbol{v}$ and q are the mass, the velocity and the charge of the particle, respectively. Defining the cyclotron angular frequency as $\Omega_\mathrm{c} = qB/m$ and the velocity parallel and perpendicular to the magnetic field as $v_\parallel = v_{z0}$ and $v_\perp = \sqrt{v_{x0}^2 + v_{y0}^2}$, the time evolution of the position of the particle can be described as

$$x = x_0 - i(v_\perp/\Omega_\mathrm{c})\exp(i\Omega_\mathrm{c}t) \tag{1.9}$$

$$y = y_0 + (v_\perp/\Omega_\mathrm{c})\exp(i\Omega_\mathrm{c}t) \tag{1.10}$$

$$z = z_0 + v_\parallel t. \tag{1.11}$$

Therefore, the motion of a charged particle can be separated into perpendicular gyrating motion with radius $\rho_\mathrm{L} = mv_\perp/qB$, called the Larmor radius, and the parallel translational motion of the center of the gyrating motion, which is called the guiding center.

The velocity of the guiding center motion of a charged particle in a non-uniform magnetic field can be described as the sum of the parallel velocity and the drift velocity

$$\boldsymbol{v}_\mathrm{d} = -\frac{v_\parallel^2 + v_\perp^2/2}{\Omega_\mathrm{c}}\frac{\boldsymbol{R}_\mathrm{c}\times\boldsymbol{B}}{R_\mathrm{c}^2 B}, \tag{1.12}$$

where $\boldsymbol{R}_\mathrm{c}$ is the radius of curvature vector which is drawn from the local center of curvature to the field line.

Considering the conservation of magnetic moment μ of the gyrating motion, the perpendicular velocity can be expressed as

$$v_\perp^2 = 2\mu B/m. \tag{1.13}$$

In addition, energy conservation gives the differential equation that the parallel velocity must obey,

$$m\frac{\mathrm{d}v_\parallel}{\mathrm{d}t} = -\mu\frac{\partial B}{\partial l}, \tag{1.14}$$

where $\partial/\partial l$ is the derivative along the field line.

Trapped Particle Orbit

As can be seen from Eq. (1.14), the parallel velocity decreases as the particle moves to a higher magnetic field region. In the tokamak, the magnetic field is higher on the inboard side of the torus. Therefore, particles with small $v_{\parallel}$ compared with $v_{\perp}$ are reflected back at a certain major radius and forms an orbit called the banana orbit. This name comes from the shape of the poloidal projection of the orbit. The width of this orbit can be expressed as

$$\Delta_{\mathrm{B}} = q(r)\rho_{\mathrm{L}}A^{1/2} \tag{1.15}$$

where $q(r) \sim rB_{\phi}/RB_{\theta}$ is the safety factor and A is the aspect ratio.

1.4.3 Coulomb Collisions

In fusion plasmas, ions can usually be assumed static compared with electrons because of their heavier mass. Here, we consider an electron colliding with a static ion. The relationship between the impact parameter b and the scattering angle θ is given by the well-known Coulomb scattering formula,

$$\tan\frac{\theta}{2} = \frac{Ze^2}{4\pi\epsilon_0 m v^2 b}. \tag{1.16}$$

The impact parameter corresponding to the 90° scattering is calculated from Eq. (1.16) as

$$b_0 = \frac{Ze^2}{4\pi\epsilon_0 m v^2}. \tag{1.17}$$

From these equations, the change in the velocity perpendicular to the initial velocity can be expressed as,

$$\Delta v_{\perp} = v\sin\theta = \frac{2vb/b_0}{1+(b/b_0)^2}. \tag{1.18}$$

Therefore, as a result of accumulated Coulomb collisions in the plasma whose ion density is n_{i}, the square of the perpendicular velocity changes at the rate

$$\begin{aligned}
\frac{\mathrm{d}\langle(\Delta v_{\perp})^2\rangle}{\mathrm{d}t} &= 2\pi n_{\mathrm{i}} v \int_0^{b_{\max}} (\Delta v_{\perp})^2 b\,db \\
&= 8\pi n_{\mathrm{i}} v^3 \int_0^{b_{\max}} \frac{(b/b_0)^2 b\,db}{[1+(b/b_0)^2]^2} \\
&= 4\pi n_{\mathrm{i}} v^3 b_0^2 \left\{ \ln\left[1+\left(\frac{b_{\max}}{b_0}\right)^2\right] + \frac{1}{1+(b_{\max}/b_0)^2} - 1 \right\},
\end{aligned} \tag{1.19}$$

where $b_{\max}$ is the upper limit of the impact parameter which is introduced to avoid a logarithmic divergence of the integral. In most plasmas we are interested in, the ratio of $b_{\max}$ to b_0 is very large,

$$\Lambda = b_{\max}/b_0 \gg 1. \tag{1.20}$$

In this limit, Eq. (1.19) can be written as

$$\frac{\mathrm{d}\langle(\Delta v_\perp)^2\rangle}{\mathrm{d}t} = 8\pi n_\mathrm{i} v^3 b_0^2 \ln\Lambda = \frac{n_\mathrm{i} Z^2 e^4 \ln\Lambda}{2\pi\epsilon_0^2 m^2 v}. \tag{1.21}$$

Considering energy conservation, $(v+\Delta v_\parallel)^2 + (\Delta v_\perp)^2 = v^2$, we obtain

$$\frac{\mathrm{d}\langle\Delta v_\parallel\rangle}{\mathrm{d}t} = -\frac{1}{2v}\frac{\mathrm{d}\langle(\Delta v_\perp)^2\rangle}{\mathrm{d}t} = \frac{n_\mathrm{i} Z^2 e^4 \ln\Lambda}{4\pi\epsilon_0^2 m^2 v^2}. \tag{1.22}$$

From this relationship, we can define the electron-ion collision frequency ν_ei for loss of electron momentum as

$$\frac{\mathrm{d}\langle\Delta v_\parallel\rangle}{\mathrm{d}t} = -\nu_\mathrm{ei} v, \tag{1.23}$$

Therefore the collision frequency between electron and ion can be described as

$$\nu_\mathrm{ei} = \frac{n_\mathrm{i} Z^2 e^4 \ln\Lambda}{4\pi\epsilon_0^2 m^2 v^3}. \tag{1.24}$$

The collision frequency is inversely proportional to the cube of the electron velocity. It means that faster electrons take longer to slow down.

1.5 Review of Previous Experiments

1.5.1 Review of Lower Hybrid Wave Experiments in Conventional Tokamaks

The dispersion relation and the accessibility of the lower hybrid wave (LHW) were confirmed by Bellan and Porkolab in 1975 [13]. In this experiment, the LHW was excited by a slow wave structure. The wavelength perpendicular to the magnetic field was measured by a movable RF probe. The LHW was originally used for ion heating. When the frequency of the wave is such that the mode conversion layer (close to the lower hybrid resonance layer) is located inside the plasma, the LHW converts to the short-wavelength ion plasma wave and is absorbed by ions. On the other hand, the LHW with

frequency higher than the lower hybrid resonance frequency (typically by a factor of two or greater) does not interact with ions. When the phase velocity of the LHW is comparable to the electron thermal speed, the wave is absorbed by electrons through Landau damping. Electron heating is generally observed in current drive experiments. A uni-directional LHW has demonstrated high current drive efficiency in conventional tokamaks, such as PLT [1], ASDEX [14], WT-II [15, 16], WT-III [17], Alcator C [18], Alcator C-mod [19], Tore Supra [20], JT60-U [21], JET [22]. Plasma start-up and current ramp-up to 100 kA was achieved in PLT [2] In this experiment, X-ray measurements revealed that the fast electrons produced by Landau damping of the LHW were responsible for the driven current. However, degradations of the current drive efficiency associated with the increase of the density or the decrease of the magnetic field strength were reported in Alcator C [18] and PLT [23].

1.5.2 Review of Plasma Start-up Experiments on STs

LATE

Plasma start-up studies using the electron cyclotron wave (ECW, 2.45 GHz/30 kW, 5.0 GHz/200 kW) are performed in LATE at Kyoto University [24–28]. The major and minor radii are 0.20 m and 0.14 m, respectively. Although the ECW accelerates electrons perpendicularly to the background magnetic field, the plasma current is driven by the tangentially injected ECW. This mechanism was revealed by Fisch and Boozer in 1980 [29]. Plasma current start-up to 20 kA has been demonstrated by 180 kW ECW.

UTST

On UTST at the University of Tokyo, plasma start-up by plasma merging is studied. The major and minor radii are 0.43 m and 0.17 m. The merging method used on UTST is called double-null merging (DNM), which uses external poloidal field (PF) coils for plasma start-up [30]. First, two poloidal field null regions are generated in the upper and lower formation regions of the vessel by two pairs of PF coils. After the initial plasmas are generated at the two null regions, PF coil currents are inverted, and the plasmas are pushed towards the midplane. Strong ion heating is achieved through magnetic reconnection by converting the magnetic energy to the ion kinetic energy, and high β plasmas are generated. Plasma start-up to 50 kA has been achieved in 0.5 ms without CS induction [31, 32].

NSTX

Plasma start-up experiments without the CS are also performed in larger STs, NSTX at Princeton Plasma Physics Laboratory (US) and MAST at Culham Centre for Fusion Energy (UK). NSTX utilizes transient coaxial helicity injection (CHI) to start and ramp up the plasma current [33–36]. The CHI discharge starts with the breakdown across the insulated gap of the lower divertor plates. The PF coil located near this gap connects the field lines between the inner and outer coaxial rings of the divertor plates, and after a delay a voltage is applied across this gap. With appropriate gas pressure, breakdown starts and the current flows across this gap. As this injector current increases, the electromagnetic $J_{\rm pol} \times B_{\rm tor}$ force overcomes the field line tension and the field lines start to extend into the vacuum vessel. After the plasma fills the vacuum vessel, if the injector current is reduced rapidly and the field lines are disconnected from the injector, a closed field line configuration with toroidal plasma current is formed. Plasma currents of up to 200 kA has been achieved by this technique.

MAST

Plasma start-up using another RF wave is investigated on MAST [37, 38]. Typical densities of the plasma produced on MAST are too high for ECW in ordinary mode (O-mode) or extraordinary mode (X-mode) to propagate. Such a plasma is called the overdense plasma. There is a propagating mode in the overdense plasma, which is called the electron Bernstein wave (EBW) [39]. This is an electrostatic wave associated with the coherent gyrating motion of the electrons and propagates perpendicular to the magnetic field. Since the EBW cannot be excited directly by an antenna, the O-X-B mode conversion scenario is employed. The O-mode ECW launched from the low field side of the tokamak propagates through the plasma to encounter the grooved mirror-polarizer placed on the center rod (inboard wall of the vacuum vessel). The polarization of the wave changes to the X-mode upon reflection. The X-mode ECW propagates to the mode conversion layer located inside the plasma. The ECW is reflected back at this layer and is converted to the EBW. The EBW then propagates to the electron cyclotron resonance layer and is strongly damped. Plasma start-up to 33 kA using 100 kW RF power at 28 GHz has been demonstrated.

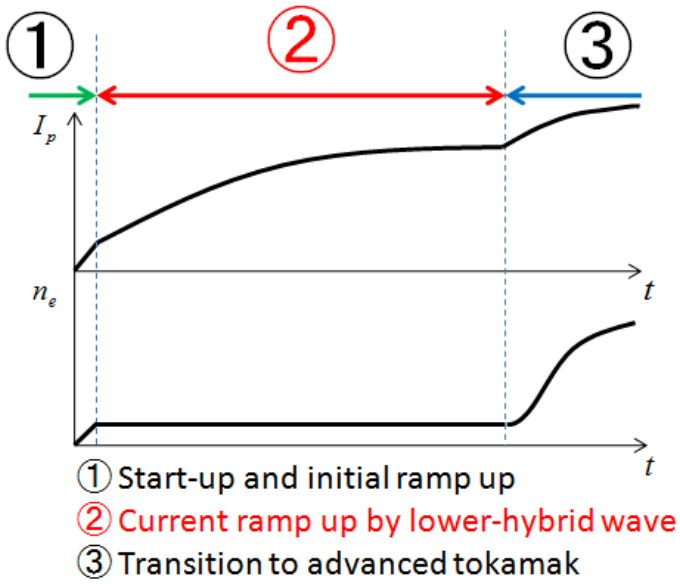

Figure 1.2: A schematic diagram of the plasma start-up scenario using the LHW.

1.6 Thesis Objectives

The development of a plasma current start-up scenario without CS induction is essential for a reactor grade burning ST device. We utilize the LHW, which is known to have a high current drive efficiency in conventional tokamaks, for current drive in ST. Although a deterioration of the current drive efficiency by the LHW is known to occur in high density plasmas, such as those produced in the ST [3,4], effective current drive may be possible if the LHW is utilized in the plasma start-up phase, if the density could be kept low. In this thesis, the feasibility of plasma current start-up and ramp-up by the LHW to a sufficient level needed for further heating (such as by NBI) is investigated. Fig. 1.2 shows a schematic diagram of the scenario we try to demonstrate.

Once heating of a high density plasma by NBI becomes effective, the self-generated current, which is called the bootstrap current [40, 41], becomes significant [42]. For the ST reactor, a large fraction of the plasma current should be driven by the bootstrap current for economic competitiveness. This kind of operation is called the advanced tokamak scenario. This research aims at the demonstration of a plasma current start-up technique needed for the achievement of the advanced tokamak operation in ST without the CS.

The experiments reported in this thesis were performed on the Tokyo

Spherical Tokamak-2 (TST-2) device. In TST-2, plasma start-up by RF power at 200 MHz is being investigated. The RF wave was excited by three types of antennas: the (inductively-coupled) combline antenna, the dielectric-loaded waveguide array antenna (grill antenna) and the electrostatically-coupled combline antenna (ECC antenna).

Chapter 2

Theory of Plasma Waves

Historically, waves over a very wide frequency range have been used to heat plasmas and drive current in plasmas. In this thesis, the lower hybrid wave (LHW) is used. In order to investigate the characteristics of these waves, dispersion relations are derived.

2.1 Waves in a Cold Plasma

First, the plasma is assumed to have zero temperature (i.e., cold plasma approximation). The cold plasma model can describe many important waves including the fast wave (FW) and LHW. The wave equation is derived by combining the following two Maxwell's equations,

$$\nabla \times \boldsymbol{E} = -\frac{\partial \boldsymbol{B}}{\partial t}, \tag{2.1}$$

$$\frac{1}{\mu_0}\nabla \times \boldsymbol{B} = \boldsymbol{J} + \epsilon_0 \frac{\partial \boldsymbol{E}}{\partial t} = \frac{\partial \boldsymbol{D}}{\partial t}. \tag{2.2}$$

The wave equation is expressed in Fourier representation (in frequency and wavenumber domain) as

$$\boldsymbol{k} \times [\boldsymbol{k} \times \boldsymbol{E}(\omega, \boldsymbol{k})] + \frac{\omega^2}{c^2}\boldsymbol{\epsilon} \cdot \boldsymbol{E}(\omega, \boldsymbol{k}) = 0. \tag{2.3}$$

Here, $\boldsymbol{\epsilon}$ is the dielectric tensor defined by

$$\boldsymbol{D}(\omega, \boldsymbol{k}) = \boldsymbol{\epsilon}(\omega, \boldsymbol{k}) \cdot \boldsymbol{E}(\omega, \boldsymbol{k}) = \epsilon_0 \boldsymbol{E}(\omega, \boldsymbol{k}) + \frac{i\boldsymbol{J}(\omega, \boldsymbol{k})}{\omega}. \tag{2.4}$$

The plasma current density can be expressed as

$$\boldsymbol{J} = \sum_s n_s q_s \boldsymbol{v_s}, \tag{2.5}$$

where n_s and $\boldsymbol{v_s}$ are the number density and the fluid velocity of particles of species s with charge q_s. Each species of particles obeys the fluid momentum equation of first order

$$m_s \frac{\mathrm{d}\boldsymbol{v_s}}{\mathrm{d}t} = q_s \left(\boldsymbol{E} + \boldsymbol{v_s} \times \boldsymbol{B_0}\right). \tag{2.6}$$

Consider a uniform magnetic field along the z-direction, $\boldsymbol{B_0} = B_0 \hat{\boldsymbol{z}}$. Using Eqs. (2.3), (2.4), (2.5), (2.6) the dielectric tensor is expressed as

$$\boldsymbol{\epsilon} = \begin{pmatrix} S & -iD & 0 \\ iD & S & 0 \\ 0 & 0 & P \end{pmatrix}. \tag{2.7}$$

S, P, D are the famous Stix parameters which are defined as

$$S = \frac{1}{2}(R + L), \tag{2.8}$$

$$D = \frac{1}{2}(R - L), \tag{2.9}$$

$$R = 1 - \sum_s \frac{\omega_{\mathrm{p}s}^2}{\omega(\omega + \Omega_s)}, \tag{2.10}$$

$$L = 1 - \sum_s \frac{\omega_{\mathrm{p}s}^2}{\omega(\omega - \Omega_s)}, \tag{2.11}$$

$$P = 1 - \sum_s \frac{\omega_{\mathrm{p}s}^2}{\omega^2}, \tag{2.12}$$

where $\omega_{\mathrm{p}s} = \sqrt{n_s q_s^2/(m_s \epsilon_0)}$ and $\Omega_s = (q_s B)/m_s$ are the plasma and cyclotron angular frequencies of species s, respectively.

It is convenient to normalize the wavenumber vector $\boldsymbol{k}$ by the magnitude of the wavenumber of light in vacuum

$$\boldsymbol{n} = \frac{\boldsymbol{k}c}{\omega}. \tag{2.13}$$

Taking $\boldsymbol{n}$ to be embedded in the x-z plane, and expressing the angle between $\boldsymbol{B_0}$ and $\boldsymbol{n}$ as θ, Eq. (2.3) becomes

$$\begin{pmatrix} S - n^2\cos^2\theta & -iD & n^2\cos\theta\sin\theta \\ iD & S - n^2 & 0 \\ n^2\cos\theta\sin\theta & 0 & P - n^2\sin^2\theta \end{pmatrix} \begin{pmatrix} E_x \\ E_y \\ E_z \end{pmatrix} = 0. \tag{2.14}$$

The determinant of the 3×3 matrix in Eq. (2.14) should be zero for a nontrivial solution to exist. This condition gives the dispersion relation

$$An^4 - Bn^2 - C = 0, \tag{2.15}$$

where

$$A = S\sin^2\theta + P\cos^2\theta, \tag{2.16}$$

$$B = RL\sin^2\theta + PS(1 + \cos^2\theta), \tag{2.17}$$

$$C = PRL. \tag{2.18}$$

The solution of Eq. (2.15) is

$$n^2 = \frac{B \pm \sqrt{(RL - PS)^2\sin^4\theta + 4P^2D^2\cos^2\theta}}{2A}. \tag{2.19}$$

It is convenient to rewrite Eq. (2.15) as an equation for $n_\perp = n\sin\theta$, because in practice, $n_\parallel = n\cos\theta$ is usually a given parameter which is determined by the antenna structure,

$$an_\perp^4 + bn_\perp^2 + c = 0, \tag{2.20}$$

where

$$a = S, \tag{2.21}$$

$$b = (S + P)n_\parallel^2 - RL - PS, \tag{2.22}$$

$$c = Pn_\parallel^4 - 2PSn_\parallel + PRL. \tag{2.23}$$

Then, the solution of Eq. (2.20) is

$$n_\perp^2 = \frac{-b \pm \sqrt{b^2 - 4ac}}{2a}. \tag{2.24}$$

A wave encounters a cutoff layer or a resonance layer when n^2 becomes zero or infinity, respectively. According to Eqs. (2.15)–(2.19), cutoff occurs when

$$P = 0 \quad \text{or} \quad R = 0 \quad \text{or} \quad L = 0, \tag{2.25}$$

and resonance occurs when

$$\tan^2\theta = -\frac{P}{S}. \tag{2.26}$$

Wave classification is clearly expressed in the CMA diagram (named after the inventors, Clemmow, Mullaly, and Allis). Figure 2.1 is a CMA diagram for a plasma containing only a single species of ions (deuterium). The parameter

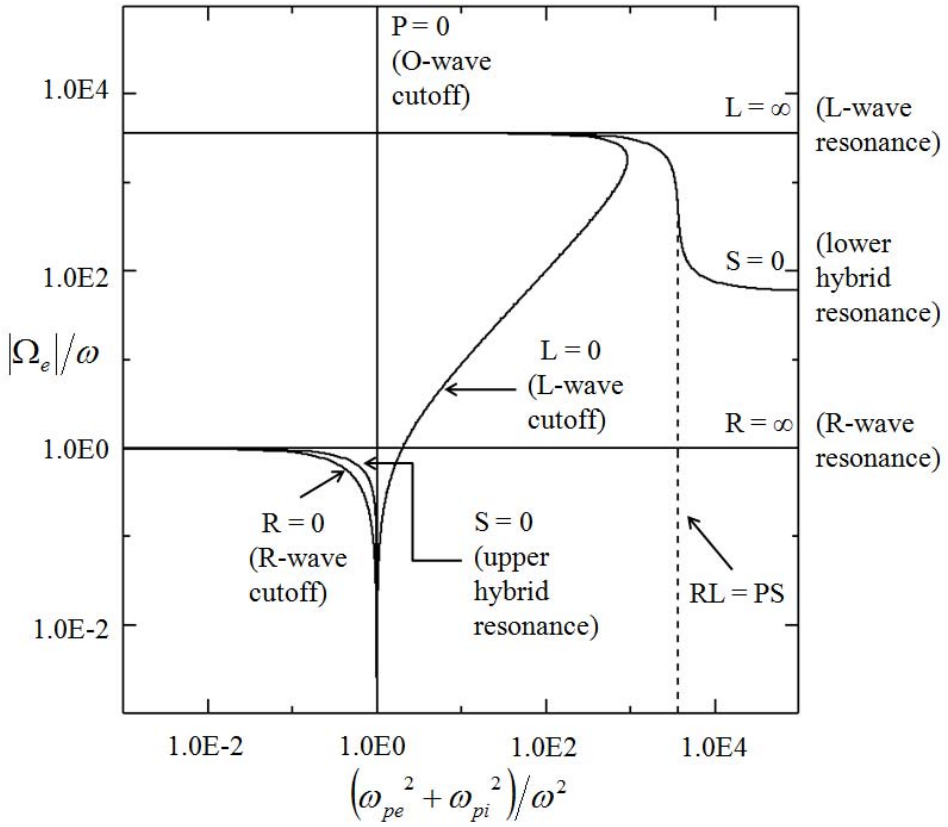

Figure 2.1: CMA diagram for a deuterium plasma.

space is divided by curves representing principal cutoffs and resonances by taking

$$\frac{\omega_{\mathrm{pe}}^2 + \omega_{\mathrm{pi}}^2}{\omega^2} \propto n_{\mathrm{e}} \tag{2.27}$$

for the x-axis and

$$\frac{|\Omega_{\mathrm{e}}|}{\omega} \propto B_0 \tag{2.28}$$

for the y-axis.

2.2 Waves in a Hot Plasma

The plasma is assumed to have a Maxwellian velocity distribution function in order to include finite temperature effects. Solving the Vlasov equation along the particle trajectory [43], the first order perturbation of the distribution

function is expressed as

$$f_1 = -\frac{q_\mathrm{e}}{m_\mathrm{e}} \exp i(\boldsymbol{k}\cdot\boldsymbol{r}-\omega t) \int_\infty^t \left[\left(1-\frac{\boldsymbol{k}\cdot\boldsymbol{v'}}{\omega}\right)\boldsymbol{E} + (\boldsymbol{v'}\cdot\boldsymbol{E})\frac{\boldsymbol{k}}{\omega}\right]\cdot\nabla'_v f_0$$
$$\times \exp\left[ik_x v_\perp\left(\frac{\sin[\theta+\Omega_\mathrm{e}(t'-t)]}{\omega}-\frac{\sin\theta}{\Omega_\mathrm{e}}\right)+i(k_x v_z-\omega)(t'-t)\right]\mathrm{d}t', \quad (2.29)$$

where f_0 is the unperturbed velocity distribution function

$$f_0 = \frac{1}{\pi^{2/3}V_{\mathrm{T}s}^3}\exp\left(-\frac{v^2}{V_{\mathrm{T}s}^2}\right), \quad (2.30)$$

$V_{\mathrm{T}s} = \sqrt{2\kappa T_s/m_s}$. The plasma current density J is given by

$$\boldsymbol{J} = \sum_s q_s \int \boldsymbol{v} f_{s1}\mathrm{d}\boldsymbol{v} \quad (2.31)$$

Therefore, substituting Eq. (2.31) into Eq. (2.4), Eq. (2.3) becomes

$$\begin{pmatrix} K_{xx}-n^2\cos^2\theta & -iK_{xy} & K_{xz}+n^2\cos\theta\sin\theta \\ iK_{xy} & K_{yy}-n^2 & iK_{yz} \\ K_{xz}+n^2\cos\theta\sin\theta & -iK_{yz} & K_{zz}-n^2\sin^2\theta \end{pmatrix}\begin{pmatrix} E_x \\ E_y \\ E_z \end{pmatrix} = 0. \quad (2.32)$$

where

$$K_{xx} = 1+\sum_s\frac{\omega_{\mathrm{p}s}^2}{\omega}\sum_{n=-\infty}^{\infty}\frac{n^2 I_n(\lambda)e^{-\lambda}}{\lambda}\frac{1}{k_\parallel V_{\mathrm{T}s}}Z_0(y_n), \quad (2.33)$$

$$K_{xy} = \sum_s\frac{\omega_{\mathrm{p}s}^2}{\omega}\sum_{n=-\infty}^{\infty} n(I_n-I'_n)e^(-\lambda)\frac{1}{k_\parallel V_{\mathrm{T}s}}Z_0(y_n), \quad (2.34)$$

$$K_{yy} = 1+\sum_s\frac{\omega_{\mathrm{p}s}^2}{\omega}\sum_{n=-\infty}^{\infty}\left(\frac{n^2}{\lambda}I_n+2\lambda I_n-2\lambda I'_n\right)\frac{e^{-\lambda}}{k_\parallel V_{\mathrm{T}s}}Z_0(y_n), \quad (2.35)$$

$$K_{xz} = -\sum_s\frac{\omega_{\mathrm{p}s}^2}{\omega}\sum_{n=-\infty}^{\infty}e^{-\lambda}\frac{k_\perp}{\Omega_s}\frac{nI_n}{\lambda}\frac{1}{2k_\parallel}\frac{\mathrm{d}Z_0(y_n)}{\mathrm{d}y_n}, \quad (2.36)$$

$$K_{yz} = -\sum_s\frac{\omega_{\mathrm{p}s}^2}{\omega}\sum_{n=-\infty}^{\infty}e^{-\lambda}\frac{k_\parallel}{\Omega_s}(I_n-I'_n)\frac{1}{2k_\parallel}\frac{\mathrm{d}Z_0(y_n)}{\mathrm{d}y_n}, \quad (2.37)$$

$$K_{zz} = 1-\sum_s\frac{\omega_{\mathrm{p}s}^2}{\omega}\sum_{n=-\infty}^{\infty}e^{-\lambda}\frac{2(\omega-n\Omega_s)}{k_\parallel V_{\mathrm{T}s}^2}I_n\frac{1}{2k_\parallel}\frac{\mathrm{d}Z_0(y_n)}{\mathrm{d}y_n}, \quad (2.38)$$

where $y_n \equiv (\omega-n\Omega_s)/(k_\parallel V_{\mathrm{T}s})$, $\lambda = (k_\perp^2\kappa T)/(m\Omega_s^2)$, I_n is the nth-order modified Bessel function, and Z_0 is the plasma dispersion function defined as

$$Z_0(y) = \frac{1}{\sqrt{\pi}}\int_{-\infty}^{\infty}\mathrm{d}z\frac{\exp(-z^2)}{z-y}, \quad \mathrm{Im}\, y > 0. \quad (2.39)$$

2.3 Wave Damping

2.3.1 Landau Damping

Consider a single-particle equation of motion under an electrostatic wave described by

$$\boldsymbol{E} = \hat{\boldsymbol{z}} E \cos(kz - \omega t), \tag{2.40}$$

$$m\frac{\mathrm{d}v}{\mathrm{d}t} = qE\cos(kz - \omega t). \tag{2.41}$$

The zeroth-order solution of Eq. (2.41) is

$$z = v_0 t + z_0. \tag{2.42}$$

Substituting this into Eq. (2.41) gives the equation for first-order velocity v_1,

$$m\frac{\mathrm{d}v_1}{\mathrm{d}t} = qE\cos(kz_0 + kv_0 t - \omega t). \tag{2.43}$$

Assuming $v_1 = 0$ when $t = 0$, the solution of Eq. (2.43) is obtained as

$$v_1 = \frac{qE}{m}\frac{\sin(kz_0 + kv_0 t - \omega t) - \sin(kz_0)}{kv_0 - \omega}. \tag{2.44}$$

The rate of change of particle energy in first order is

$$\begin{aligned}\frac{\mathrm{d}}{\mathrm{d}t}\frac{mv^2}{2} = \frac{q^2E^2}{m}\Bigg(&\left[\frac{\sin(kz_0 + \alpha t) - \sin(kz_0)}{\alpha}\right]\cos(kz_0 + \alpha t) \\ -kv_0&\left[\frac{-\cos(kz_0 + \alpha t) + \cos(kz_0)}{\alpha^2} - \frac{t\sin(kz_0)}{\alpha}\right]\sin(kz_0 + \alpha t)\Bigg),\end{aligned} \tag{2.45}$$

where $\alpha \equiv kv_0 - \omega$. The oscillatory terms can be eliminated by averaging over the initial position,

$$\begin{aligned}\left\langle \frac{\mathrm{d}}{\mathrm{d}t}\frac{mv^2}{2} \right\rangle &= \frac{q^2E^2}{2m}\left[-\frac{\omega\sin(\alpha t)}{\alpha^2} + t\cos(\alpha t) + \frac{\omega t\cos(\alpha t)}{\alpha}\right] \\ &= \frac{q^2E^2}{2m}\frac{\omega}{k}\frac{\mathrm{d}}{\mathrm{d}v}\left[\frac{\sin(kv - \omega)t}{kv - \omega}\right].\end{aligned} \tag{2.46}$$

The average rate of change of the particle energy is obtained by averaging Eq. (2.46) over velocity,

$$\begin{aligned}\frac{\mathrm{d}W}{\mathrm{d}t} &= \int \mathrm{d}v f(v) \left\langle \frac{\mathrm{d}}{\mathrm{d}t}\frac{mv^2}{2} \right\rangle \\ &= -\frac{q^2E^2}{2m}\frac{\omega}{k}\int_{-\infty}^{\infty}\mathrm{d}v\frac{\mathrm{d}f(v)}{\mathrm{d}v}\frac{\sin(kv-\omega)t}{kv-\omega} \\ &= -\frac{q^2E^2}{2m}\frac{\pi\omega}{k^2}\int_{-\infty}^{\infty}\mathrm{d}v\frac{\mathrm{d}f(v)}{\mathrm{d}v}\delta\left(v-\frac{\omega}{k}\right) \quad (t\to\infty) \\ &= -\frac{q^2E^2}{2m}\frac{\pi\omega}{k^2}\frac{\mathrm{d}f(v)}{\mathrm{d}v}\bigg|_{v=\omega/k}. \end{aligned} \tag{2.47}$$

This equation implies that the wave is damped if the gradient of the velocity distribution function is negative at the resonant velocity $v = \omega/k$. This process is called Landau damping. The change in particle velocity due to Landau damping can be expressed as velocity diffusion which is discussed in next chapter.

2.3.2 Magnetic Pumping

In the low frequency regime, the magnetic moment μ_m of the particle is conserved. The kinetic energy of the particle is expressed as

$$W = \frac{1}{2}mv_\parallel^2 + \mu_\mathrm{m}B. \tag{2.48}$$

Therefore, the conservation of kinetic energy leads to

$$m\frac{\mathrm{d}v_\parallel}{\mathrm{d}t} = -\nabla_\parallel(\mu_\mathrm{m}B) = -\mu_\mathrm{m}\nabla_\parallel B. \tag{2.49}$$

Comparing Eqs. (2.41) and (2.49), the correspondences of μ_m and $-\nabla_\parallel B$ in Eq. (2.49) to q and E in Eq. (2.41) can be identified. Therefore, the rate of change of the particle energy is given by

$$\frac{\mathrm{d}W}{\mathrm{d}t} = -\frac{\mu_\mathrm{m}^2 B_{1z}^2}{2m}\pi\omega\frac{\mathrm{d}f(v)}{\mathrm{d}v}\bigg|_{v=\omega/k}. \tag{2.50}$$

This process is called magnetic pumping.

2.3.3 Collisional Damping

The absorption mechanisms presented so far are collision-less processes. Collisional effects are modeled by introducing an effective collision frequency,

$\nu_{\rm eff}$ [44], which describes the loss of momentum. The dominant momentum loss process is electron-ion collision, hence $\nu_{\rm eff} \simeq \nu_{\rm ei}$. The momentum conservation equation Eq. (2.6) is modified as

$$m_{\rm e}\frac{{\rm d}v_{\rm e}}{{\rm d}t} = q_{\rm e}\left(\boldsymbol{E} + \boldsymbol{v_{\rm e}} \times \boldsymbol{B_0}\right) - \boldsymbol{I}\nu_{\rm eff} m_{\rm e} v_{\rm e}. \tag{2.51}$$

Therefore, the effect of electron-ion collision can be modeled by an effective electron mass,

$$m_{\rm eff} = m_{\rm e}(1 + i\nu_{\rm eff}/\omega). \tag{2.52}$$

Stix parameters are modified as

$$\tilde{P} \cong 1 - \frac{\omega_{\rm pe}^2}{\omega^2}\left(1 - \frac{i\nu_{\rm eff}}{\omega}\right), \tag{2.53}$$

$$\tilde{R} \cong 1 + \sum_i \left(\frac{\omega_{{\rm p}i}^2}{\Omega_i(\omega + \Omega_i)} + \frac{i\omega_{{\rm p}i}^2\nu_{\rm eff}}{\omega\Omega_i\Omega_{\rm e}}\right), \tag{2.54}$$

$$\tilde{L} \cong 1 - \sum_i \left(\frac{\omega_{{\rm p}i}^2}{\Omega_i(\omega - \Omega_i)} - \frac{i\omega_{{\rm p}i}^2\nu_{\rm eff}}{\omega\Omega_i\Omega_{\rm e}}\right), \tag{2.55}$$

$$\tilde{S} \cong 1 + \frac{\omega_{\rm pe}^2}{\Omega_{\rm e}} - \sum_i \left(\frac{\omega_{{\rm p}i}^2}{\omega^2 - \Omega_i^2} - \frac{i\omega_{{\rm p}i}^2}{\omega\Omega_i}\frac{\nu_{\rm eff}}{\Omega_{\rm e}}\right). \tag{2.56}$$

Here, we expanded terms in powers of $m_{\rm e}/m_{\rm i}$, and assumed $\nu_{\rm eff}/\omega \ll 1$ which is a good approximation for typical edge plasmas: $n_{\rm e} \leq 5 \times 10^{18}\,{\rm m}^{-3}$, $T_{\rm e} \cong 10$–$50\,{\rm eV}$. Substituting these parameters into Eq. (2.15), the real part of n_x is given as

$$n_{\rm r}^2 = (n_z^2 - R)(n_z^2 - L)/(S - n_z^2), \tag{2.57}$$

and the imaginary part of n_x is given as

$${\rm Im}(n_x) = \frac{n_{\rm r}}{2}\frac{\dfrac{\nu_{\rm eff}}{\omega}\dfrac{\omega^2}{\omega_{\rm pe}^2}\dfrac{n_z^2 D^2}{n_z^2 - S} + \dfrac{\nu_{\rm eff}}{\omega}\dfrac{\omega_{\rm pi}^2}{\Omega_{\rm i}\Omega_{\rm e}}\dfrac{(n_{\rm r}^2 + 2n_z^2 - 2S)}{n_{\rm r}^2}}{(n_z^2 - S) + \eta}, \tag{2.58}$$

where $\omega_{\rm pe}^2/\Omega_{\rm e}^2 \ll 1$ was assumed, and

$$\eta = \frac{\omega^2}{\omega_{\rm pe}}(RL - n_z^2 S - 2n_r^2 S). \tag{2.59}$$

Unless $n_z^2 \sim S$, η is a small term and can be ignored. In addition, the second term in the numerator of Eq. (2.58) is also typically small. The spatial damping rate can be expressed in the following approximate form,

$${\rm Im}(k_x) \cong \frac{\nu_{\rm eff} n_{\rm r}}{2c}\frac{\omega^2}{\omega_{\rm pe}^2}\frac{n_z^2 D^2}{(n_z^2 - S)^2}. \tag{2.60}$$

This process is called collisional damping.

Chapter 3

Lower Hybrid Wave

The LHW is the slow electrostatic wave in the frequency range intermediate between the electron cyclotron and ion cyclotron frequencies. The high current drive efficiency of LHW is confirmed in many conventional tokamaks.

The dispersion relation is plotted as $k^2(\omega)$ in Fig. 3.1. There is a resonance at $\omega = \Omega_{\rm LH} = |\Omega_{\rm Ce}\Omega_{\rm Ci}|^{1/2}$ for the wave propagating perpendicularly to the magnetic field ($\boldsymbol{k} \perp \boldsymbol{B}_0$). This resonance is called the lower hybrid resonance, and $\Omega_{\rm LH}$ is called the lower hybrid resonance frequency. On the other hand, the wave propagating parallel to the magnetic field ($\boldsymbol{k} \parallel \boldsymbol{B}_0$) has a resonance at $\omega = \Omega_{\rm Ce}$. The LHW can exist in the frequency range $\Omega_{\rm LH} < \omega \ll \Omega_{\rm Ce}$. The LHW, in general, has a finite propagation angle. In the experiment, the LHW is launched by the antenna placed on or near the outer wall of the vacuum vessel. The antenna imposes a definite periodicity in the toroidal direction and determines the wavenumber parallel to the magnetic field. Figure 3.2 shows the dependence of $n_\perp^2$ on ω for different $n_\parallel$. As described in the following section, the LHW can be treated as an electrostatic wave provided that

$$n^2 \sim n_\perp^2 \gg |P|. \tag{3.1}$$

3.1 Theory of LHW

3.1.1 Electrostatic Approximation

Since the LHW is an electrostatic wave, the electric field can be expressed as the gradient of a scalar potential,

$$\boldsymbol{E} = -\nabla\phi = -i(\hat{\boldsymbol{x}}k_x + \hat{\boldsymbol{z}}k_z)\phi. \tag{3.2}$$

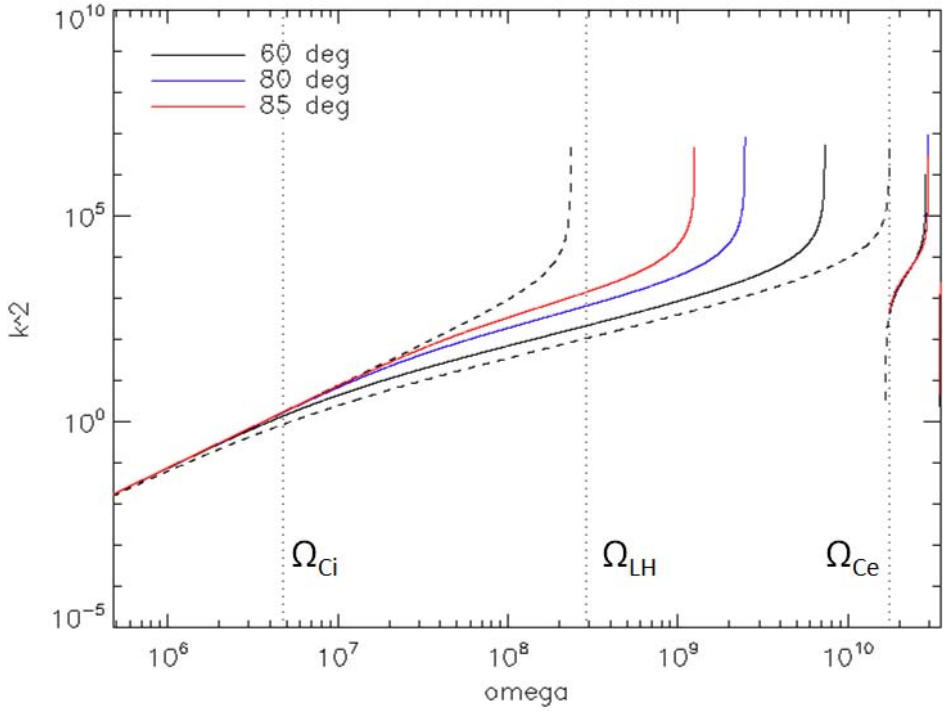

Figure 3.1: The dispersion relation plotted as $k^2(\omega)$ for $n_e = 1.8 \times 10^{17}\mathrm{m}^{-3}$ and B_T=0.1 T. The black, blue and red solid lines indicate the dispersion relation for propagation angles 60°, 80° and 85°, respectively. The black broken lines with resonances ($k^2 \to \infty$) at $\omega = \Omega_\mathrm{Ce}$ and $\omega = \Omega_\mathrm{LH}$ indicate the dispersion relations for parallel and perpendicular propagations, respectively.

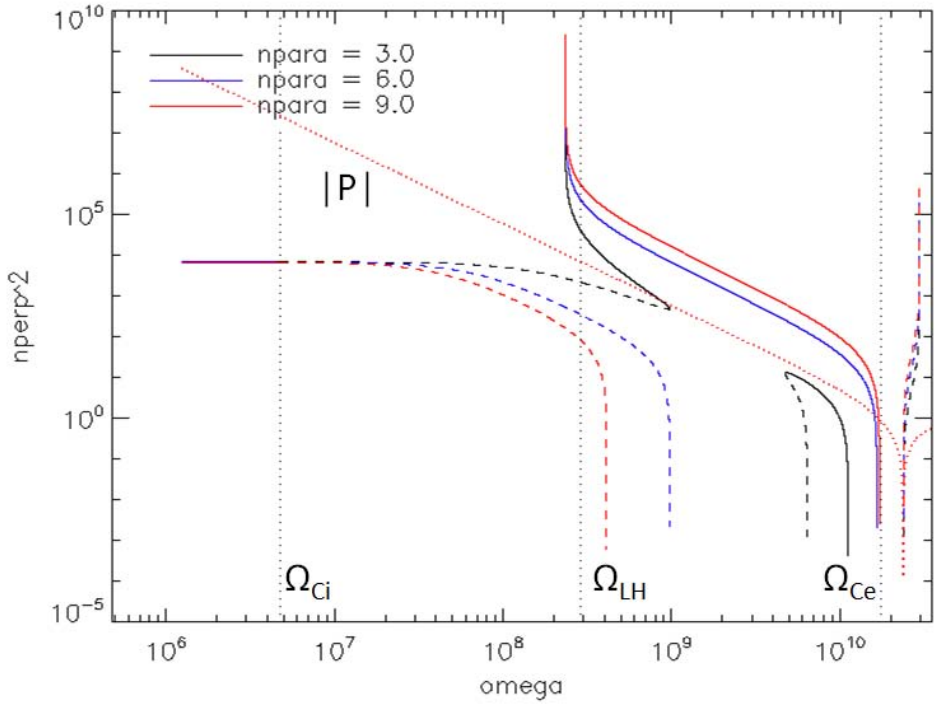

Figure 3.2: The dispersion relation plotted as $n_\perp^2(\omega)$ for $n_e = 1.8 \times 10^{17}\mathrm{m}^{-3}$ and B_T=0.1 T. The black, blue and red solid lines indicate the slow wave with $n_\parallel$ = 3, 6 and 9, respectively. The black, blue and red broken lines indicate those of the fast wave. The red dotted line shows the Stix parameter $|P|$.

Substituting into Eq.(2.3) and multiplying by $\boldsymbol{k}$ from the left yields

$$(\boldsymbol{k}\cdot\boldsymbol{\epsilon}\cdot\boldsymbol{k})\phi = 0. \tag{3.3}$$

For a cold plasma, Eq. (3.3) becomes

$$Sk_\perp^2 + Pk_\parallel^2 = 0. \tag{3.4}$$

The Fourier representation of Eq. (3.4) can be inverted to obtain

$$\frac{\partial^2\phi}{\partial x^2} = -\left(\frac{P}{S}\right)\frac{\partial^2\phi}{\partial z^2}. \tag{3.5}$$

This equation has a similar form to the wave equation. The solution of Eq. (3.5) describes propagation along the characteristics $z \pm (-P/S)^{1/2}x =$ const. Because of the symmetry in the plane perpendicular to the magnetic field in a uniform plasma, the characteristics define resonance cones. By splitting $\boldsymbol{E}$ into its longitudinal and transverse components, $\boldsymbol{E}_\parallel$ and $\boldsymbol{E}_\perp$, Eq. (2.3) can be written as

$$(n^2\boldsymbol{I} - \boldsymbol{\epsilon})\cdot\boldsymbol{E}_\perp = \boldsymbol{\epsilon}\cdot\boldsymbol{E}_\parallel. \tag{3.6}$$

Therefore, $\boldsymbol{E}_\perp$ will be small compared to $\boldsymbol{E}_\parallel$ when

$$n^2 \gg |P| > |\epsilon_{ij}| \tag{3.7}$$

for all i and j. This condition needs to be satisfied for the electrostatic approximation to be valid.

Eq. (3.4) has a singularity where $S = 0$. This singularity is removed by including the finite temperature effect. In this section, the finite Larmor radius (FLR) effects are assumed to be small, $\lambda \ll 1$ in Eqs. (2.33)–(2.38). The first-order FLR terms are added to Eq. (3.4) to give [45–47],

$$\alpha n_\perp^4 + \beta n_\perp^2 + \gamma = 0, \tag{3.8}$$

where

$$\alpha = \lim_{k_\perp\to 0}\frac{\omega^2}{c^2}\frac{\partial}{\partial k_\perp^2}K_{xx} = \frac{3}{2}\frac{\omega_{\rm pi}^2}{\omega^2}\frac{V_{\rm Ti}^2}{c^2}, \tag{3.9}$$

$$\beta = K_{xx\ \rm cold} = S, \tag{3.10}$$

$$\gamma = -n_\parallel^2\sum_s\frac{\omega_{{\rm p}s}^2}{k_\parallel^2 V_{{\rm T}s}^2}\frac{{\rm d}Z_0(y_0)}{{\rm d}y_0}, \tag{3.11}$$

and the singularity has disappeared. The $n_\perp^4$ term describes the thermal wave branch of the dispersion relation (ion plasma wave). Imaginary contributions, which describe Landau damping of the LHW by electrons and ions, arise from Z_0' in γ.

3.1.2 Physical Picture of the LHW

The physical picture of the LHW is described. Orbits of electrons and ions under the influence of an oscillating electric field perpendicular to the magnetic field $\boldsymbol{E} = \hat{\boldsymbol{x}} E_x \cos(\omega t)$ is considered. The equation of motion is written as

$$\frac{\mathrm{d}v_{xs}}{\mathrm{d}t} - \Omega_{\mathrm{Cs}} v_{ys} = \Omega_{\mathrm{Cs}} \frac{E_x \cos(\omega t)}{B_0} \tag{3.12}$$

$$\frac{\mathrm{d}v_{ys}}{\mathrm{d}t} + \Omega_{\mathrm{Cs}} v_{xs} = 0. \tag{3.13}$$

Since the frequency of the LHW is far greater than the ion cyclotron frequency and far smaller than the electron cyclotron frequency, $\Omega_{\mathrm{Ci}} \ll \omega \ll \Omega_{\mathrm{Ce}}$, ions can be treated as unmagnetized whereas electrons are strongly magnetized. Therefore, the second term on the left hand side of Eq. (3.12) can be ignored for ions, and the ion velocity can be written as

$$v_{x\mathrm{i}} = \frac{\Omega_{\mathrm{Ci}}}{\omega} \frac{E_x \sin(\omega t)}{B_0} \tag{3.14}$$

$$v_{y\mathrm{i}} = \frac{\Omega_{\mathrm{Ci}}^2}{\omega^2} \frac{E_x \cos(\omega t)}{B_0}. \tag{3.15}$$

Since $\omega \gg \Omega_{\mathrm{Ci}}$, ions exhibit oscillation nearly aligned to the direction of the electric field.

On the other hand, electrons are strongly magnetized. In order to separate the gyro-motion and the drift motion, we introduce a new velocity variable $\boldsymbol{u}$,

$$u_{x\mathrm{e}} = v_{x\mathrm{e}} + \frac{\omega}{\Omega_{\mathrm{Ce}}} \frac{E_x \sin(\omega t)}{B_0} \tag{3.16}$$

$$u_{y\mathrm{e}} = v_{y\mathrm{e}} - \frac{E_x \cos(\omega t)}{B_0}. \tag{3.17}$$

The equation of motion can then be written as

$$\frac{\mathrm{d}u_{x\mathrm{e}}}{\mathrm{d}t} - \Omega_{\mathrm{Ce}} u_{y\mathrm{e}} = \frac{\omega^2}{\Omega_{\mathrm{Ce}}} \frac{E_x \cos(\omega t)}{B_0} \sim 0 \tag{3.18}$$

$$\frac{\mathrm{d}u_{y\mathrm{e}}}{\mathrm{d}t} + \Omega_{\mathrm{Ce}} u_{x\mathrm{e}} = 0. \tag{3.19}$$

The right hand side of Eq. (3.18) is smaller than that of Eq. (3.12) by $(\omega/\Omega_{\mathrm{Ce}})^2$. Therefore, electrons exhibit $E \times B$ drift oscillation perpendicular to the electric field.

3.2 Expected Propagation of LHW in TST-2

3.2.1 Propagation and Mode Conversion

The variation in density and magnetic field across the plasma midplane is shown by the red trajectory on the CMA diagram in Fig. 3.3. The FW can exist only between the cutoff layer depicted by the green curve and the mode conversion layer which is along the edge of the blue region in Fig. 3.3 (a). In order to examine the characteristics of the cutoff and mode conversion layers, a higher density case shown by the light blue curve in Fig. 3.3 (a) is also considered. The solutions of the cold plasma dispersion relation with parameters indicated by asterisks in Fig. 3.3(a) are shown in (d) for the low density case, and in (e) for the high density case. It can be seen that the wave with $n_\parallel$ smaller than the critical value cannot propagate, and there are two solutions (LHW and FW) for a certain value of $n_\parallel$.

In TST-2, the LHW is excited by three types of antennas which are the combline antenna, the grill antenna and the ECC antenna. As the wave propagates inward, the toroidal mode number n_ϕ of the wave is conserved because of toroidal symmetry. As a result, the toroidal component of the wavenumber k_T changes as $k_\mathrm{T} = n_\phi/R$. In the present analysis, the toroidal direction is considered to coincide with the parallel direction (equivalent to ignoring the poloidal field) for simplicity. Figure 3.4 shows the solution of Eq. (2.20) across the midplane for $n_\phi = 18$ which corresponds to the LHW excited by the combline antenna. For the low density case (a), the FW is evanescent for any R. On the other hand, mode conversion between the FW and the LHW occurs for the high density case (b).

3.2.2 Quasilinear Diffusion

The effect of high power RF waves was modeled as diffusion in velocity space [48]. This treatment can be justified if a band of waves produces an overlap of island phase space trajectories of trapped particles ("phase mixing"). Considering the one dimensional motion of a single particle whose zeroth order motion is expressed as

$$z = vt + z_0 \tag{3.20}$$

in a traveling wave $\mathbf{E}(z,t) = \hat{\mathbf{z}} E\cos(kz - \omega t)$, the first order motion can be described by

$$m\frac{d}{dt}\Delta v = qE\cos(kz_0 + kvt - \omega t). \tag{3.21}$$

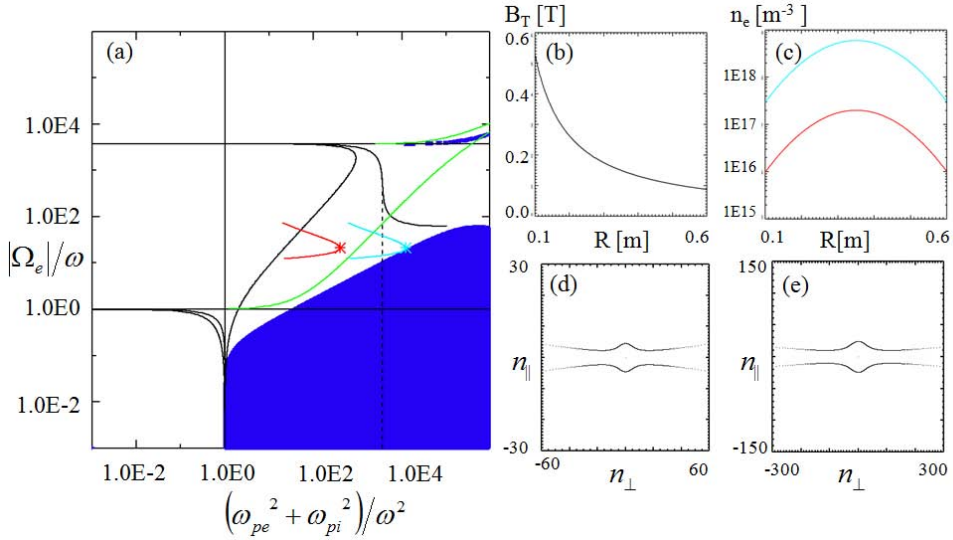

Figure 3.3: (a) CMA diagram. Red and light blue curves indicate variations of density and magnetic field in TST-2 for a low density case and a high density case, respectively. The green curve shows the cutoff layer for the FW with $n_\parallel = 7.16$ (corresponds to $n_\phi = 18$ at $R = 0.6$m). The edge of the blue region indicates the LHW to the FW mode conversion layer with $n_\parallel = 12.3$ (corresponds to $n_\phi = 18$ at $R = 0.35$m). There is no propagating wave inside the blue region. The profiles of B_T and n_e on the midplane of the torus are plotted in (b) and (c). The solutions of the cold plasma dispersion relation for plasma parameters at the points indicated by asterisks in (a) are shown in (d) for the low density case and in (e) for the high density case.

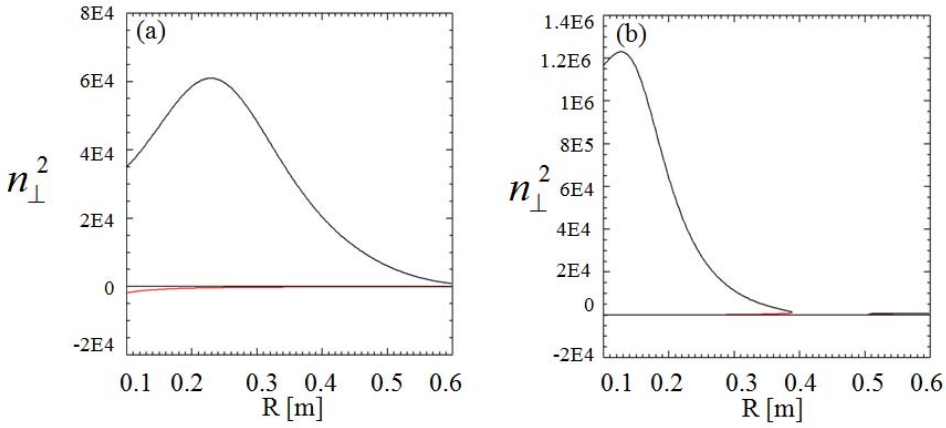

Figure 3.4: Solutions for $n_\perp^2$ across the midplane for parameters given in Fig. 3.3 and $n_\parallel = n_\phi/R$ ($n_\phi = 18$) for (a) the low density case and (b) the high density case.

Integrating the first order motion one can calculate

$$\Delta v = \frac{qE}{m(\omega - kv)} \sin[kz_0 - (\omega - kv)t] - \sin kz_0. \tag{3.22}$$

Averaging over the initial position z_0 yields

$$\overline{(\Delta v)^2} = 2\left[\frac{qE}{m(\omega - kv)}\right]^2 \sin^2\left[\frac{(\omega - kv)t}{2}\right] \simeq \pi\left(\frac{qE}{m}\right)^2 t\delta(\omega - kv). \tag{3.23}$$

The last approximation in Eq. (3.23) is valid in the limit of large t, $\omega t \gg 1$. Finally, the velocity space diffusion coefficient can be written as:

$$D_v = \frac{\overline{(\Delta v)^2}}{2t} = \frac{\pi}{2}\left(\frac{qE}{m}\right)^2 \delta(\omega - kv). \tag{3.24}$$

If there is a monochromatic wave, Eq. (3.23) just describes the averaged width of the trapped particle trajectory in phase space. The concept of velocity space diffusion can be applied if the wave spectrum is dense enough to destroy the phase coherence between modes by phase mixing and the phase space trajectory becomes stochastic. Therefore, the quasilinear diffusion coefficient can be derived by integrating Eq. (3.24) over k,

$$D_v(v) = \frac{\pi}{2}\left(\frac{q}{m}\right)^2 \int_{-\infty}^{\infty} dk |E_k|^2 \delta(\omega - kv) \tag{3.25}$$

If the LHW with an asymmetric parallel wavenumber spectrum is used, an asymmetric velocity distribution function with respect to $v_{\parallel}$ will develop as a result of quasilinear diffusion. The $v_{\parallel}$ moment of the asymmetric velocity distribution gives the plasma current driven by the LHW.

3.2.3 Full Wave Simulation Using TORLH/CQL3D

TORLH is a full wave simulation code for propagation and absorption of LHW [49]. A spectral representation of the electric field is employed in this simulation as

$$\mathbf{E}(x) = \sum_m \mathbf{E}_m(\psi) \exp(im\theta + in\phi). \tag{3.26}$$

TORLH solves the wave equation Eq. (2.3) by casting it into Galerkin's weak variational form. The finite element discretization is used in the radial direction, which allows fast calculation of the solution. The advantage of full wave method is that the effect of diffraction and interference can be retained unlike the ray tracing simulation. In TORLH ion finite Larmor radius (FLR) effect is neglected. Therefore the ion plasma wave branch cannot be treated. This simplification is justified since the ion plasma wave is strongly evanescent under experimental conditions where $\omega/\omega_{\mathrm{LH}} > 2$. The waves are absorbed by electron Landau damping (ELD) and transit time magnetic pumping (TTMP). Although the FLR terms play no role, thermal effects are retained through the plasma dispersion function contributions to ELD and TTMP in the plasma model.

The interaction of the waves with the electrons far out on the tail of the distribution function creates a non-Maxwellian plateau. This deformation of the distribution function is calculated by the CQL3D bounce-averaged Fokker-Planck code [50]. The distribution function is assumed to be constant on the flux surface and can be expressed as $f = f(t, \psi, u_0, \theta_0)$ where $u_0 = p_0/m$ is the particle momentum per mass, and $\theta_0 = u_{\perp,0}/u_{\parallel,0}$ is the pitch angle, both evaluated on the low field side midplane. The Fokker-Planck equation is written as:

$$\frac{\partial}{\partial t}(\lambda f_{e0}) = \nabla_{u0} \cdot \Gamma_{u0} + \langle R \rangle + \langle S \rangle, \tag{3.27}$$

where $\lambda = |v_{\parallel,0}|\tau_B$, τ_B is the bounce time, $\langle R \rangle$ is the bounce and gyro averaged radial diffusion term and $\langle S \rangle$ is the averaged particle source term. The

velocity space divergence of flux vector Γ_{u0} can be written as

$$\nabla_{u0} \cdot \Gamma_{u0} = \frac{1}{u_0^2}\frac{\partial}{\partial u_0}G_0 + \frac{1}{u_0^2 \sin\theta_0}\frac{\partial}{\partial \theta_0}H_0 \tag{3.28}$$

$$G_0 = u_0^2 \Gamma_{u_0} = \left(A_0 + B_0\frac{\partial}{\partial u_0} + C_0\frac{\partial}{\partial \theta_0}\right) f_0, \tag{3.29}$$

$$H_0 = u_0 \sin\theta_0 \Gamma_{\theta_0} = \left(D_0 + E_0\frac{\partial}{\partial u_0} + F_0\frac{\partial}{\partial \theta_0}\right) f_0. \tag{3.30}$$

The quasi-linear diffusion coefficient is expressed as δB_0 [51]

$$\lambda\langle \delta B_0 \rangle = v_{\|0} \oint \sum_{m_1,m_2} \frac{\mathrm{d}l}{|v_\||} \frac{u_\|^4 E_\|^{(m_1)} E_\|^{*(m_2)}}{\gamma^2(\omega/k_{\|1})(\omega/k_{\|2})} e^{i\theta(m_1-m_2)} \delta(\omega - v_\| k_{\|1}) J_0(k_\perp u_\perp/\Omega_{\mathrm{ce}}) \tag{3.31}$$

As can be seen in this equation, the effect of interference for quasilinear diffusion coefficient is treated properly in TORLH.

3.2.4 Simulations for TST-2 Plasma Parameters

TORLH/CQL3D simulations are performed under the conditions of TST-2 experiments. Due to the low temperature (less than 100 eV) absorption of LHW is very weak in Maxwellian plasmas. However, damping becomes stronger when quasilinear deformation of the distribution function is taken into account as can be seen in Fig. 3.5. Simulations for higher density and temperature are also performed. Stronger toroidal field is needed to satisfy the accessibility condition to the plasma core. In these cases, the central electron temperature is assumed to be T_{e0}=200 eV. As is shown in Fig. 3.6(a), relatively strong absorption at the edge is calculated for $n_\| = 8.9$ which corresponds to the wave excited for 90 degree phasing of the grill antenna. On the other hand, for $n_\| = 5.9$ which corresponds to the wave excited for 60 degree phasing of the grill antenna, the LHW can propagate to the plasma core and drive current at smaller minor radii (Fig. 3.6).

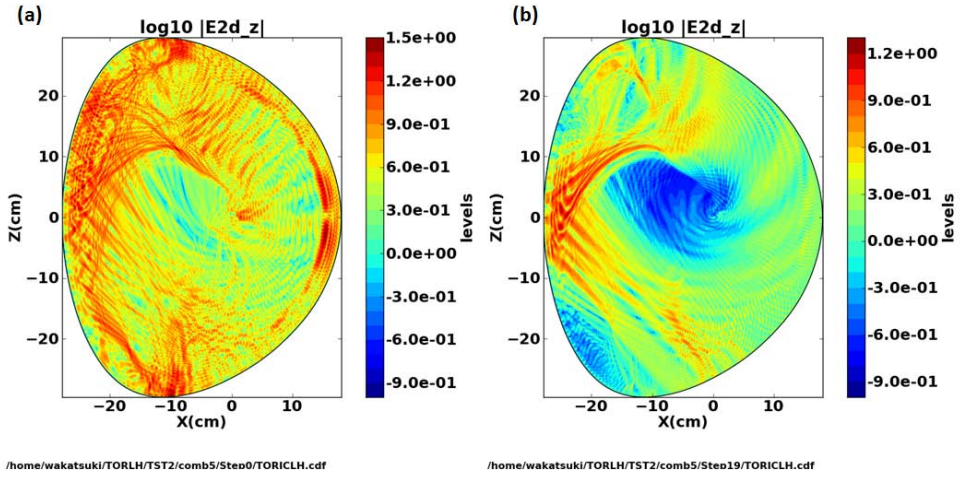

Figure 3.5: Comparison of the parallel electric field distribution for (a) Maxwellian plasma and (b) non-Maxwellian plasma, obtained after 20 iterations between TORLH and CQL3D. $T_{e0} = 50$ eV, $n_{e0} = 5 \times 10^{17}$ m^{-3}, $B_T = 0.1$ T, $n_{\|} = 7.1$. The colors indicate the logarithm of the absolute value of the parallel electric field.

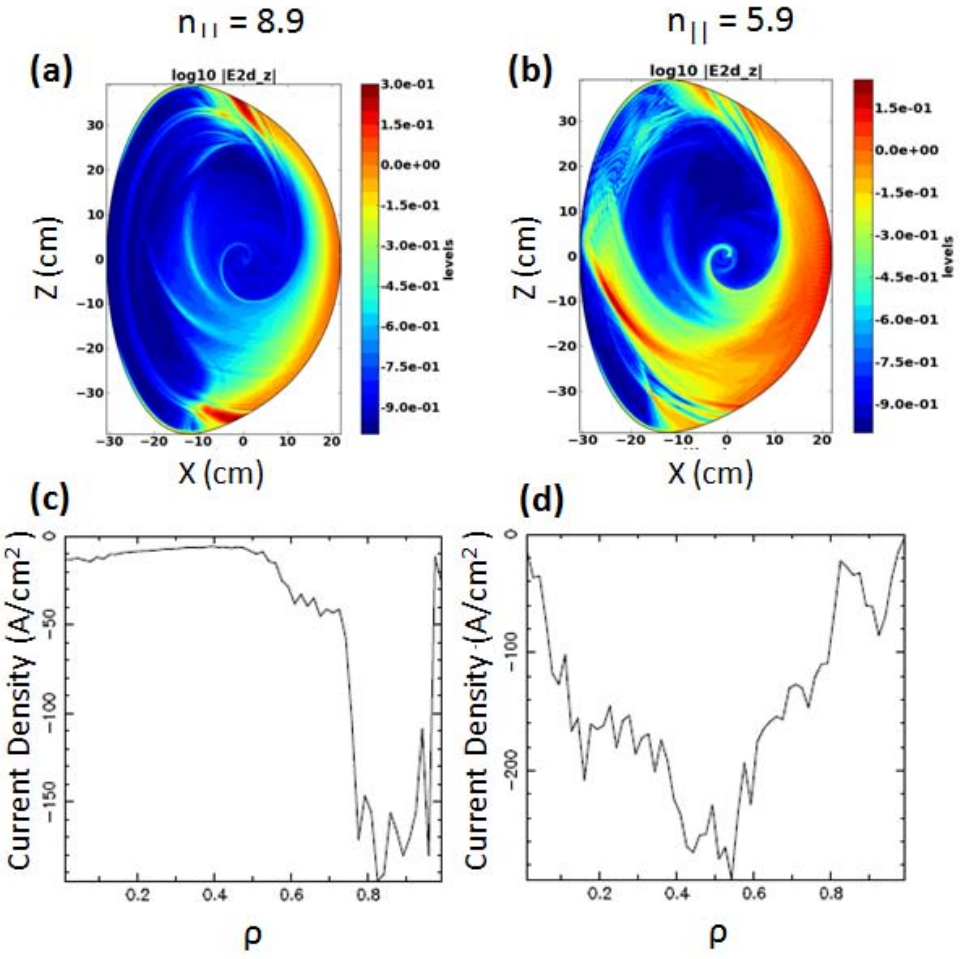

Figure 3.6: Comparison of the parallel electric field distribution and driven current density for (a), (c) $n_{\parallel} = 8.9$ and (b), (d) $n_{\parallel} = 5.9$. $T_{e0} = 200$ eV, $n_{e0} = 1 \times 10^{18}$ m^{-3}, $B_T = 0.3$ T. The colors indicate the logarithm of the absolute value of the parallel electric field.

Chapter 4

TST-2

4.1 The TST-2 Device

TST-2 (Tokyo Spherical Tokamak 2) is a spherical tokamak at the University of Tokyo with major radius $R_0 \simeq 0.38\,\mathrm{m}$, minor radius $a \simeq 0.25\,\mathrm{m}$, and aspect ratio $A \simeq 1.5$ [52]. Typical plasma parameters are: toroidal magnetic field $B_\mathrm{T} \simeq 0.15\,\mathrm{T}$, plasma current $I_\mathrm{p} \simeq 100\,\mathrm{kA}$, electron density $n_\mathrm{e} \simeq 1 \times 10^{19}\ \mathrm{m}^{-3}$, and electron temperature $T_\mathrm{e} \simeq 300\,\mathrm{eV}$ for operation using the central solenoid. Figure 4.1 shows a cross sectional view of TST-2. The OH coil (central solenoid) induces a toroidal electric field by induction, which drives the plasma current and heats the plasma resistively. The TF coils generate the toroidal magnetic field, the PF coils generate the magnetic field primarily in the vertical direction to achieve tokamak equilibrium and control the cross-sectional shape of the plasma, and the H coils are used to control the vertical position of the plasma.

4.2 Diagnostics

Many diagnostic instruments are installed on TST-2. The plasma current is measured by the rogowski coil surrounding the vacuum vessel.A microwave interferometer is used to measure the line integrated electron density along three vertical (R = 290, 380, 600 mm) and three horizontal (Z = −220, 0, +200 mm) chords. Electromagnetic radiation from the plasma is measured over a broad range of photon energies. In particular, the X-ray measurements are used to investigate the high energy electrons produced by the LHW. The energy spectrum of X-rays generated by bremsstrahlung (photon number per

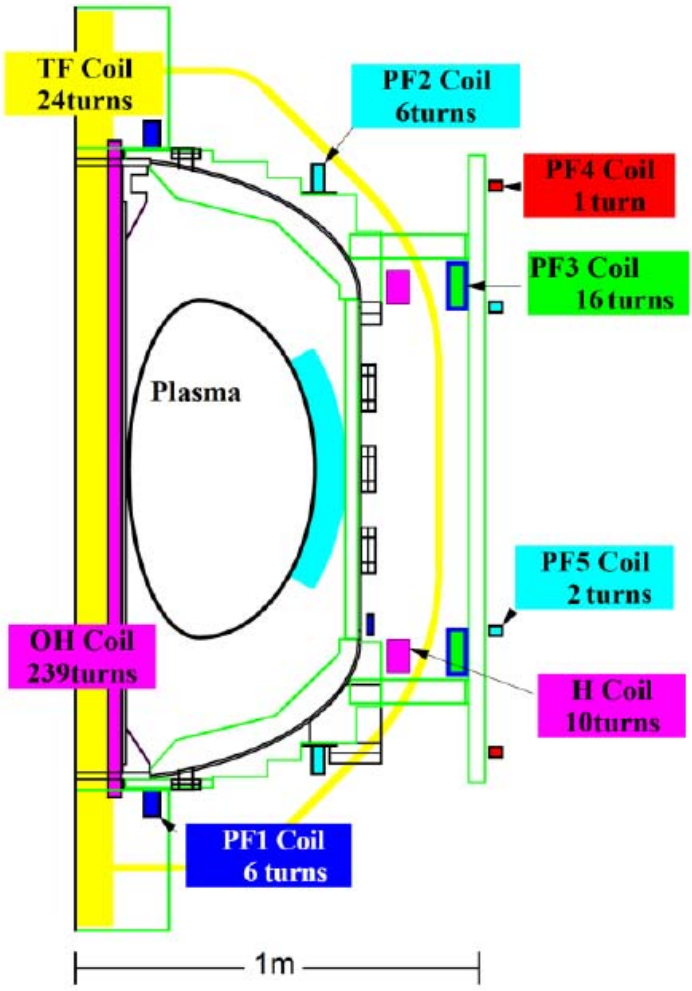

Figure 4.1: Cross-sectional drawing of TST-2.

unit volume per unit time) is given by [53, 54]

$$\frac{dP_{\rm B}}{dE} = 3 \times 10^{-3}\, n_{\rm e}^2 \frac{Z_{\rm eff}}{\sqrt{T_{\rm e}}} g_{\rm f}(T_{\rm e}, E) \exp\left(-\frac{E}{T_{\rm e}}\right) [{\rm m}^{-3}\,{\rm s}^{-1}], \qquad (4.1)$$

where $n_{\rm e}$ [$\rm m^{-3}$], E [keV], $T_{\rm e}$ [keV], $Z_{\rm eff}$ and $g_{\rm f}$ are the electron density, photon energy, electron temperature, effective ion charge number, and the Gaunt factor which is approximately unity.

4.2.1 Soft X-ray Detectors

Soft X-ray (SX:10 eV∼20 keV) radiation is measured by semiconductor detectors. A semiconductor detector has a junction of p-type and n-type semiconductors. When a photon with sufficient energy strikes the depletion layer between the p-n junction, electron-hole pairs are generated, and a current proportional to the number of electron-hole pairs is generated. We use two types of detectors, "AXUV" and "SBD". The "AXUV (absolute extreme ultraviolet) photodiode" [55] is a product manufactured by IRD Inc., and it is sensitive to photons in the energy range 7 eV to 6000 eV. The "SBD (surface barrier diode)" is a photodiode with a thin coating of aluminum, with additional thin-film filters made of beryllium or polypropylene. Figure 4.2 shows the detection efficiencies of these detectors. SBD without filter (aluminum coating only), with polypropylene filter, and with beryllium filter are mainly sensitive to photons in the energy range 10-70 eV, $> 200\,$eV, and $> 1\,$keV, respectively. However, it is difficult to detect SX photons with energies less than 100 eV because photons in this energy range are absorbed by the impurities on the surface of the detector. Therefore, the SBD without an additional filter might be sensitive to photons with energies greater than 100 eV.

The AXUV and SBD detectors are connected directly to the vacuum flange on the mid-plane of TST-2 because SX is strongly attenuated in air. These detectors view the plasma core perpendicularly to the toroidal magnetic field as shown in Fig. 4.7.

4.2.2 Hard X-ray Detector

NaI scintillators were used to measure hard X-rays (HX) with energies in excess of 100 keV. A scintillator is a crystal which emits scintillation light when struck by an X-ray photon or an incoming particle. The amplitude of the emitted light is proportional to the energy of the absorbed X-ray. We used scintillators made of a Sodium Iodide (NaI) crystal doped by a small

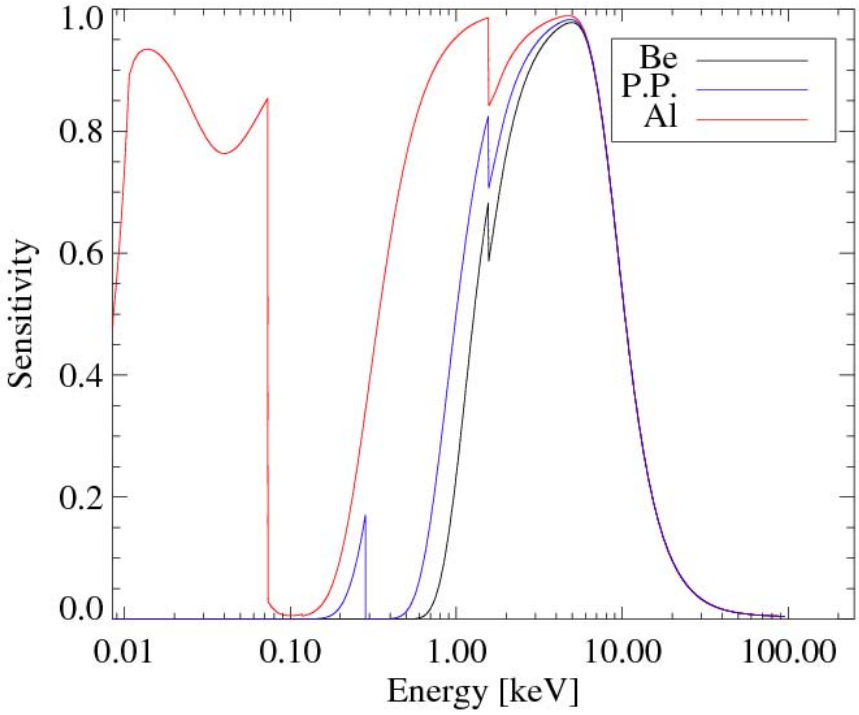

Figure 4.2: Detection efficiencies of SBD detectors with different filters. The X-ray attenuation coefficients are derived from the data in [56, 57]. The thickness of the Be filter is 15 μm, the polypropylene is 4 μm

amount of Thallium (Tl). The scintillation light is converted to an electric signal by the photomultiplier tube (PMT). The signal gain of the PMT can be controlled by changing the control voltage of the PMT. The relationship between the output signal and the X-ray energy was calibrated by measuring the well-known radiation sources. We used ^{137}Cs and ^{57}Co. The ^{137}Cs nucleus decays by β^- emission to the metastable ^{137m}Ba with the probability of 94.7 %. The metastable ^{137m}Ba decays into the stable ^{137}Ba by the gamma transition whose energy is 662 keV [58, 59]. The ^{57}Co nucleus decays by electron capture to the excited state of ^{57}Fe at 136 keV. This nucleus decays into the ground state emitting gamma rays with energies 122 keV (85.5 %) and 14 keV (9.15 %) in cascade, or emitting 136 keV gamma ray (10.7 %) [58, 60]. The energy resolution of the detector was not high enough to distinguish these two decay branches. Therefore, the weighted average value of 124 keV was assumed to be the energy of the photoelectric absorption of the gamma rays from ^{57}Co. The resultant gamma energy spectrum of ^{137}Cs and ^{57}Co are shown in Fig. 4.3 and Fig. 4.4. The large lower energy peak in the ^{137}Cs spectrum is a consequence of the backscatter peak from the lead block surrounding the radiation source and the detector. The voltage-energy relationship was estimated using the peak voltages corresponding to the 662 keV photoelectric peak of ^{137}Cs and the 124 keV peak of ^{57}Co as shown in Fig. 4.5.

As the HX is not strongly absorbed in air, the NaI scintillator is placed behind a vacuum window on the mid-plane of TST-2, and its position can be changed. The detector is surrounded by 30 mm thick lead blocks except for the front in order to suppress the backscattering effect. The front block has a 3 mm diameter, 80 mm long pinhole to collimate the sight line of the scintillator. The directivity of this pinhole was confirmed by changing the position of the radiating source as shown in Fig. 4.6. The geometric opening angle of this collimator is 2 degrees while the half width at half maximum is 2.7 degrees. The viewing solid angle is 4×10^{-3} str, but the viewing angle was restricted by the port edge and the actual viewing solid angle was less than this value.

The viewing chords of HX detectors are shown in Fig. 4.7 and Fig. 4.8. Hard X-rays emitted by energetic electrons as bremsstrahlung are strongly directed in the forward direction when the energy of the incident electron exceed several hundreds keV, as shown in Fig. 4.9 [61, 62]. Therefore, the detectors with viewing chords labeled “HX view (Co)” in Fig. 4.7 and Fig. 4.8 measure HX photons emitted from current-carrying fast electrons accelerated by the LHW. The viewing chords labeled “HX view (Counter)” in Fig. 4.7 and Fig. 4.8 measure HX photons emitted in the opposite direction. A difference in HX emission measured along “Co” and “Counter” viewing chords indicates

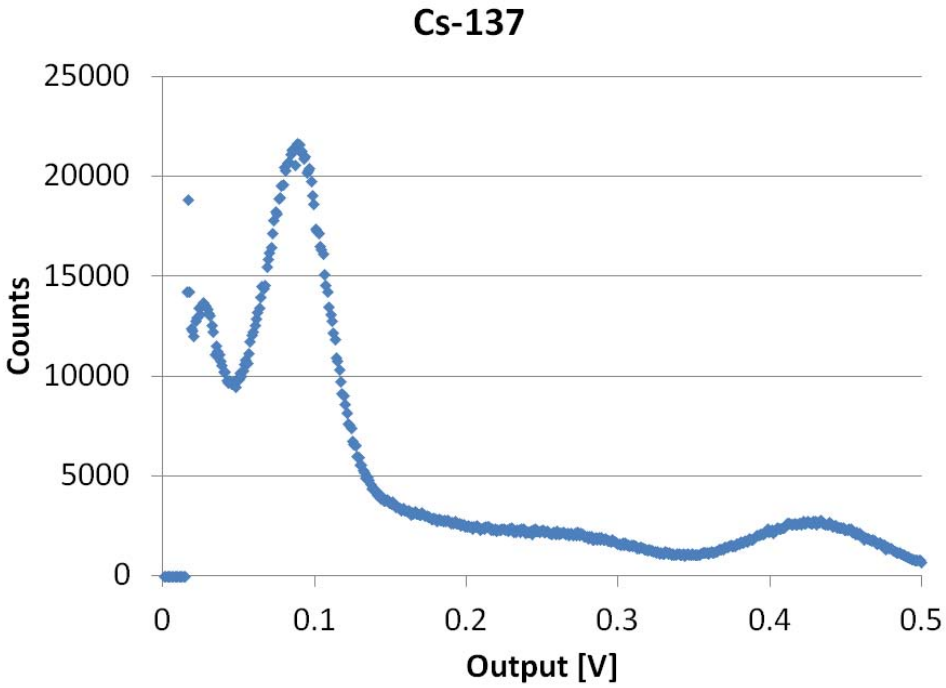

Figure 4.3: The gamma spectrum of ^{137}Cs.

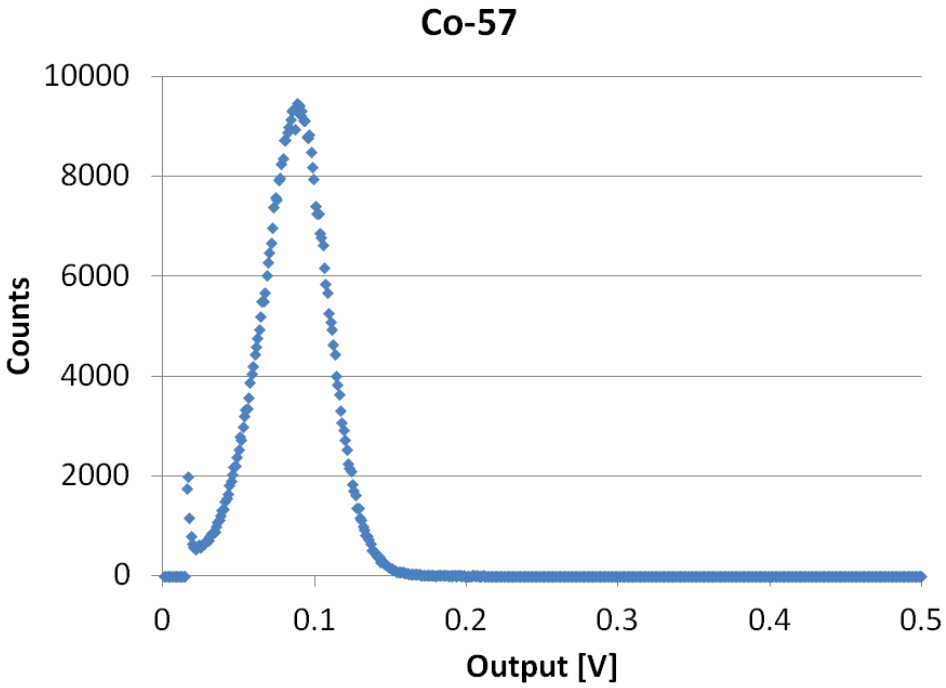

Figure 4.4: The gamma spectrum of ^{57}Co.

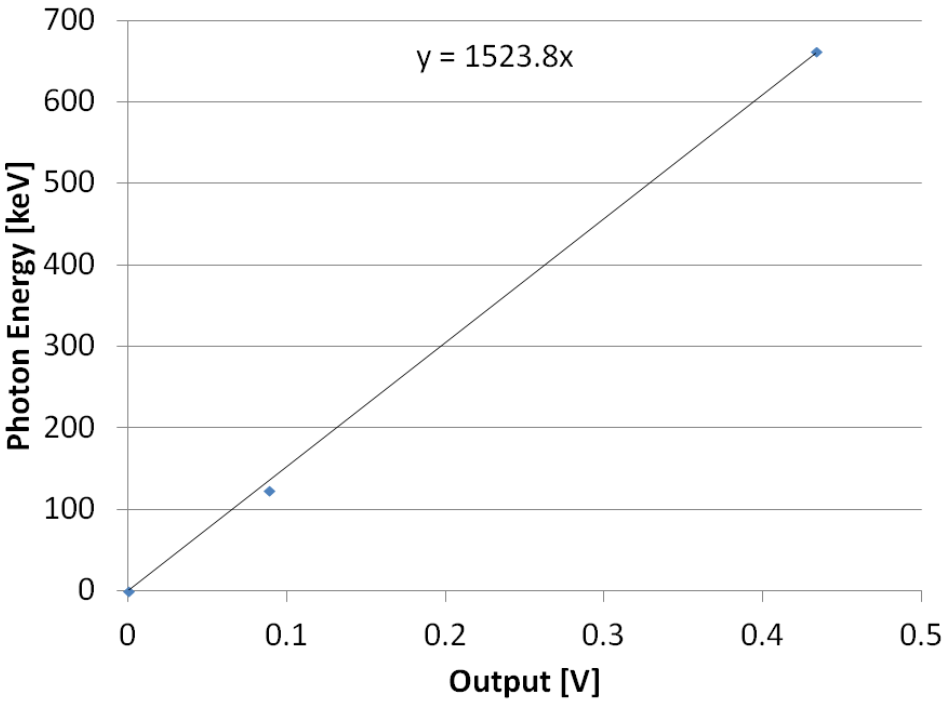

Figure 4.5: The voltage-energy relationship of the HX detector system.

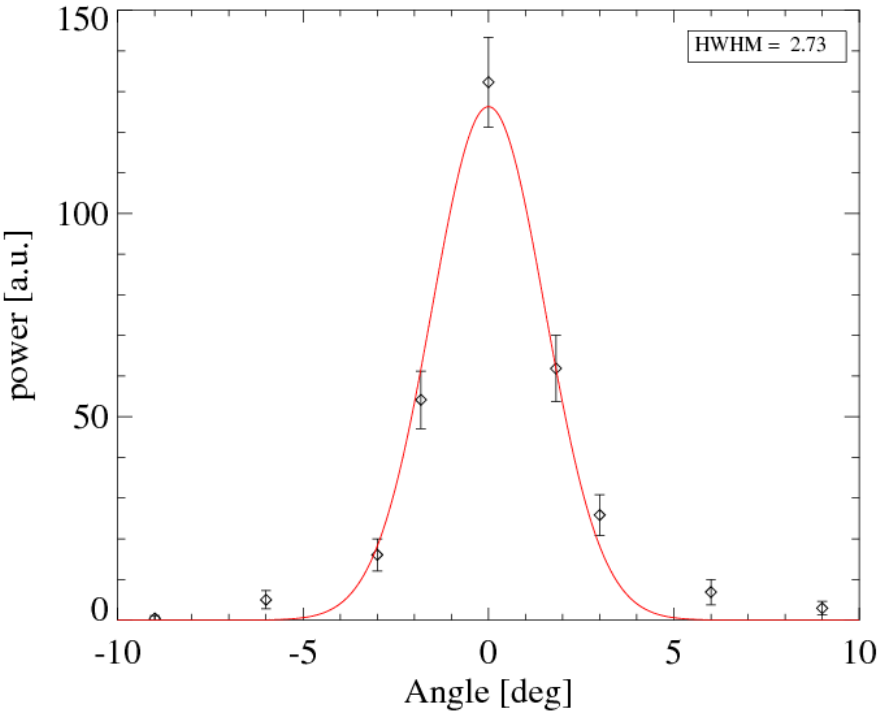

Figure 4.6: The directivity of the HX detector.

	Gain	Input Power	Output Power
Pre Amplifier	40 dB	50 mW	1 kW
Excitation and Intermediate Amplifiers	13 dB	1 kW	20 kW
Final Power Amplifier	8 dB	20 kW	120 kW

Table 4.1: Typical parameters of 200 MHz power amplifiers.

asymmetry in the fast electron velocity distribution.

We intend to measure only HX photons emitted by fast electrons colliding with ions. HX photons can also be emitted when electrons collide with a solid material. This emission is called thick-target bremsstrahlung. The strongest thick-target bremsstrahlung is emitted when fast electrons strike the limiter surrounding the antenna, which is placed approximately 100 mm inward (towards the plasma) from the vacuum vessel wall. This radiation was measured when the viewing chord is shifted 5 degrees as shown by the green region in Fig. 4.7. Figure 4.10 shows the effect of thick-target bremsstrahlung. The radiation from the chord angle 5 degrees from the center of the viewing chord is reduced to 0.5 % by the collimator as shown in Fig. 4.6. Therefore, for the "HX view (Co)" viewing chord in Fig. 4.7 the possible contamination from thick-target bremsstrahlung is one to two orders of magnitude smaller than the plasma bremsstrahlung.

4.3 LHW System

4.3.1 High Power Amplifier System

A block diagram of the 200 MHz high power amplifier system is shown in Fig. 4.11. The RF amplifier system consists of a signal generator, attenuators, phase shifters, a power divider, power combiners, circulators, and several stages of amplifiers. The maximum output power is 120 kW for each of the four units. Typical parameters of power amplifiers are summarized in Table 4.1.

4.3.2 Combline Antenna

The combline antenna (Fig. 4.12) consists of eleven vertically oriented current straps whose electrical length is $\lambda/4$. The 200 MHz RF power is fed to the antenna from the amplifier through the vacuum feed-through connected to the antenna strap on one outermost strap (input strap). Each antenna strap

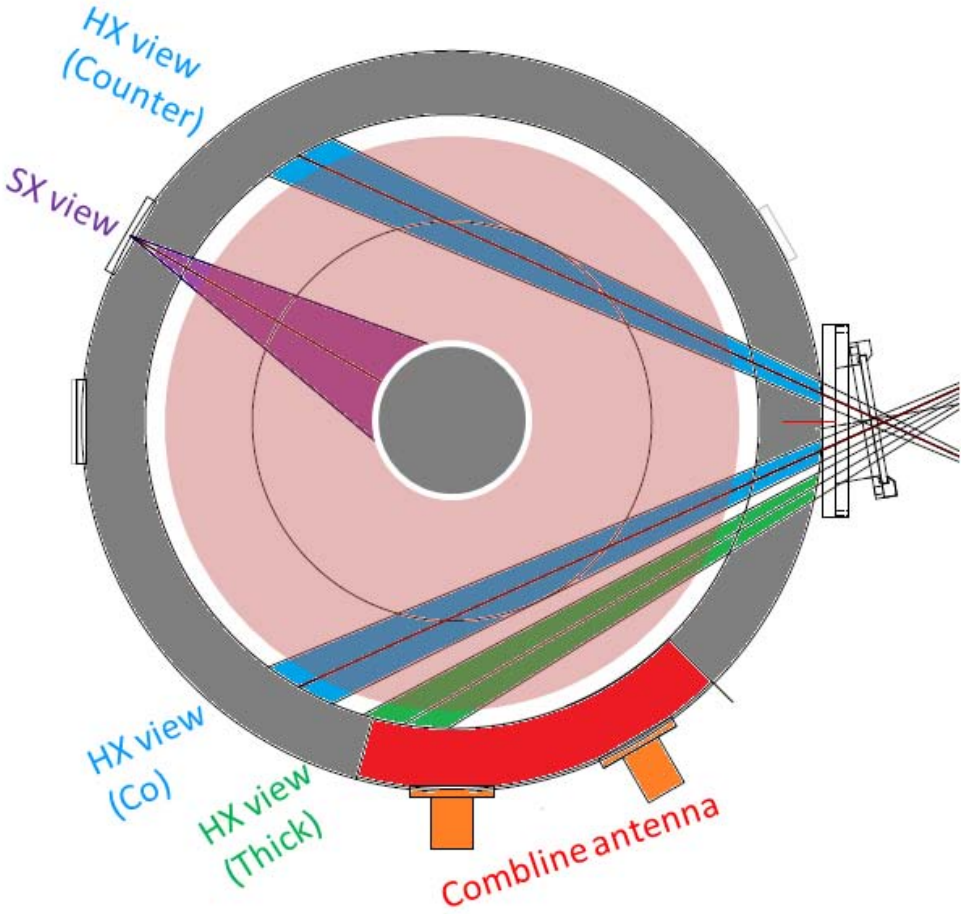

Figure 4.7: The viewing chords of X-ray detectors when the combline antenna was used. The purple region indicates the viewing region of the SX detector. The blue regions indicate the viewing regions of HX detectors in "Co" and "Counter" directions. The green region indicate the viewing region which includes the limiter which is the dominant source of thick-target bremsstrahlung.

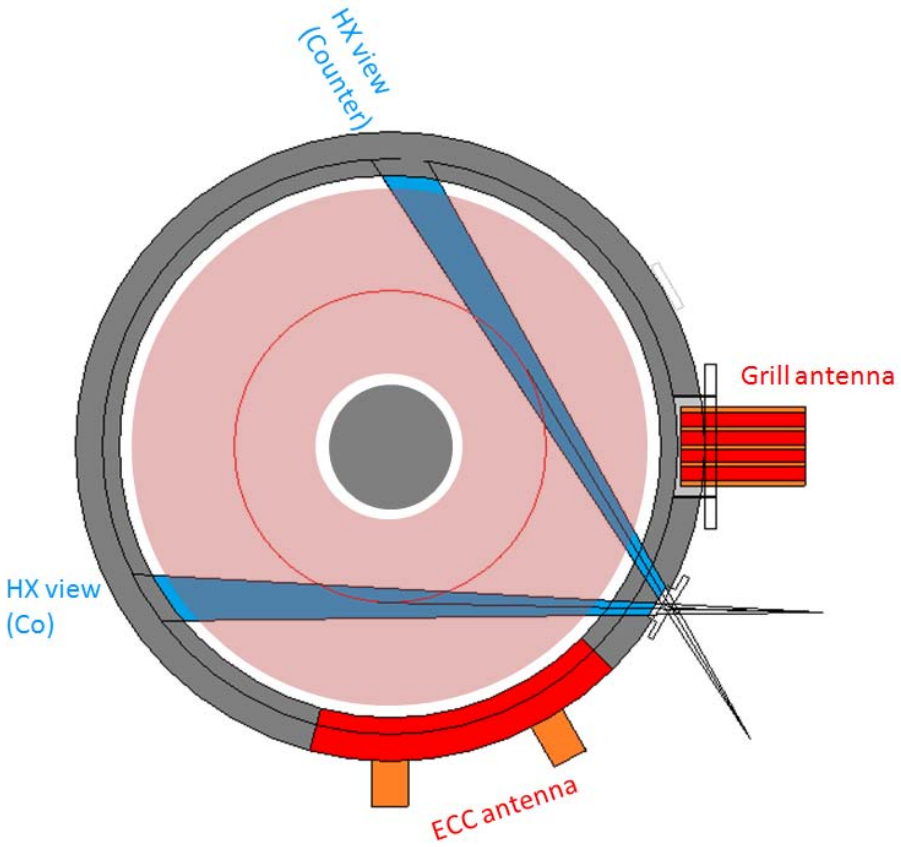

Figure 4.8: The viewing chords of the X-ray detectors when the grill antenna and the ECC antenna were used. The blue regions indicate the viewing regions of HX detectors in "Co" and "Counter" directions.

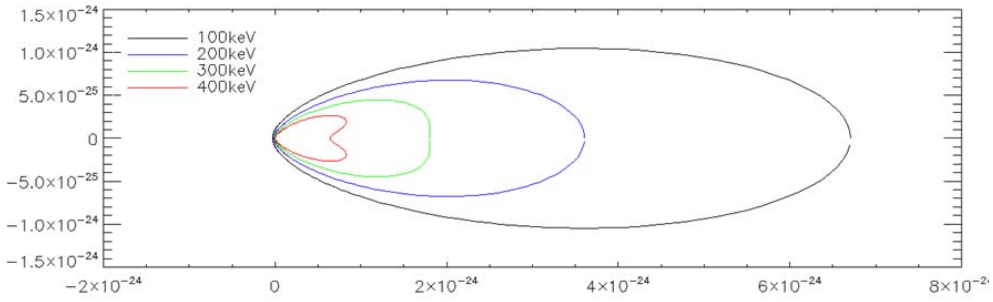

Figure 4.9: Polar plot of electron-ion bremsstrahlung intensity (in arbitrary units). The energy of the incident electron is 500 keV. The black, blue, green and red traces indicate the intensities of the emitted X-rays with energies 100, 200, 300 and 400 keV, respectively.

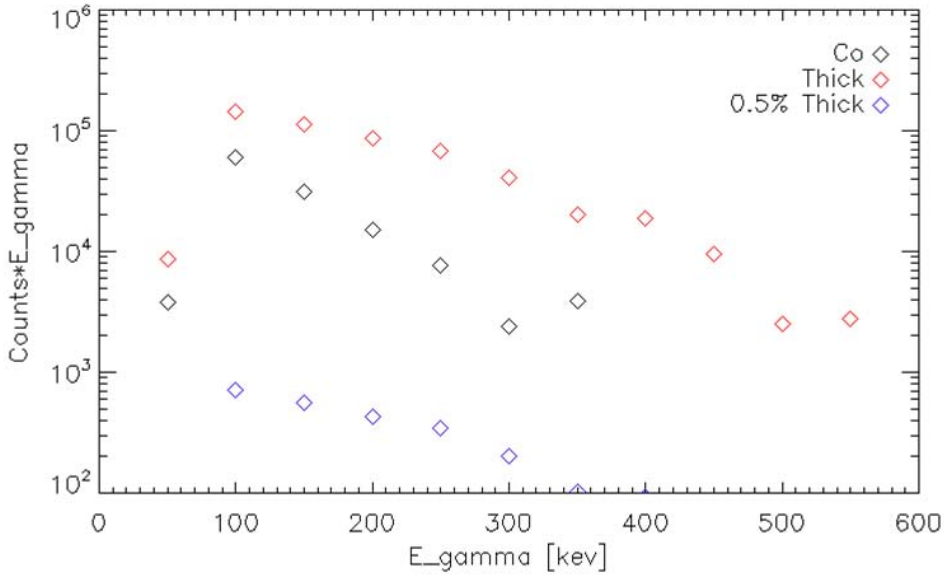

Figure 4.10: The effect of thick-target bremsstrahlung. The black and red symbols indicate HX energy spectra measured along the viewing chords labeled "HX view (Co)" and "HX view (Thick)" in Fig. 4.7. The collimator reduced the count rate from thick-target bremsstrahlung 0.5 % (blue symbols), which is much less than the electron-ion bremsstrahlung.

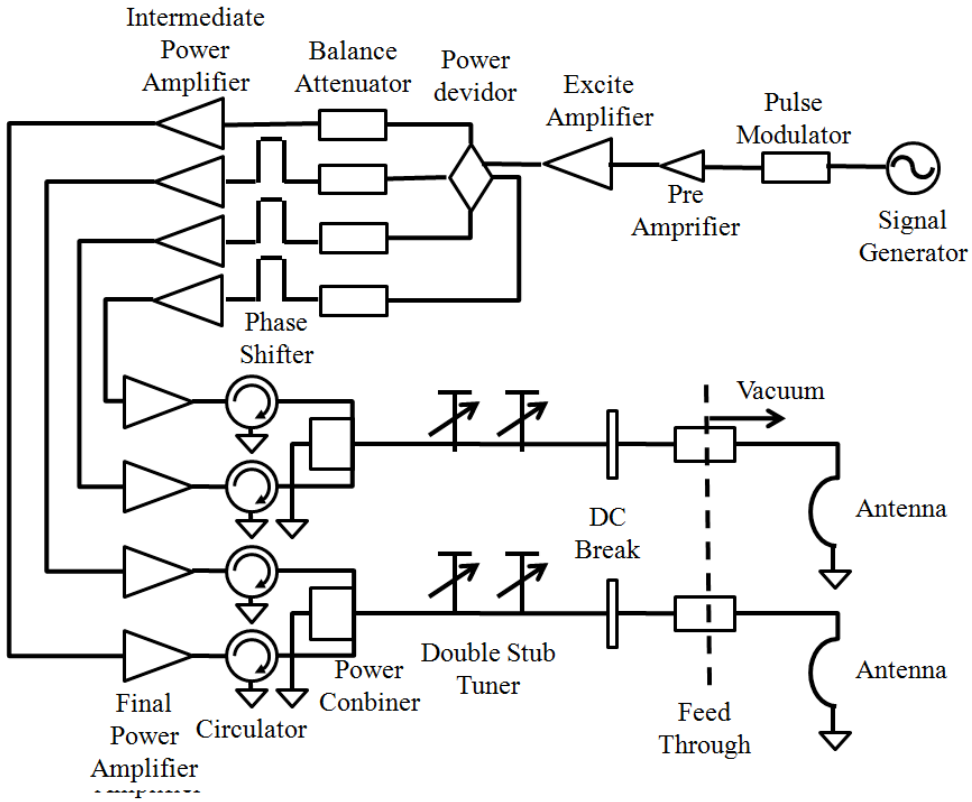

Figure 4.11: Block diagram of the 200 MHz high power amplifier system.

is mutually coupled to the adjacent straps inductively. The inductance and capacitance of the antenna strap are adjusted so that the phase difference between RF currents in adjacent straps is 90 degrees. As a result, $n_{\parallel}$ of the launched wave is 7.2. The RF power transmitted to the other outermost strap (output strap) exits the vacuum vessel through the feed-through and is absorbed by the dummy load. The input port-through power is up to 150 kW, but the power injected into the plasma is less than 70 kW, and the remainder is dissipated in the dummy load. The current straps are vertically aligned and the toroidally oriented Faraday shield elements surrounding each current strap suppress the electric field parallel to the toroidal magnetic field. Therefore, this antenna excites the RF magnetic field only in the toroidal direction. This polarization is usually called the "fast wave" polarization.

The wave excitation by the combline antenna was simulated using a versatile finite element method (FEM) solver package COMSOL [63]. This simulation code solves the wave equation for a specified dielectric tensor. The cold plasma dielectric tensor expressed as in Eq. (2.7) was given. The assumed plasma density and toroidal magnetic field were $n_e = 5 \times 10^{16}\mathrm{m}^{-3}$ and $B_{\mathrm{T}} = 0.06\mathrm{T}$. The radial RF electric field distribution of simulated wave excited by the combline antenna is shown in Fig. 4.13. This wave satisfies the dispersion relation of the slow wave (i.e. LHW). This is because the FW is cutoff at such a low density, and a propagating FW cannot exist under this condition.

4.3.3 Dielectric Loaded Grill Antenna

In many tokamak devices, the LHW is launched by a waveguide array antenna (a.k.a. grill antenna). The grill antenna can provide slow wave structure needed to shorten the wavelength, and can excite the RF electric field aligned in the toroidal direction. The LHW is an electrostatic wave (wavevector parallel to the electric field). Therefore, the grill antenna is suitable for exciting the LHW. However, a conventional grill antenna cannot be utilized in TST-2. The frequency used for the LHW experiment in TST-2 is 200 MHz, which is one order of magnitude lower compared to conventional tokamak experiments due to weaker toroidal field. Therefore, the wavelength is an order of magnitude longer, and the height of the waveguide must be at least 0.75 m (half of free-space wavelength). This is larger than the largest port of TST-2. In order to overcome this difficulty, a dielectric loaded waveguide array was proposed. The size of the waveguide can be reduced to about one-third by filling the waveguide with alumina ceramic (aluminum oxide) whose relative permittivity is 10. It is technically very difficult to metalize a large alumina block whose largest dimension exceeds 1 m. Therefore, the method

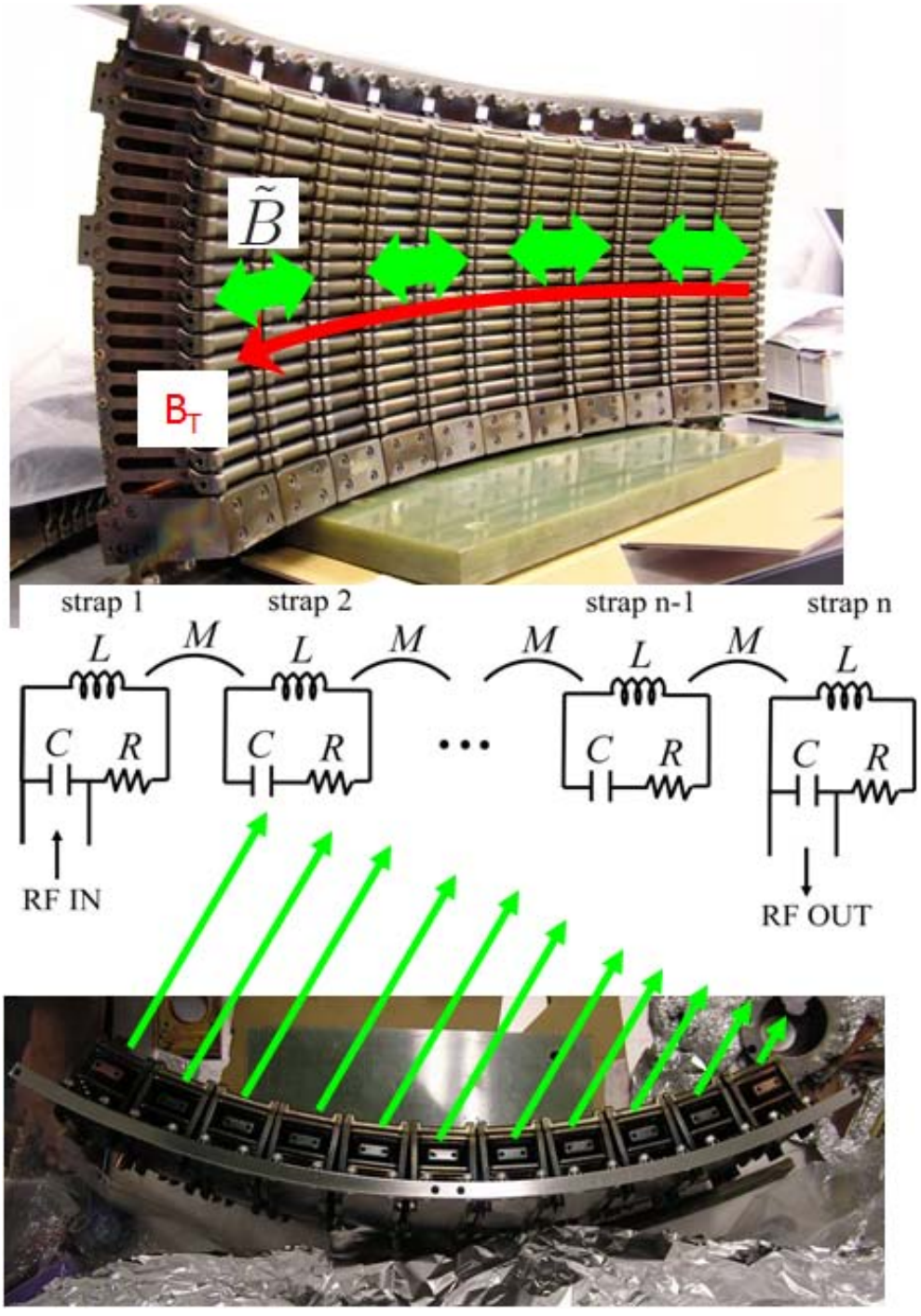

Figure 4.12: The (inductively-coupled) combline antenna. The top figure shows the front view of the combline antenna. The direction of the toroidal magnetic field is shown by the red arrow and the direction of the RF magnetic field excited by the antenna is shown by the green arrows. The middle figure shows an equivalent circuit model of the combline antenna. The bottom figure shows the top view of the combline antenna. the direction of the group velocity of the excited wave is indicated by green arrows.

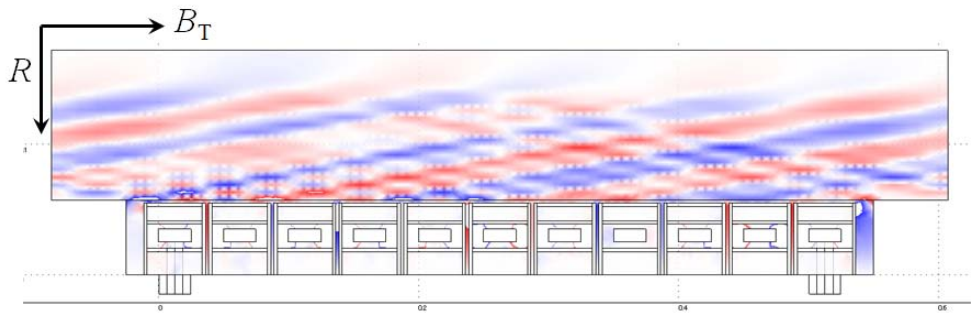

Figure 4.13: The radial component of the RF electric field excited by the combline antenna for $n_e = 5 \times 10^{16}\mathrm{m}^{-3}$ and $B_T = 0.06\mathrm{T}$. Periodic boundary conditions are imposed on the left and right boundaries. Artificially high collisionality is added near the top boundary to suppress unwanted reflection.

of electroless plating was utilized to cover the surface of the alumina block with an 80 μm thick nickel layer. Four such nickel covered alumina blocks were used as dielectric loaded waveguide elements of the array. The vacuum seal is accomplished with O-rings around each waveguide. Figure 4.14 is a photograph of the grill antenna. This antenna consists four waveguides. There is a movable private limiter placed around the waveguide array to control the density in front of the waveguide opening which strongly affects the coupling efficiency of the grill antenna to the plasma. The relative phase of the RF electric field in each waveguide can be changed arbitrarily since each waveguide is fed by a different amplifier with an independent phase shifter. The $n_\parallel$ spectrum of the excited wave can be changed by changing the phase difference between adjacent waveguides. The $n_\parallel$ spectra for three different antenna phasings (i.e., relative phases between adjacent waveguides) are shown in Fig. 4.15. The kinetic energy of electrons which have same velocity as the parallel phase velocity of LHW is plotted versus $n_\parallel$ in Fig. 4.16. The LHW with $n_\parallel = 3$ can interact with the electron whose kinetic energy is 31 keV if $v_\perp = 0$, for example.

Coax-waveguide transformers are needed because the RF power is transmitted from the amplifiers to the antenna by coaxial lines. Several types of transformers were investigated using COMSOL [63]. Since a simple design is preferred because it is difficult to machine alumina, a short-ended design is employed in which the inner conductor of the coaxial section is connected to the opposite wall of the waveguide. The optimization of this transition for 200 MHz was achieved with respect to the waveguide thickness (H) and the

Figure 4.14: Dielectric loaded waveguide array (grill) antenna

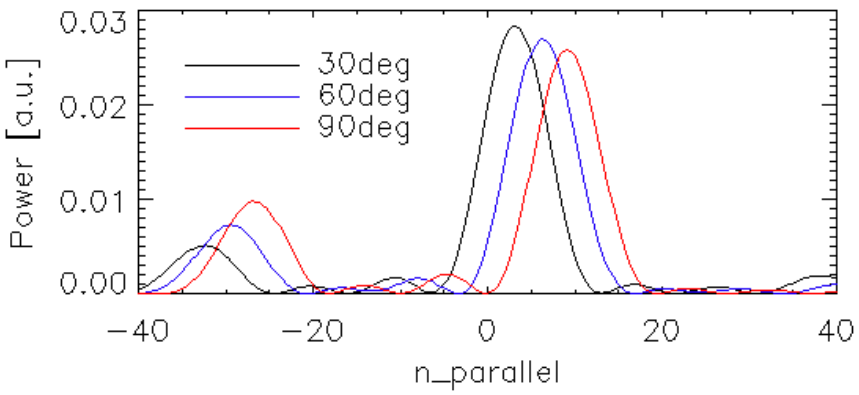

Figure 4.15: The $n_{\|}$ spectra of the LHW excited by the grill antenna for three different antenna phasings, 30° (black), 60° (blue) and 90° (red).

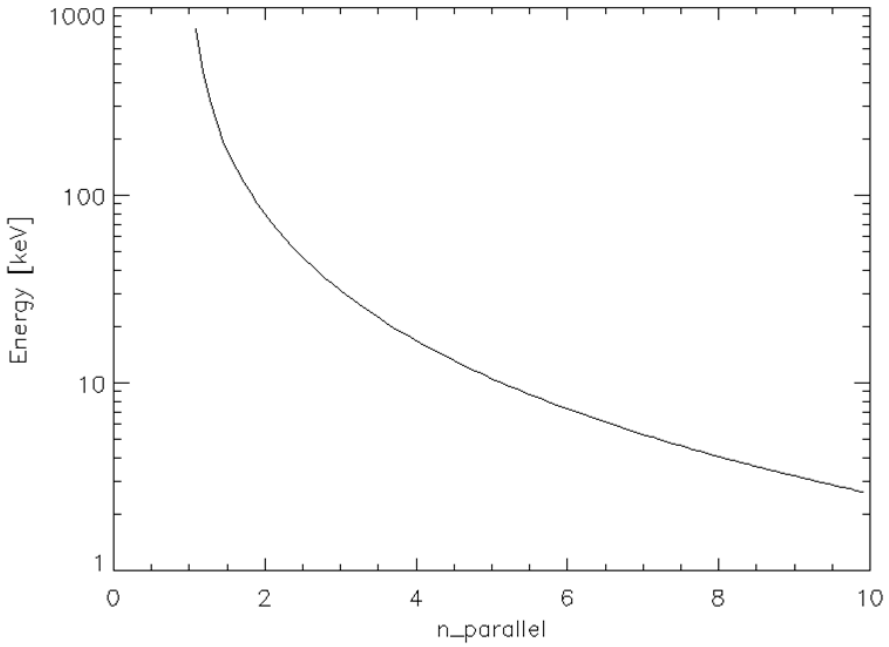

Figure 4.16: The kinetic energy of electrons which have same velocity as the parallel phase velocity of LHW is plotted versus $n_{\|}$.

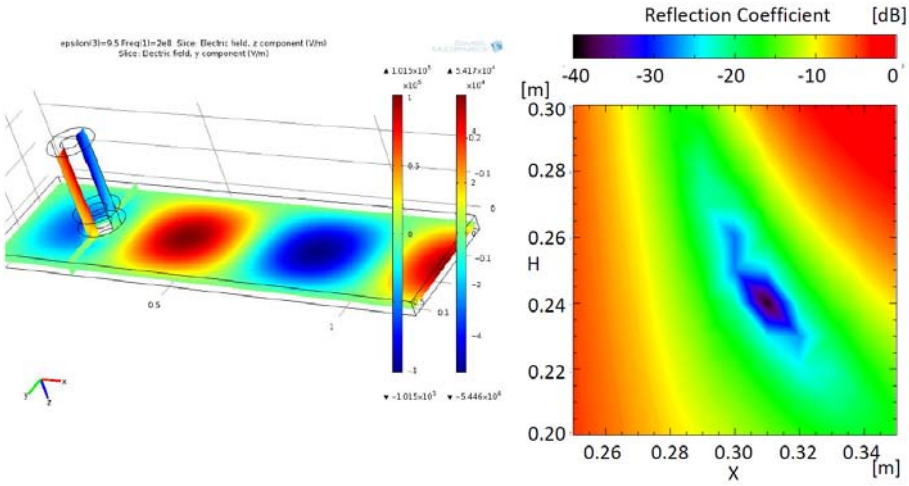

Figure 4.17: The dependence of the reflection coefficient of the coax-waveguide transition on the position of coaxial feeder x and the thickness of the alumina block H.

coaxial feeder position from the closed end of the waveguide (x) as shown in Fig. 4.17.

4.3.4 Electrostatically-Coupled Combline Antenna (ECC Antenna)

The grill antenna has an advantage that the launched $n_{\parallel}$ can be changed. However, the reflection coefficient became as high as 60 % under the low density plasma start-up operation condition, and the total input power was restricted to below 100 kW in order to avoid the arc discharge at the coax-waveguide transition. As a result the maximum coupled power in the start-up experiment was 40 kW. In addition, the number of the wave launching elements of the grill antenna is only four. Therefore, the $n_{\parallel}$-spectrum inevitably has a substantial reverse going peak other than the main peak intended for current drive. The height of the reverse going peak was one-third of the main peak for the case of $\pi/2$ phasing.

In order to overcome these difficulties associated with the grill antenna, a novel antenna called the electrostatically-coupled combline antenna (ECC antenna) was developed in a collaboration with Dr. Charles Moeller of General Atomics. This antenna is similar in principle to the (inductively-coupled) combline antenna. As can be seen in Fig. 4.18, this antenna consists of 13 vertically aligned metal rods. The shape of the rod and the covers surround-

ing the upper and lower parts of the rod were designed so that adjacent rods are electrostatically coupled. As a result, this antenna can excite the RF electric field aligned in the toroidal direction and excite the LHW directly. The phase difference between adjacent rods was set to be 60 degrees so that the launched $n_{\parallel}$ is 5.5. However, this antenna launches a backward wave, therefore the RF power is fed from the opposite end compared to the case of inductively-coupled combline antenna.

The reflection coefficient of this antenna was below 10 % and the power which exits through the output port was less than 1 %. Therefore, the fraction of the coupled power relative to the input power was much higher than that of the grill antenna or the combline antenna.

4.4 Non-inductive Plasma Start-up Experiment

Plasma start-up experiments using microwave power at 2.45 GHz were conducted previously in TST-2 [64]. The plasma was heated by electron cyclotron resonance heating. Initially, the plasma is confined in an open field line configuration by the magnetic mirror effect. A small net toroidal current can arise due to pressure driven effects [65–68]. The magnitude of the toroidal current generated by these effects is proportional to the plasma pressure, so the current increases as the plasma is heated. When the plasma current becomes large enough to cancel the applied vertical field on the inboard side of the torus, closed flux surfaces are formed. Once closed flux surfaces are formed, the fraction of confined electrons increase drastically, and the plasma current increases rapidly. This process is called the "current jump" [24].

In TST-2, not only ECH but also HHFW (21 MHz) was used for non-inductive start-up [69–71]. Sustainment of the ST configuration by HHFW after the formation of closed flux surfaces by ECH was demonstrated. Although the formation of closed flux surfaces was not achieved by HHFW alone, HHFW was able to provide heating and therefore current sustainment. The plasma current achieved in the plasma start-up experiments using ECH or HHFW was less than 2 kW.

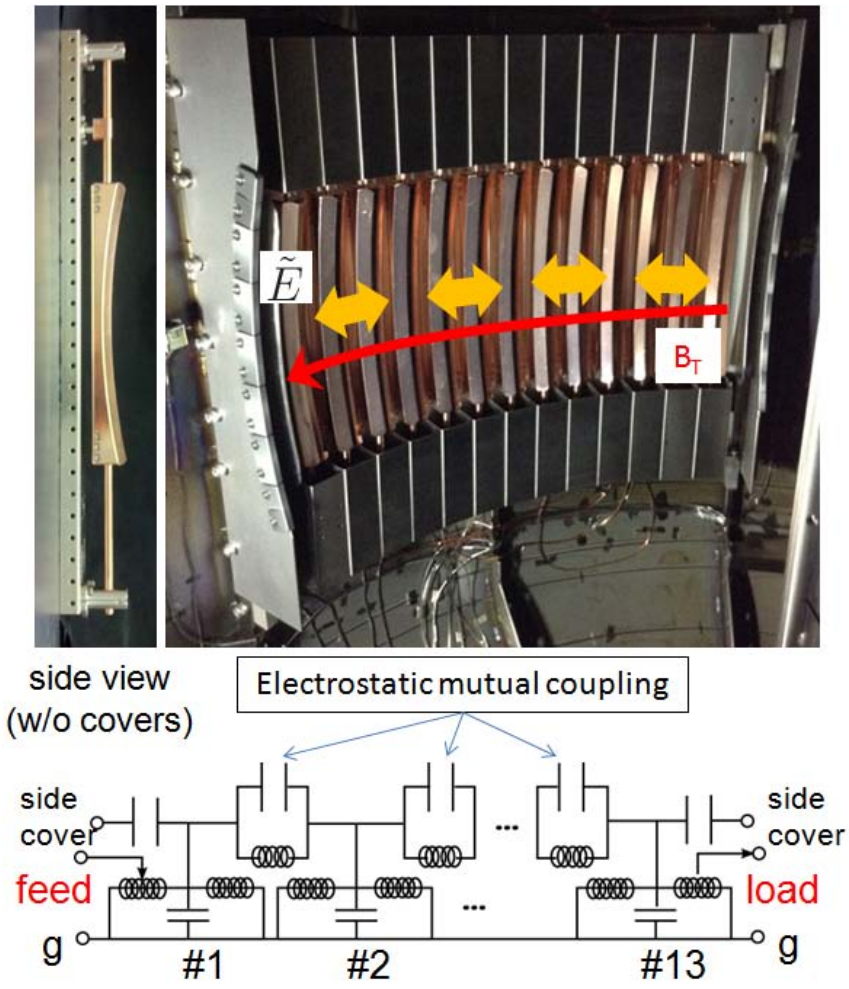

Figure 4.18: The ECC antenna. The top right figure shows the front view of the antenna. The red arrow indicates the direction of the toroidal magnetic field, and the orange arrows show the direction of the RF electric field excited by the antenna. The top left figure shows the side view of the antenna rod without the top and bottom covers. The bottom figure shows an equivalent circuit model of the ECC antenna.

Chapter 5

Antenna-Plasma Coupling Study

5.1 Linear Plasma Coupling Simulation

Antenna-plasma coupling of the dielectric-loaded waveguide array antenna was studied experimentally and theoretically. A linear plasma coupling simulation was performed using COMSOL under a simplified condition. The plasma density was assumed to be spatially constant and the toroidal curvature was ignored. Figure 5.1 shows the simulated reflection coefficient for different plasma densities and relative phases between adjacent waveguides. The reflection coefficient is high with the electron density less than 1×10^{16} m^{-3}. This density is much higher than the low density cutoff for the LHW, which is about 5×10^{14} m^{-3} for 200 MHz. This may be because the impedance mismatch from the dielectric-loaded waveguide to vacuum is very large. The reflection coefficient is less than 30 % for the density from 1×10^{16} m^{-3} to 1×10^{17} m^{-3} while increases again for the density more than 1×10^{17} m^{-3}. This is because there is no propagating mode for such a high density plasma as shown in Fig. 5.2.

5.2 Dependence on Input Power

The coupling characteristics of this antenna were investigated over a wide range of input power (fig. 5.3). The reflection coefficient for the grill antenna is defined as the ratio of the sum of the reflected powers to the sum of the input powers measured by directional couplers in coax-waveguide transitions connected to the four waveguides. The LHW was launched into an inductively sustained plasma. When the movable private limiter surrounding the

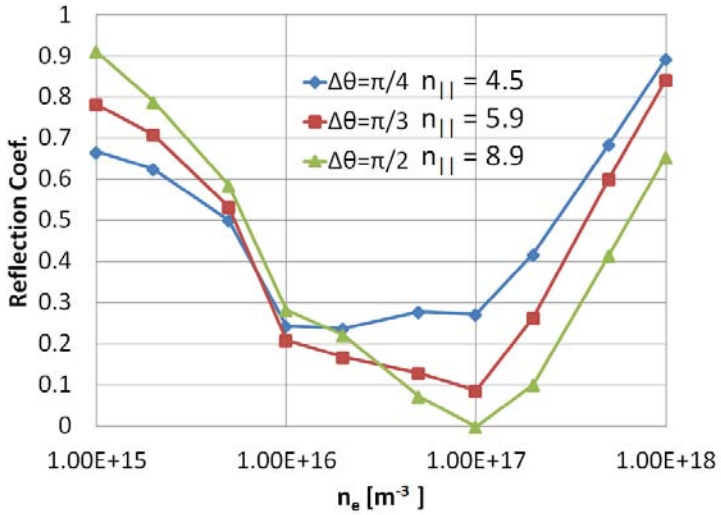

Figure 5.1: The dependence of the calculated reflection coefficient of the grill antenna on the electron density.

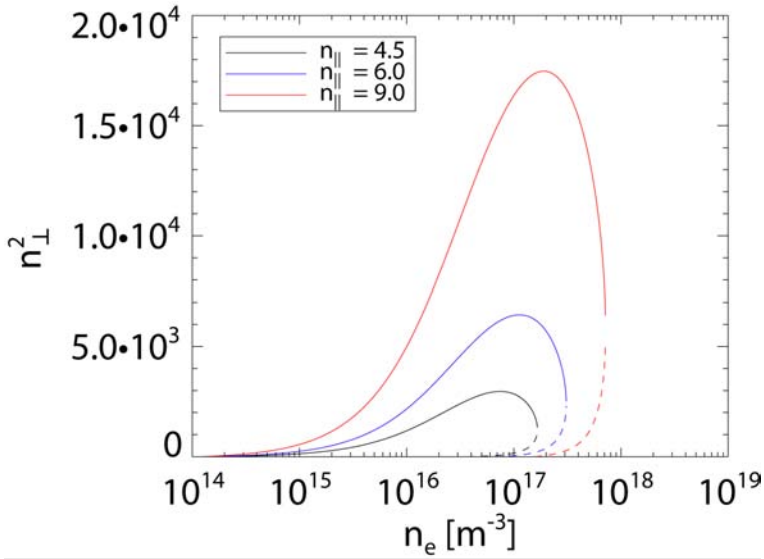

Figure 5.2: The $n_{\perp}^2$ dependence on plasma density for three deferent $n_{\parallel}$ is shown.

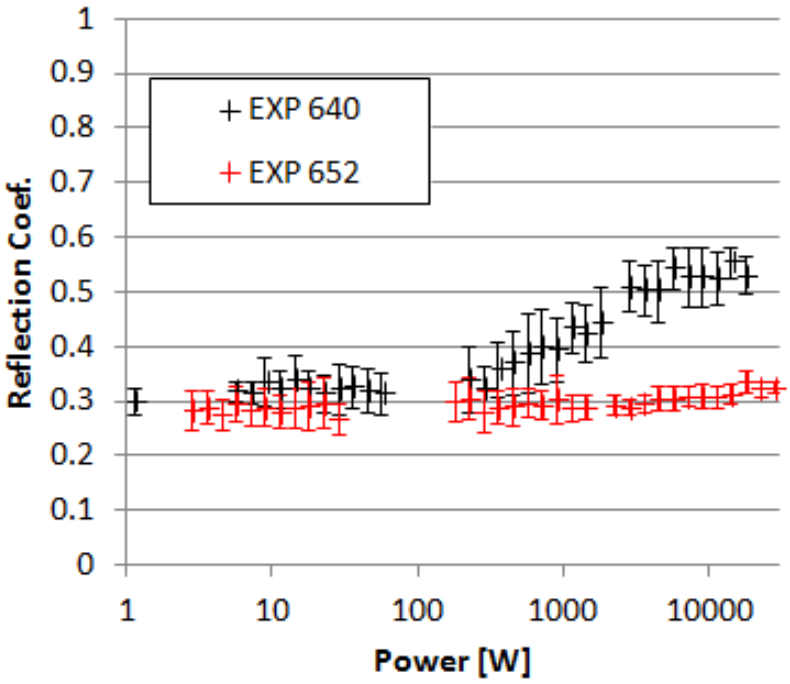

Figure 5.3: The dependence of the reflection coefficient on the input power.

grill antenna was placed 10 mm in front (towards the plasma) of the surface of the antenna, the reflection coefficient was greater than 50 % at high power, but decreased to 30 % at low power (less than 100 W). On the other and, when the private limiter was placed behind the antenna surface, this power dependence was not observed. This result can be explained by considering the ponderomotive force which is discussed in detail in next section.

5.3 Ponderomotive Force

The non-linear behavior of antenna-plasma coupling can be explained by the ponderomotive effect. The equation of motion for a particle of charge q is given by

$$m\frac{\mathrm{d}\boldsymbol{v}}{\mathrm{d}t} = q\left(\boldsymbol{E} + \boldsymbol{v} \times \boldsymbol{B}\right). \tag{5.1}$$

Neglecting the DC electric and magnetic fields, the $\boldsymbol{v} \times \boldsymbol{B}$ term becomes second order. The wave electric field can be written as

$$\boldsymbol{E} = \boldsymbol{E}(\boldsymbol{r}) \cos(\omega t). \tag{5.2}$$

In the first order, we can evaluate the electric field at the initial Position. Therefore,

$$m\frac{\mathrm{d}\boldsymbol{v_1}}{\mathrm{d}t} = q\boldsymbol{E}(\boldsymbol{r_0}) \cos(\omega t) \tag{5.3}$$

can be solved to obtain

$$\begin{aligned} \boldsymbol{v_1} &= \frac{q}{m\omega}\boldsymbol{E}(\boldsymbol{r_0}) \sin(\omega t), & (5.4)\\ \boldsymbol{r_1} &= -\frac{q}{m\omega^2}\boldsymbol{E}(\boldsymbol{r_0}) \cos(\omega t). & (5.5) \end{aligned}$$

In the next order, we can obtain the second order electric field by expanding $\boldsymbol{E}(\boldsymbol{r})$ about $\boldsymbol{r_0}$,

$$\boldsymbol{E}(\boldsymbol{r}) = \boldsymbol{E}(\boldsymbol{r_0}) + (\boldsymbol{r_1} \cdot \nabla)\boldsymbol{E} \mid_{\boldsymbol{r}=\boldsymbol{r_0}} . \tag{5.6}$$

To evaluate the $\boldsymbol{v_1} \times \boldsymbol{B_1}$ term, $\boldsymbol{B_1}$ is rewritten using Maxwell's equation $\nabla \times \boldsymbol{E} = -\partial_t \boldsymbol{B}$

$$\boldsymbol{B_1} = -\frac{1}{\omega}\nabla \times \boldsymbol{E}(\boldsymbol{r}) \mid_{\boldsymbol{r}=\boldsymbol{r_0}} \sin(\omega t). \tag{5.7}$$

Therefore, the second order terms of Eq. (5.1) satisfy

$$m\frac{\mathrm{d}\boldsymbol{v_2}}{\mathrm{d}t} = q\left[(\boldsymbol{r_1} \cdot \nabla)\boldsymbol{E} \cos(\omega t) + \boldsymbol{v_1} \times \left(-\frac{1}{\omega}\right) \nabla \times \boldsymbol{E} \sin(\omega t)\right], \tag{5.8}$$

where the spatial argument of $\boldsymbol{E}$ is suppressed for notational convenience. Substituting Eq. (5.4) and Eq. (5.5), we obtain

$$m\frac{\mathrm{d}\boldsymbol{v_2}}{\mathrm{d}t} = -\frac{q^2}{m\omega^2}\left[(\boldsymbol{E} \cdot \nabla)\boldsymbol{E} \cos^2(\omega t) + \boldsymbol{E} \times (\nabla \times \boldsymbol{E}) \sin^2(\omega t)\right]. \tag{5.9}$$

Averaging over time yields

$$\begin{aligned} m\left\langle \frac{\mathrm{d}\boldsymbol{v_2}}{\mathrm{d}t} \right\rangle &= -\frac{q^2}{2m\omega^2}\left[(\boldsymbol{E} \cdot \nabla)\boldsymbol{E} + \boldsymbol{E} \times (\nabla \times \boldsymbol{E})\right] \\ &= -\frac{q^2}{4m\omega^2}\nabla \boldsymbol{E}^2. & (5.10) \end{aligned}$$

Finally, the non-linear ponderomotive force is derived as

$$\boldsymbol{F}_{\mathrm{P}} = -\frac{q^2}{4m\omega^2}\nabla \boldsymbol{E}^2. \tag{5.11}$$

Figure 5.4: Electrostatic probe array installed on the inner wall of the private limiter.

As can be seen in Eq. (5.11), the ponderomotive force pushes charged particle towards the region of weaker electric field. Therefore, the ponderomotive force reduces the plasma density in front of the antenna where the intensity of electric fields is high. The antenna-plasma coupling can deteriorate if the plasma density becomes lower than the optimum density. The ponderomotive effect is counteracted by the rapid plasma transport along the magnetic field when the private limiter does not intersect magnetic field lines in front of the antenna. Therefore, the deterioration of coupling should be observed only when the private limiter intersects magnetic field lines in front of the antenna.

5.4 Density Measurements by the Limiter Probe

To confirm the density reduction by the ponderomotive force, electrostatic probes were installed on the inner wall of the private limiter (Fig. 5.4).

The applied voltage on the probe was swept from -250 V to $+50$ V at 1 kHz. The current flowing into the probe changes with the applied voltage. This current is measured as the voltage across a small shunt resistor betweeen the variable voltage source and the ground. The current vs. voltage trace (V-I characteristic, cf. Fig. 5.5) is analyzed to reveal information about the plasma. When the applied voltage is sufficiently negative (**Region I**), the current takes a constant value called the ion saturation current ($I_{\rm is}$). As the

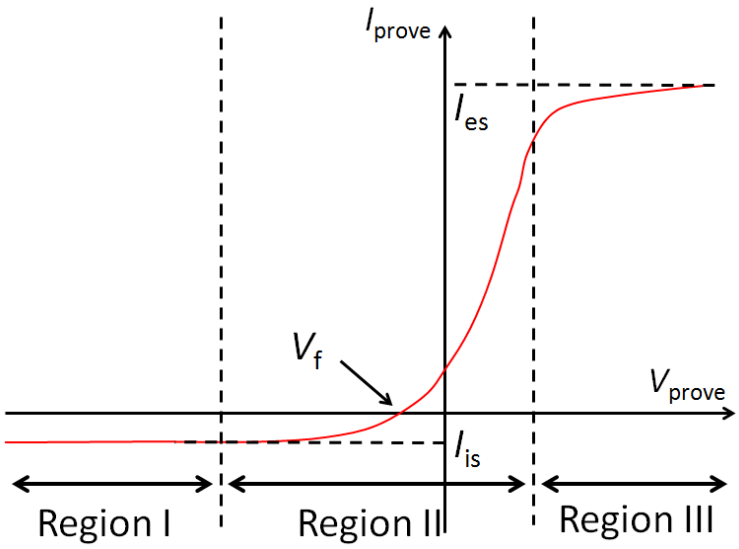

Figure 5.5: Schematic of the V-I characteristics.

probe voltage increases, the probe current becomes zero. This probe voltage is called the floating potential (V_f). When the probe voltage increases further, the probe current increases exponentially (**Region II**). This is because the number of electrons which can overcome the Coulomb barrier and reach the probe increases exponentially if the electron velocity distribution is Maxwellian. This exponential increase of the probe current saturates at the value called the electron saturation current (I_{es}) as the probe voltage approaches the space potential (V_s, **Region III**). However, because of the limit in the current supply capability of the variable voltage source, it is difficult to measure I_{es} in our experimental setup. In **Region II**, the probe current can be described as [72]

$$I_{probe} \propto \exp\left[\frac{eV_{probe}}{\kappa T_e}\right] \tag{5.12}$$

where e is electron charge, κ is the Boltzmann constant and T_e is the electron temperature. The electron temperature can be estimated from the slope of the $\ln(I_{probe})/V_{probe}$. The ion density n_i can be estimated from T_e and I_{is} because I_{is} is expressed as [72]

$$I_{is} = \frac{1}{2} e n_i A_p \sqrt{\frac{\kappa T_e}{m_i}} \tag{5.13}$$

where A_p is the probe area. The factor 1/2 varies depending on electron

emission from the electrode, the plasma sheath thickness, and the shape of the probe. Because of quasi-neutrality the electron density is equal to the estimated ion density, unless there is a large fraction of impurity ions.

The dependence of the estimated density on the input power is shown in Fig. 5.6. It is clearly seen that the density in front of the antenna decreases as the input power increases. In addition, the change in density starts around the same input power as where the reflection coefficients starts to increase. This result strongly suggests that the deterioration of reflection coefficient is caused by the density decrease due to the ponderomotive force of the applied RF electric field.

5.5 Non-Linear Antenna-Plasma Coupling Simulation

The experimental results described above were compared with the results of non-linear numerical simulation based on the finite element method (FEM). This simulation is similar to that performed using the POND code [73, 74]. As we discussed in Sec. 5.3, the ponderomotive force can be described as the gradient of a scalar potential, $\boldsymbol{F}_{\mathrm{P}} = -\nabla\Phi_{\mathrm{P}}$. This ponderomotive potential can be calculated for the wave field calculated by COMSOL using the formula [75, 76],

$$\Phi_{\mathrm{P}s} = \frac{q_s}{m_s}\left[\frac{|E_z|^2}{\omega^2} + \frac{|E_x|^2 + |E_y|^2}{\omega^2 - \Omega_s^2} + \mathrm{Im}\left\{\frac{\Omega_s({}^*E_yE_x - {}^*E_xE_y)}{\omega(\omega^2 - \Omega_s^2)}\right\}\right], \quad (5.14)$$

where it is assumed that $\boldsymbol{B_0} = B_0\hat{\boldsymbol{z}}$, and s stands for the species index. This form is derived from the second order term of the perturbative expansion of the Hamiltonian of the charged particle in the oscillating electromagnetic field,

$$H = \frac{1}{2m}(\boldsymbol{p} - q\boldsymbol{A})^2 + q\Phi, \quad (5.15)$$

where $\boldsymbol{A}$ and Φ are the magnetic vector potential and the electrostatic potential, respectively.

The ponderomotive force mainly acts on the electrons because of the mass dependence of Eq. (5.11). However, the electrostatic force acts to neutralize the plasma. Therefore, the total force felt by the electron is

$$\boldsymbol{F}_{\mathrm{e}} = -e\nabla\Phi_{\mathrm{es}} + \nabla\Phi_{\mathrm{Pe}} \quad (5.16)$$

where Φ_{es} is the electrostatic potential which appears as a result of the neutralizing effect.

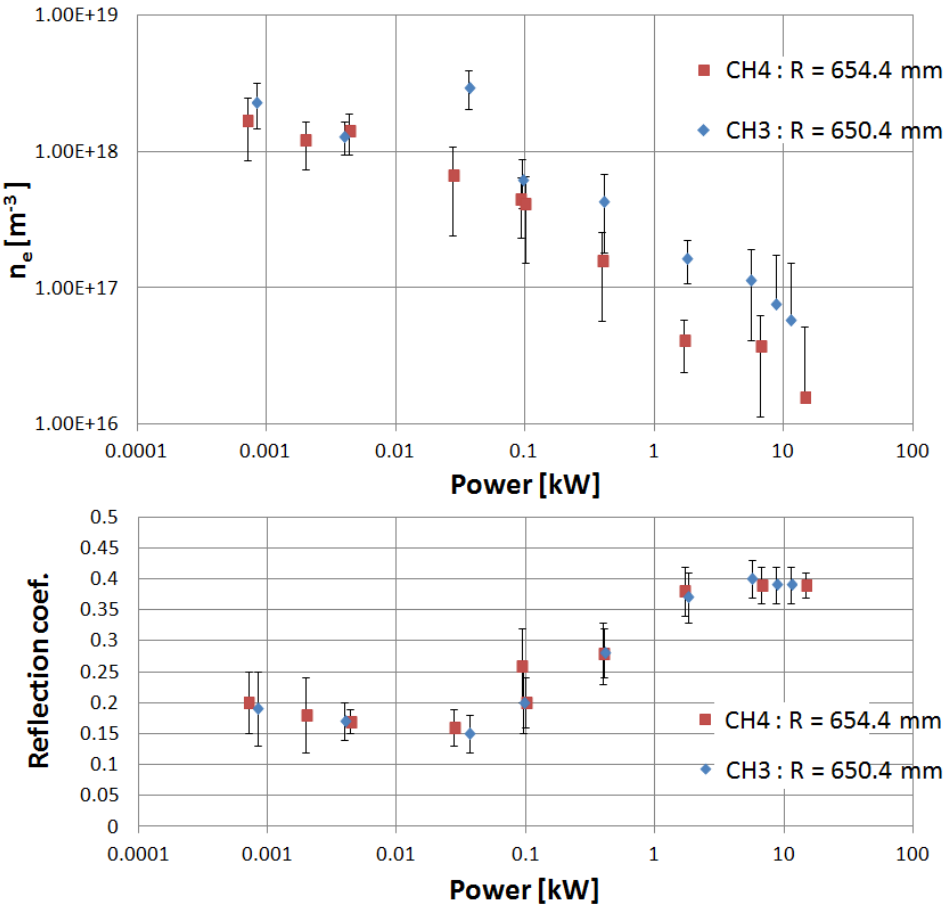

Figure 5.6: The dependences of the electron density and the reflection coefficient on the input power.

In equilibrium, the density of each species obeys the Boltzmann distribution,

$$n_s = n_{s0} \exp\left(-\frac{q_s \Phi_{\rm es} + \Phi_{{\rm P}s}}{\kappa T_s}\right), \tag{5.17}$$

where n_{s0} is the density of species s without the ponderomotive effect. Assuming quasi-neutrality (i.e. $n_{\rm i} = n_{\rm e}$), the electric potential can be written as

$$\Phi_{\rm es} = \frac{T_{\rm e}\Phi_{{\rm P}i} - T_{\rm i}\Phi_{{\rm P}e}}{eT_{\rm i} + q_{\rm i}T_{\rm e}}. \tag{5.18}$$

Therefore, the electron density can be expressed as

$$n_{\rm e} = n_{\rm e0} \exp\left(-\frac{q_{\rm i}\Phi_{\rm Pe} + e\Phi_{\rm Pi}}{\kappa(q_{\rm i}T_{\rm e} + eT_{\rm i})}\right). \tag{5.19}$$

Expanding this expression for small ponderomotive potential as $n_{\rm e} \sim n_{\rm e0}(1+\delta n)$, one can express the density reduction as

$$\delta n = -\frac{q_{\rm i}\Phi_{\rm Pe} + e\Phi_{\rm Pi}}{\kappa(q_{\rm i}T_{\rm e} + eT_{\rm i})}. \tag{5.20}$$

The benchmark of this simulation was performed comparing the density change for a certain electric field with the result shown in [77], which solves numerically the one dimensional MHD equation with RF electric field.

However, as the density in front of the antenna decreases, the reflection coefficient of the grill antenna increases. As a result, the electric field excited by the antenna decreases. Therefore, the iteration between the wave field calculation by COMSOL and the density reduction calculation based on the ponderomotive theory is needed to obtain a self consistent density profile for a certain input power. From the experimental result, the effect of rapid plasma transport along the magnetic field appears to be important, so the density is averaged along the magnetic field.

The result of simulation is shown in Fig. 5.7. The inflection point of the simulated reflection coefficient plotted versus the input power shifted towards higher power as the prescribed plasma temperature increased, because the change in density was determined from the equilibrium relationship between the plasma pressure force and the ponderomotive force. Compared with Fig. 5.3, the inflection point of the experimentally measured reflection coefficient was between 100 W and 1 kW. The corresponding temperature in the simulation was 5 – 10 eV. This result falls within the approximate range of electron temperature measured by the mid-plane Langmuir probe. This result strongly supports the explanation that the observed deterioration of

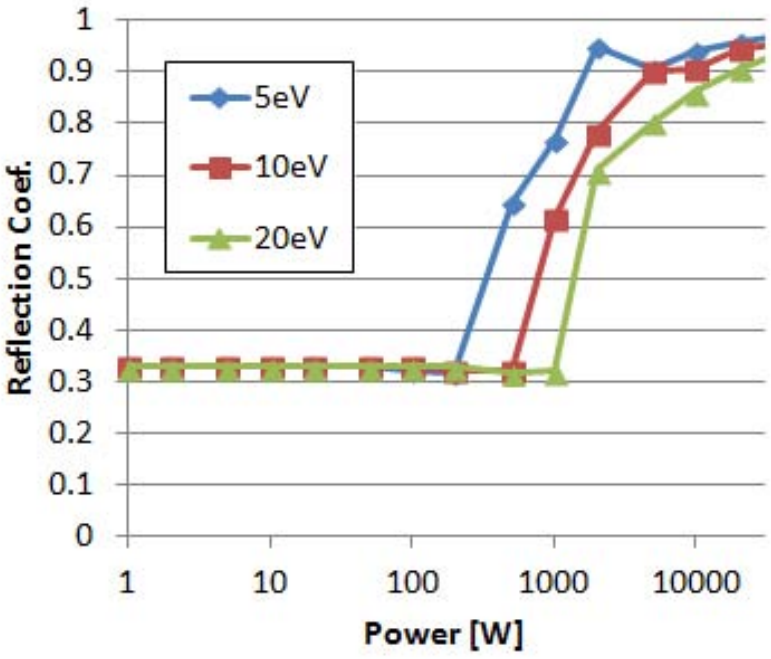

Figure 5.7: The simulated dependence of the reflection coefficient on the input power.

antenna-plasma coupling of the grill antenna is caused by the ponderomotive effect. The simulated reflection coefficient when the input power is more than several kW is more than 85 % while the experimental value is less than 60 %. This discrepancy might be caused by the edge plasma heating by the LHW.

Chapter 6

Plasma Start-up Experiments Using Three Types of Antennas on TST-2

Non-inductive plasma current start-up experiments using RF power in the lower hybrid frequency range is being conducted on the TST-2 spherical tokamak using three types of antennas: the (inductively-coupled) combline antenna, the grill antenna and the electrostatically-coupled combline (ECC) antenna .

6.1 Experiments Using the Combline Antenna

インターネット公表に関する使用承認が出版社から得られていないため、本節については、非公開。

「X-ray Measurements during Plasma Current Start-up Experiments using the Lower Hybrid Wave on the TST-2 Spherical Tokamak」
IEEJ Transactions on Fundamentals and Materials, 132 485 (2012).
(2012.7.1 No. 7, P485-489)

インターネット公表に関する使用承認が出版社から得られていないため、本節については、非公開。

「X-ray Measurements during Plasma Current Start-up Experiments using the Lower Hybrid Wave on the TST-2 Spherical Tokamak」
IEEJ Transactions on Fundamentals and Materials, 132 485 (2012).
(2012.7.1 No. 7, P485-489)

インターネット公表に関する使用承認が出版社から得られていないため、本節については、非公開。

「X-ray Measurements during Plasma Current Start-up Experiments using the Lower Hybrid Wave on the TST-2 Spherical Tokamak」
IEEJ Transactions on Fundamentals and Materials, 132 485 (2012). (2012.7.1 No. 7, P485-489)

インターネット公表に関する使用承認が出版社から得られていないため、本節については、非公開。

「X-ray Measurements during Plasma Current Start-up Experiments using the Lower Hybrid Wave on the TST-2 Spherical Tokamak」
IEEJ Transactions on Fundamentals and Materials, 132 485 (2012). (2012.7.1 No. 7, P485-489)

インターネット公表に関する使用承認が出版社から得られていないため、本節については、非公開。

「X-ray Measurements during Plasma Current Start-up Experiments using the Lower Hybrid Wave on the TST-2 Spherical Tokamak」
lEEJ Transactions on Fundamentals and Materials, 132 485 (2012).
(2012.7.1 No. 7, P485-489)

インターネット公表に関する使用承認が出版社から得られていないため、本節については、非公開。

「X-ray Measurements during Plasma Current Start-up Experiments using the Lower Hybrid Wave on the TST-2 Spherical Tokamak」
IEEJ Transactions on Fundamentals and Materials, 132 485 (2012). (2012.7.1 No. 7, P485-489)

インターネット公表に関する使用承認が出版社から得られていないため、本節については、非公開。

「X-ray Measurements during Plasma Current Start-up Experiments using the Lower Hybrid Wave on the TST-2 Spherical Tokamak」
IEEJ Transactions on Fundamentals and Materials, 132 485 (2012). (2012.7.1 No. 7, P485-489)

$\delta\theta$ [deg]	30	60	90	180
$n_\parallel$	3.0	6.0	9.0	18 (dipole phasing)

Table 6.2: The correspondence between the antenna phasing and the $n_\parallel$ of the launched LHW.

6.2 Experiments Using the Grill Antenna

6.2.1 Typical Waveforms

The plasma current start-up to 10 kA was demonstrated using the grill antenna as shown in Fig. 6.5. The advantage of this antenna over the combline antenna is that this antenna can launch the LHW directly with $n_\parallel$ varied from -18 to $+18$ by changing the phase difference between adjacent waveguides. The correspondence between the antenna phasing and the $n_\parallel$ of the launched LHW is shown in table 6.2. The main objective of the experiments using the grill antenna is to search the most favorable $n_\parallel$ for the plasma current start-up in the TST-2. Therefore, the dependence of the achieved plasma current on the antenna phasing was studied for several discharge sequence and the X-ray emission in these experiments were also compared.

6.2.2 Dependence on the Phase Difference

Plasma Current and Soft X-ray Emission

Non-inductive plasma current start-up was attempted with several different phasings at relatively low plasma current (7 kA). Figure 6.6 shows the dependence of the achieved plasma current on antenna phasing. The waveform of the externally applied vertical field coil current was kept the same during this phasing scan while the input power was varied from 4 kW to 15 kW. The negative value in $n_\parallel$ denotes the counter drive case. Plasma currents greater than 3 kA were not achieved for the counter drive case in this scan. This result again shows that the effect of direct current drive by the LHW is important to achieve plasma currents greater than 4 kA in TST-2.

In order to investigate the dependence in the co drive case, plasma start-up to 10 kA was attempted. In this case, the mean value of the input power was 15 kW and the variation of the input power for different discharges was kept to less than 35 %. As clearly seen in Fig. 6.7, the highest plasma current was obtained for $1.5 \leq n_\parallel \leq 4.5$. The strength of SX emission in the energy range 0.1–1 keV also took its highest value for $1.5 \leq n_\parallel \leq 4.5$ while thatin the energy range 1–10 keV showed a monotonic decrease as $n_\parallel$ increases. This

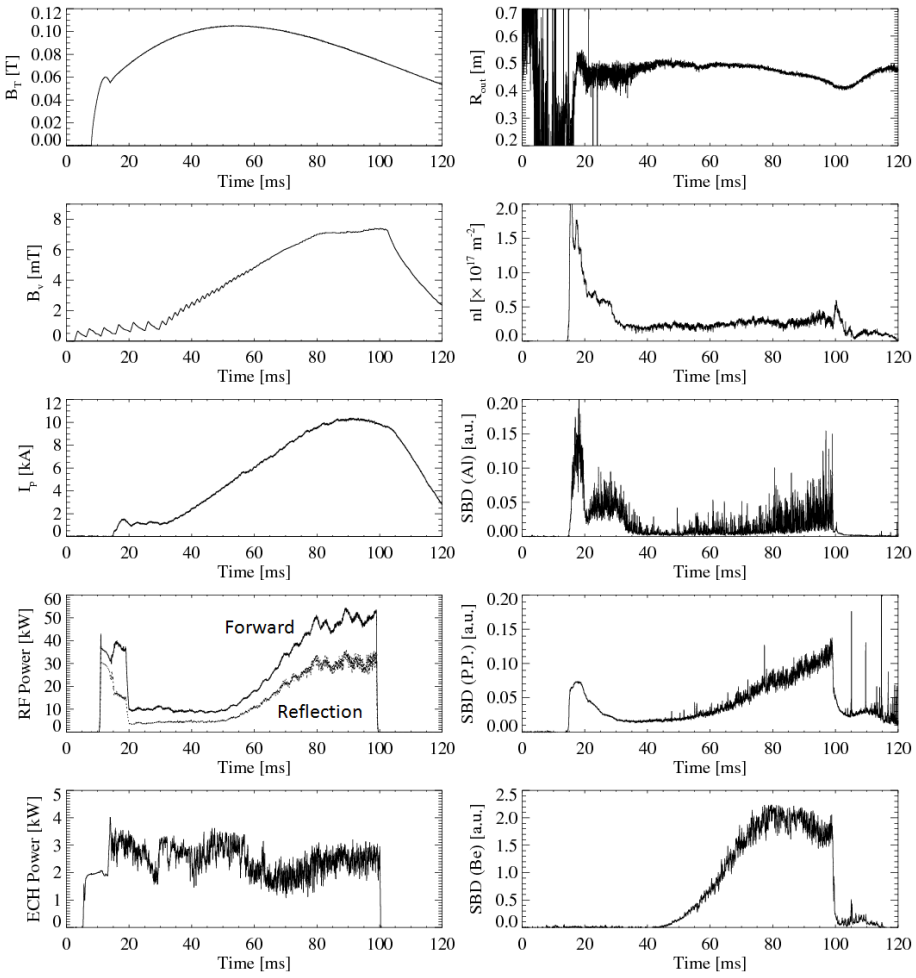

Figure 6.5: Typical discharge waveforms of the plasma start-up experiments using the grill antenna.

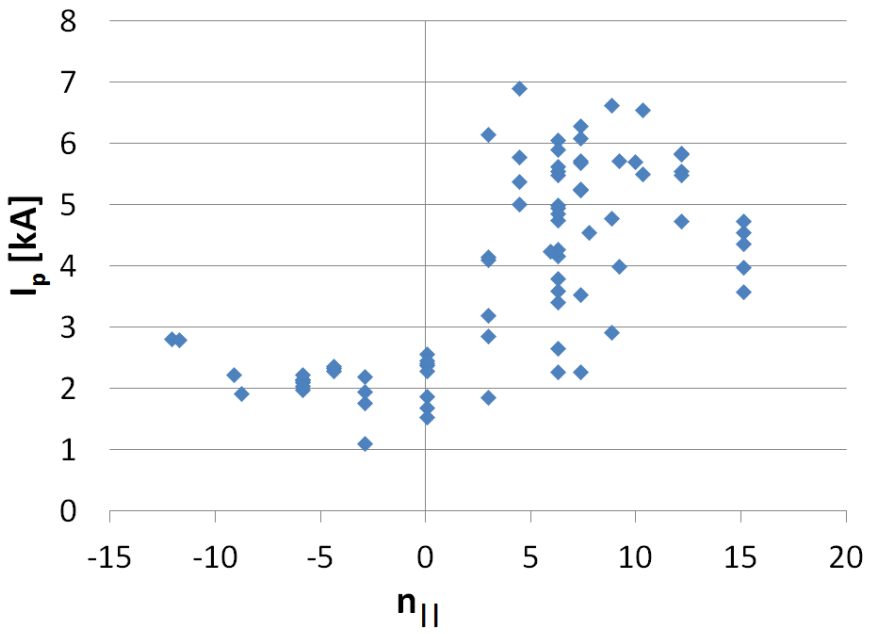

Figure 6.6: Dependence of the achieved plasma currnt on antenna phasing.

is because the LHW with lower $n_{\|}$ can interact with higher energy electrons. The higher energy electrons take longer to slow down to become bulk thermal electrons. Therefore, the LHW with lower $n_{\|}$ is thought to drive more current by producing higher energy electrons.

Hard X-ray Spectrum

This hypothesis is confirmed by the measured spectrum of tangential HX emission. Figure 6.8 shows the HX spectra averaged over 5 shots for each $n_{\|}$ shown in Fig. 6.7. The sight line lies along a tangential chord and the detector is oriented to detect HX emitted from high energy electrons accelerated in the co-direction. The count rate of high energy photons was lower when $n_{\|}$ of the launched wave was greater than 7.5. As stated above, the input power was kept at a certain level but the plasma current differed in this comparison. Therefore, there is a possibility that the drop in HX emission at high energies might have been caused by the deterioration of high energy electrons confinement because of the lower poloidal field strength.

Another phasing scan was performed to investigate whether the difference in the HX spectrum could be measured with almost the same poloidal field (or plasma current). As can be seen in Fig. 6.9, the input power was increased in

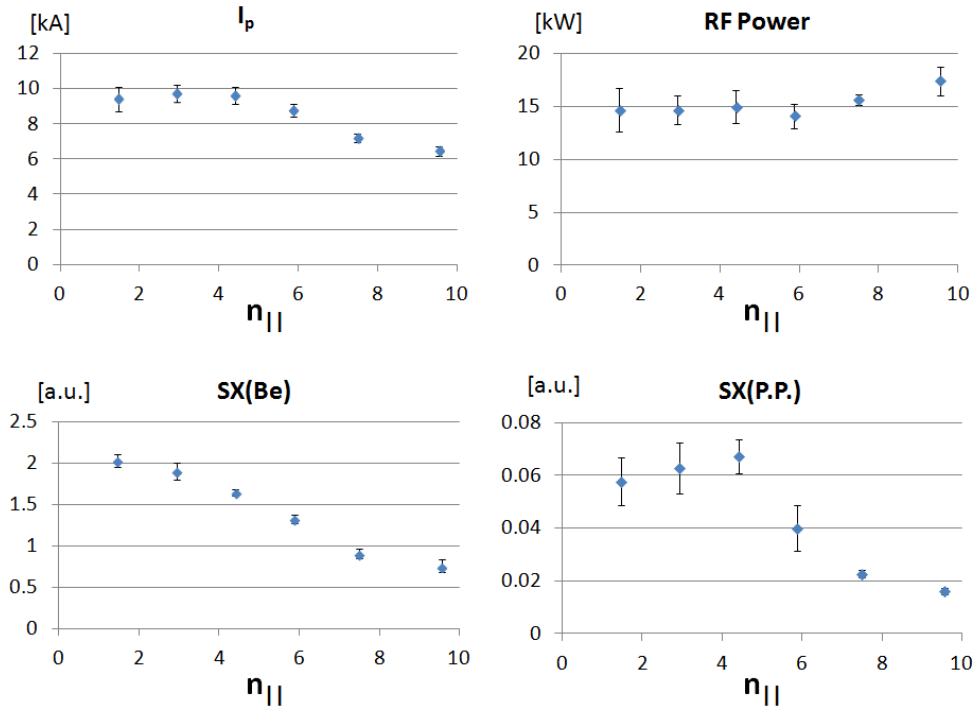

Figure 6.7: Dependences of the achieved plasma currnt and SX emission on Antenna phasing.

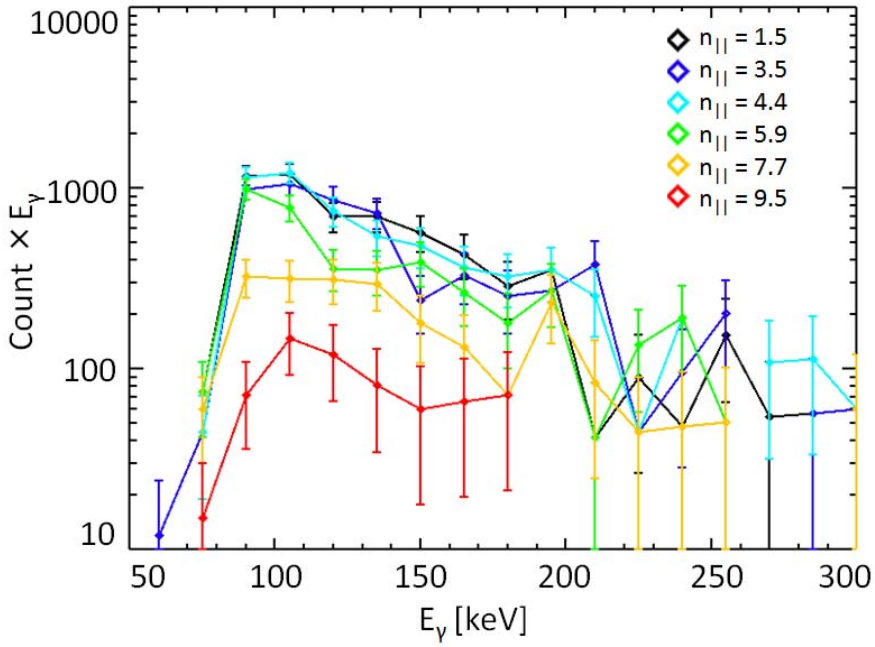

Figure 6.8: Comparison of hard X-ray spectra obtained for different antenna phasings.

$n_\parallel$	$T_{\mathrm{eff,co}}$	$T_{\mathrm{eff,ctr}}$
3.0	58±3 keV	52±10 keV
6.0	56±3 keV	53±9 keV
7.5	40±7 keV	-

Table 6.3: The effective temperatures of the HX energy spectra for different launched $n_\parallel$.

order to maintain the same plasma current in cases with higher launched $n_\parallel$. The emission in the counter direction was also measured in this experiment. Since only one NaI scintillator was available at that time, the direction of the sight line was changed alternatively for every 3 discharges. The HX counts were accumulated for 13 shots for every antenna phasing and for both sight lines.

The measured HX spectra and the fitted effective temperatures for different launched $n_\parallel$ are shown in Fig. 6.10 and table 6.3. Firstly, for all launched $n_\parallel$, the emission in the co direction was stronger than that in the counter direction. This is a clear evidence that the LHW created an asymmetry in the electron velocity distribution function. Secondly, the decreases in the emitted photon energy and the effective temperature can be seen for $n_\parallel = 7.5$. From this result, we can conclude that the launched $n_\parallel$ of less than 6 is favorable for creating high-energy electrons in the co-direction, which is thought to account for a large fraction of the plasma current in TST-2 non-inductively driven plasmas.

The higher effective temperature of the HX energy spectrum compared with the bulk electron temperature accounts for the existence of a plateau in the electron velocity distribution function. Although the difference between effective electron temperatures measured in co and counter directions seemed not to be very different in this experiment, the total counts of counter HX emission was not sufficient to obtain the effective temperature accurately. The effective temperatures of the co HX radiation for $n_\parallel = 3$ and 6 were almost the same as that measured in the experiment using the combline antenna.

Power Modulation Experiments

Amplitude modulation experiments were performed using the grill antenna. The same model of plasma response to LHW amplitude modulation as that used to analyze the combline antenna experiment was used. The relative phases of SX signals to the LHW amplitude modulation are shown in Fig. 6.11.

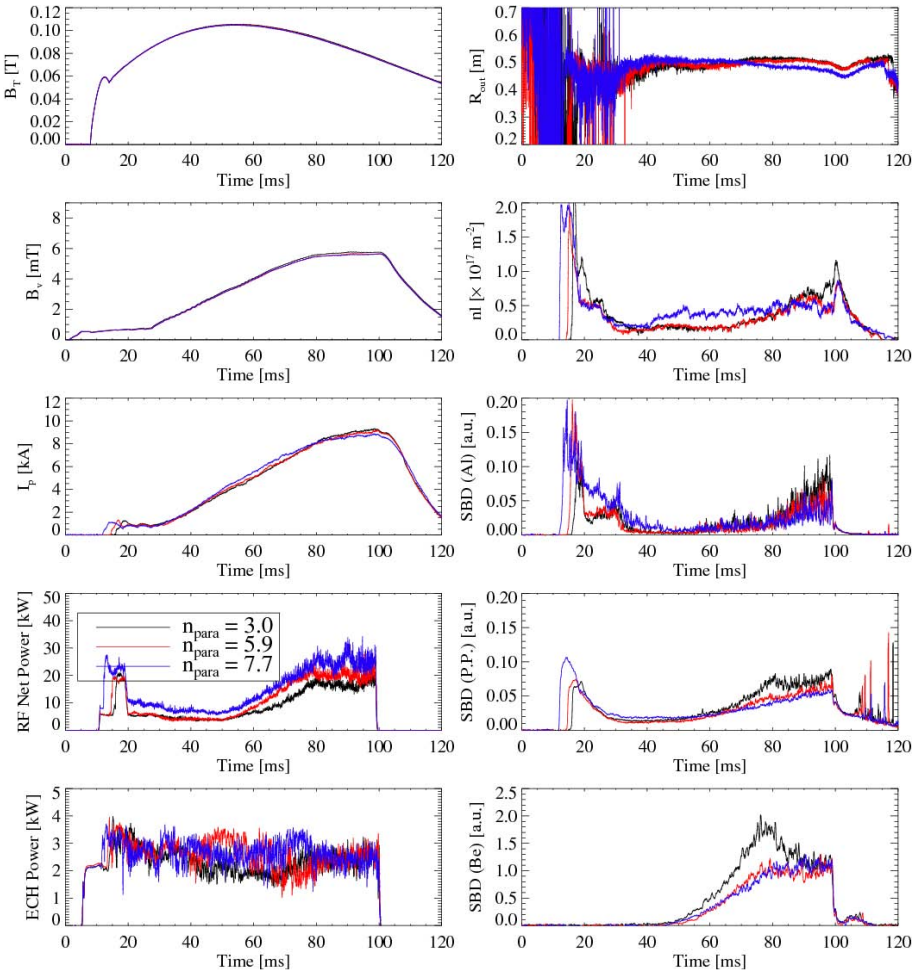

Figure 6.9: Discharge waveforms for HX spectrum comparison at the same plasma current. The black, red and blue traces indicate the discharges with $n_{\parallel}$=3.0, $n_{\parallel}$=5.9 and $n_{\parallel}$=7.7.

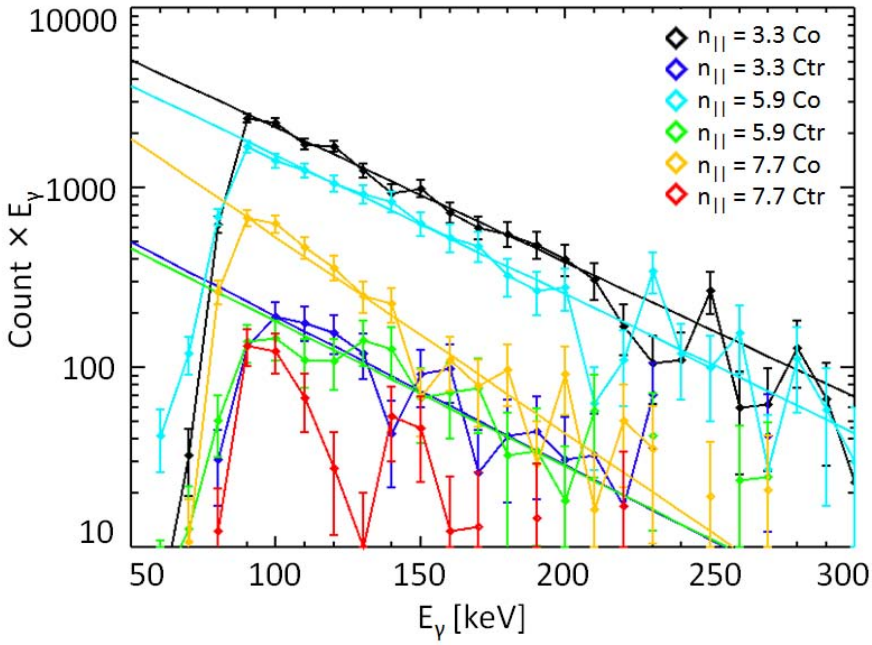

Figure 6.10: Comparison of HX spectra measured in co and counter directions for 3 antenna phasings.

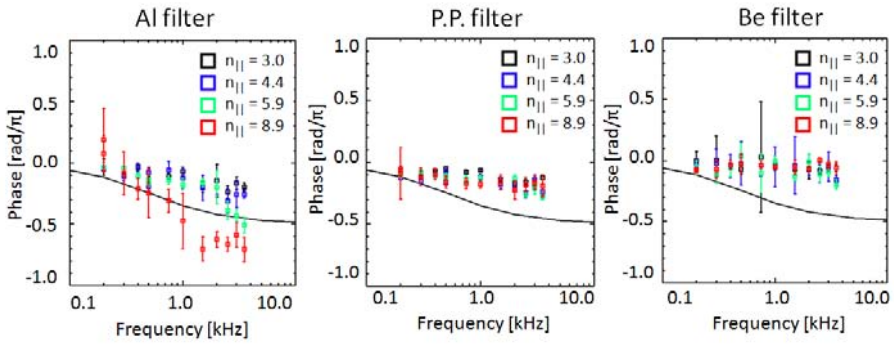

Figure 6.11: Phases of modulated SX signals in three energy ranges relative to RF modulation. The left, center and right figures indicate the relative phase of SX signals measured by the SBD with no additional filter, with the polypropylene filter and with the beryllium filter, respectively.

The relative phase was measured for three energy ranges and four launched $n_{\parallel}$'s with AM frequency from 0.2 kHz to 3.5 kHz. However, a definite delay in the AM phase of the SX signal was observed only in the lowest energy component measured by the SBD with no additional filter for the case with $n_{\parallel} = 9$. For this case, the inflection point of the relative phase plotted against the logarithm of AM frequency fell around 0.5 kHz. From this result, the timescale for the loss of electrons which emit low energy photons measured by the SBD with no additional filter was estimated to be 0.3 ms. This timescale is of the same order as the electron-ion collision time of 50 eV electrons in a plasma with a density $10^{17}\mathrm{m}^{-3}$, which is 0.6 ms. On the other hand, all the other SX signals did not show any delay in relative phase. This result indicates that the electrons which emit these photons are lost very quickly, in less than 50 μs. This rapid loss can be attributed to the orbit loss because of the deviation of the electron orbit from the flux surface. As stated above, the size of the drift orbit for a 10 keV electron is approximately 30 mm, while a typical minor radius of the plasma is 250 mm. Therefore, a certain fraction of energetic electrons would be created near the plasma edge. This tendency did not change for the launched $n_{\parallel}$ in the range from 3 to 9. The absorption profile of the LHW might change with $n_{\parallel}$. However, if the single-pass absorption were very weak, the absorption profile would become broad and insensitive to the launched $n_{\parallel}$ because absorption would depend on up-shift or down-shift of $n_{\parallel}$ while propagating inside the plasma. As a result, a certain fraction of the LHW power would be absorbed at large normalized radii, and energetic electrons accelerated by the LHW would be lost quickly.

6.3 Experiments Using the ECC Antenna

6.3.1 Typical Waveforms

Plasma start-up experiments using the ECC antenna were performed after experiments using the grill antenna and the combline antenna. From the experimental results using the grill antenna, it became clear that the antenna which can excite the LHW directly with $n_{\parallel}$ less than 6 would be favorable to initiate the plasma current in TST-2. The ECC antenna can excite the LHW with $n_{\parallel} = 5.5$ with relatively sharp wavenumber spectrum because this antenna has 13 elements while the grill antenna has only 4 elements. In addition, the antenna-plasma coupling characteristics of this antenna is the best among the three antennas. The reflection coefficients of this antenna is less than 10 % and the power that exits from the output port is negligibly small (much less than 1 %). Therefore, more than 85 % of the input power can be delivered to the plasma. However, the input power has been restricted to less than 30 kW so far because of impurity production. This antenna was installed on TST-2 in the spring of 2013. An extensive antenna conditioning would be required to increase the input power. Up to now, plasma current initiation and ramp-up to 12 kA has been demonstrated using the ECC antenna, as shown in Fig. 6.12.

6.3.2 Hard X-ray Spectrum

The HX spectrum was measured in discharges with plasma currents of approximately 10 kA. Figure 6.13 compares the spectra of HX radiation for co and counter directions. Again, the HX radiation in the co direction is stronger than that in the counter direction, which means that the LHW created an asymmetric electron distribution function. The effective temperature of the HX radiation was 27.6 keV, which is less than that measured in experiments using the grill antenna or the combline antenna. The higher density which is caused by insufficient conditioning of the antenna might account for this difference.

6.4 Comparison Among Different Antennas

6.4.1 Comparison of the Current Drive Efficiency

We performed plasma current start-up experiments using three types of antennas. Each antenna has its own feature and the achieved plasma current differs. Although the highest plasma current was achieved using the combline

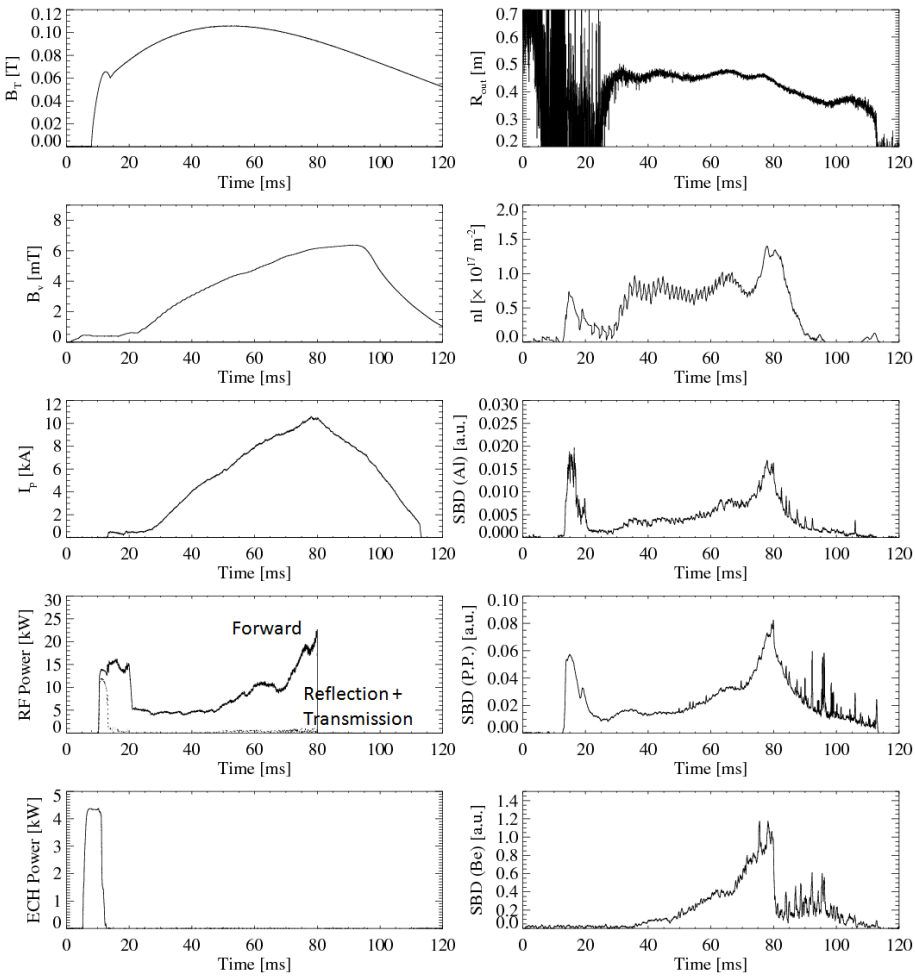

Figure 6.12: Typical waveforms of a start-up experiment using the ECC antenna.

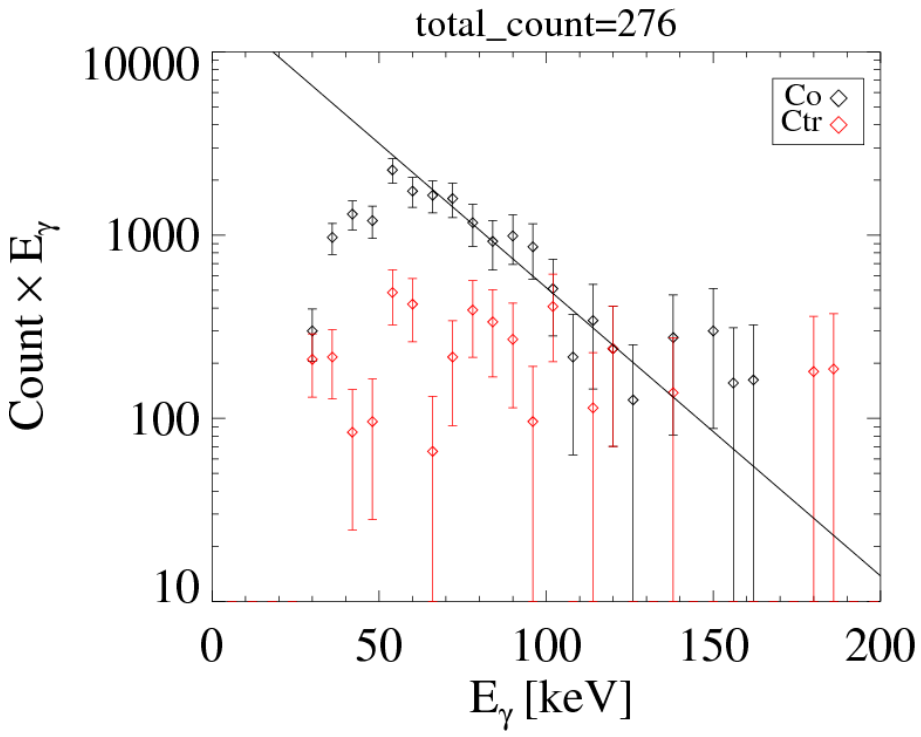

Figure 6.13: Hard X-ray spectra in the experiment using the ECC antenna. The HX radiation in the co direction (indicated by black symbols) is stronger than that in the counter direction (indicated by red symbols), which means that the LHW created an asymmetric electron distribution function.

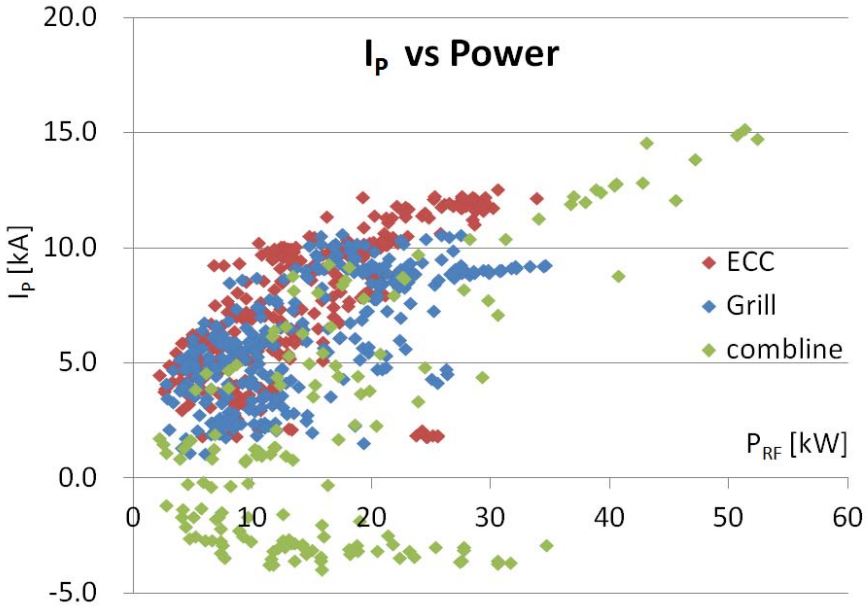

Figure 6.14: Comparison of plasma currents achieved with the three antennas plotted versus the input RF power.

antenna, this might be attributed to the highest available power. As can be seen in Fig. 6.14, 15 kA was achieved in the combline antenna experiment with an input power of 50 kW. The available power in the grill antenna experiment was limited to less than 35 kW to avoid arcing in the coax-waveguide transition section. The ECC antenna did not have such a restriction in the input power, but bursts in the plasma density and the H-α radiation were observed for input powers exceeding 30 kW. This implies that impurity and/or neutral gas influx from the antenna became non-negligible, and effective current drive was not possible in this regime.

In order to compare the current drive ability in tokamak devices, the current drive figure of merit $\eta_{\mathrm{CD}} = \bar{n}_{\mathrm{e}} R I_{\mathrm{p}} / P_{\mathrm{LH}}$ is widely used [17, 21]. This parameter normalizes the effects of the device size and the plasma density. In fact, the value of the driven current per input RF power is not exactly inversely proportional to the density, but this figure of merit takes into account the deterioration of the current drive ability at higher density due to the faster slowing down of high energy electrons.

Figure 6.15 compares η_{CD} achieved with three antennas against the plasma current. η_{CD} increases as the plasma current increases for all three antennas. This tendency can be attributed to the improvement of high energy electron

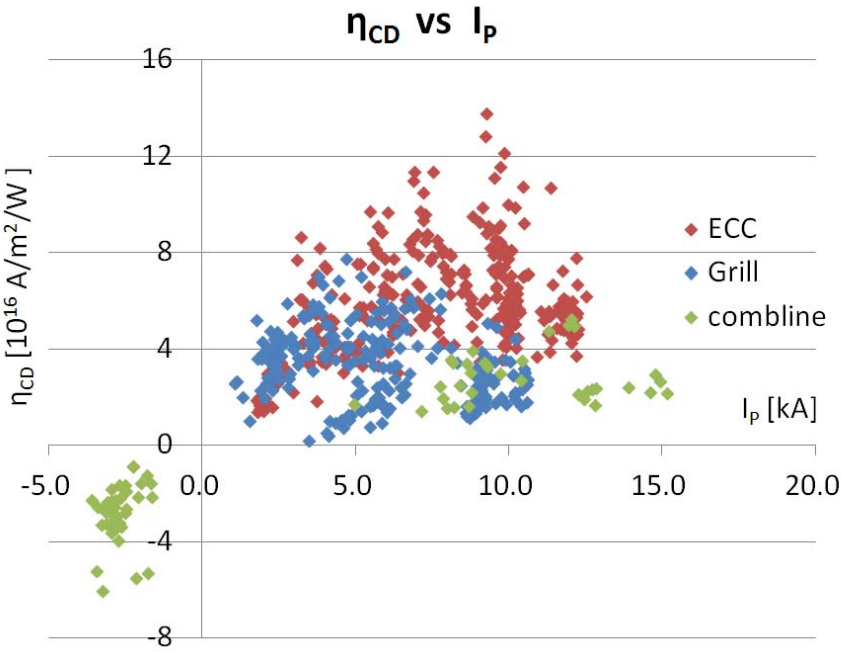

Figure 6.15: Comparison of the current drive figure of merit η_{CD} achieved with the three antennas plotted versus the plasma current.

confinement with the increase of the poloidal field strength. In addition, the bulk electron confinement also improves with the poloidal field. This may also lead to higher electron temperatures, which improves the absorption of the LHW. This is another possible cause of improved η_{CD}.

Among the three antennas, η_{CD} was the lowest for the combline antenna even though the highest plasma current was achieved by this antenna. This is because the combline antenna was designed for excitation of the FW. The LHW is an electrostatic wave, and an antenna suitable for LHW excitation should excite RF electric field aligned with the confining magnetic field, but the combline antenna excites RF electric field perpendicular to the confining magnetic field (RF magnetic field parallel to the confining magnetic field). Therefore, excitation of the LHW by the combline antenna relies on the small parallel magnetic component of the LHW and is not expected to be efficient.

The grill antenna has higher η_{CD} than the combline antenna. This result is attributed to the ability of the grill antenna to excite the LHW with suitable polarization. The highest η_{CD} on TST-2 was achieved using the ECC antenna, which can also excite the LHW with the toroidal electric field. One difference between the grill antenna and the ECC antenna is the

launched $n_{\parallel}$. The launched $n_{\parallel}$ of the grill antenna can be varied from -18 to $+18$ while that of the ECC antenna is fixed at 5.5. Another difference is the number of antenna elements. The grill antenna consists of only 4 antenna elements while the ECC antenna has 13 elements. Therefore, the peak of the $n_{\parallel}$-spectrum of the grill antenna is broader than that of the ECC antenna. In addition, the $n_{\parallel}$-spectrum of the grill antenna has the reverse going peak, whose height is one-third of the main peak, while that of the ECC antenna is less than 10 %.

If the absorption of the LHW were strong, most of the power is absorbed in the first pass through the plasma, and the absorption profile is strongly dependent on the launched $n_{\parallel}$ spectrum. In that case, η_{CD} of the grill antenna could be greater than that of the ECC antenna. As stated in the preceding section, no clear difference in the HX energy spectrum was observed when the launched $n_{\parallel}$ was less than 6. This result suggests that the absorption of the LHW is weak and multiple passes through the plasma are required for sufficient absorption. In such a case, absorption should not depend sensitively on the launched $n_{\parallel}$ spectrum. Therefore, even though the launched $n_{\parallel}$ of the ECC antenna is fixed at 5.5, this antenna could drive the plasma current more efficiently because the reverse going wave component, which drives the current in the reverse direction, is much weaker.

Chapter 7

Discussion and Conclusions

7.1 Discussion

7.1.1 Difficulty in Using the Grill Antenna at Low Frequency

In other experiments which use the grill antenna, the ponderomotive effect is usually not critical, especially at input powers as low as several kW [79–84]. A possible explanation of this difference lies in the difference in the RF frequency. As can be seen from Eq. (5.14), the ponderomotive potential is inversely proportional to the square of the RF frequency. Typical frequencies of the LHW used in conventional tokamaks are in the range of several GHz because of their higher magnetic fields. On the other hand, the frequency used on TST-2 is 200 MHz. Therefore, the ponderomotive potential is roughly 2 orders of magnitude larger than in conventional tokamak experiments while the edge plasma temperature is on the same order as in other experiments. As a result, the fraction of density reduction becomes negligibly small for the same input power density according to Eq. (5.20). However, the ponderomotive effect cannot be dismissed in almost all experiments when their maximum powers are used since it is empirically known that the attainable RF power density of the grill antenna scales as the square of the frequency [85–88].

Another possible cause of deterioration at low power is the effect of the dielectric. The energy density of the electric field in the waveguide is enhanced because of the high relative permittivity of the dielectric material. This leads to a stronger ponderomotive effect in front of the antenna compared with the grill antenna without a dielectric material. In addition, the large impedance mismatch from the dielectric-loaded waveguide to vacuum

causes antenna-plasma coupling to deteriorate at much higher densities than the cutoff density.

7.1.2 Estimation of the Fast Electron Density

The measured HX spectrum represents the fast electron velocity distribution function. We assume a spatially uniform 1-D (zero perpendicular velocity) Maxwellian distribution function with asymmetric temperatures in the "Co" and "Counter" directions for fast electrons, which can be expressed as

$$f(p_\parallel) = \begin{cases} \exp\left(-\frac{p_\parallel^2}{2m_e k_\mathrm{B} T_\mathrm{Co}}\right), & (p_\parallel \geq 0) \\ \exp\left(-\frac{p_\parallel^2}{2m_e k_\mathrm{B} T_\mathrm{Ctr}}\right), & (p_\parallel < 0). \end{cases} \tag{7.1}$$

The emission intensity is calculated using the differential cross section labeled "2BN" in [61]. A comparison of the measured HX spectra in the experiment using the combline antenna and the calculated HX spectra using the assumed fast electron velocity distribution function are shown in Fig. 7.1. The assumed fast electron density and ion density are $n_\mathrm{fast} = 2 \times 10^{15}\mathrm{m}^{-3}$ and $n_\mathrm{i} = 1 \times 10^{17}\mathrm{m}^{-3}$, respectively, and the assumed parallel fast electron temperatures in the co and counter directions are $T_\mathrm{Co} = 80$ keV and $T_\mathrm{Ctr} = 50$ keV, respectively. The measured HX intensity in the energy range less than 100 keV drops because pulses with photon energies less than 100 keV are easily hidden by the preamplifier noise. The asymmetry in the co vs. counter directions results in the plasma current driven by the fast electrons accelerated by the LHW. The current density calculated for the assumed velocity distribution is 12 kA/m^2, which corresponds to the plasma current of 2.4 kA, assuming a circular plasma cross section with a minor radius of 0.25 m. Since this estimate uses a simple model with uniform spatial distribution and zero perpendicular velocity, the uncertainty in the estimated fast electron density and plasma current can easily be several times.

7.1.3 Analysis of Orbit Loss Using a Fokker-Planck Code

As mentioned in Chapter 6, the orbit loss of fast electrons is believed to be significant in the low-current start-up plasma created by the LHW. This assumption is confirmed by calculations using the CQL3D Fokker-Planck code. The orbit loss is calculated in CQL3D using the simple banana model. In this model, a trapped particle is considered lost when its banana width

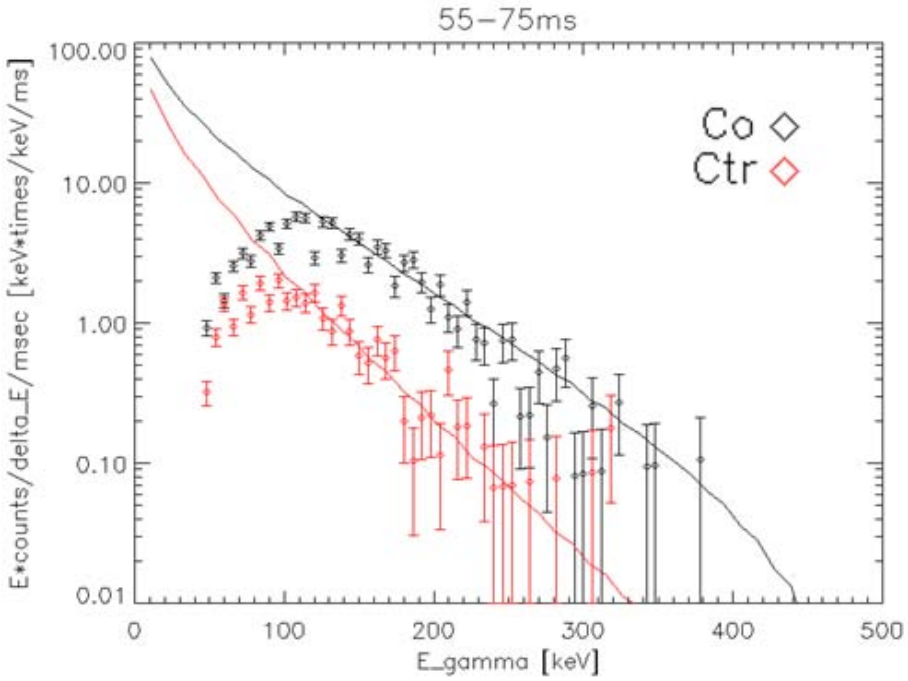

Figure 7.1: Comparison of the measured HX spectra in the experiment using the combline antenna (diamonds) and the calculated HX spectra using assumed fast electron velocity distribution function (solid lines). The assumed values of the fast electron density and ion density are $n_{\rm fast} = 2 \times 10^{15} {\rm m}^{-3}$ and $n_{\rm i} = 1 \times 10^{17} {\rm m}^{-3}$, respectively, and the assumed parallel fast electron temperatures in the co and counter directions are $T_{\rm Co} = 80$ keV and $T_{\rm Ctr} = 50$ keV, respectively.

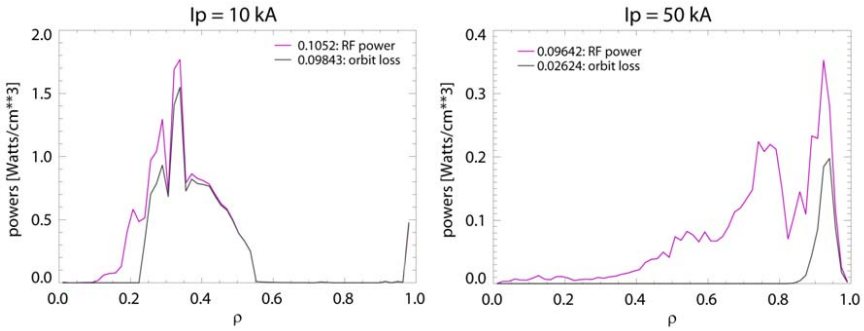

Figure 7.2: Comparison of the energy lost by orbit loss for plasma currents of 10 kA and 50 kA.

plus gyro-orbit width becomes greater than the distance to the plasma edge, and a circulating particle is considered lost when its gyro-orbit width becomes greater than the distance to the plasma edge.

A comparison of the energy lost by the orbit loss for plasma currents of 10 kA and 50 kA is shown in Fig. 7.2. The orbit loss is significant for normalized minor radius of greater than 0.2 for the 10 kA case. This calculation strongly supports the assumption that the estimated rapid loss of high energy electrons is attributed to the orbit loss.

On the other hand, the orbit loss is comparable to the RF power source only for normalized minor radius of greater than 0.9 for the 50 kA case. Therefore, a further improvement in the current drive efficiency can be achieved if the plasma current could be increased.

7.1.4 Start-up Scenario Keeping Low Density

The density profile was reconstructed for a 9 kA discharge obtained using the grill antenna by inverting the measured line integrated densities measured along four vertical chords, as shown in Fig. 7.3. Accessibility of the LHW to the plasma core is ensured for this operation. As shown in Fig. 6.5, the plasma density was able to be kept at almost constant level while the plasma current was ramped up from 1 kA to 10 kA for the plasma start-up operation using the grill antenna, which indicates that it is possible to start and ramp up the plasma current keeping the plasma density low.

A lower plasma density is favorable for current drive by the LHW because fast electrons driven by the LHW take a longer time to slow down to thermal electrons and contribute to more plasma current. The higher fraction of high energy electrons can be confirmed by comparing the ratio of the SX radiation

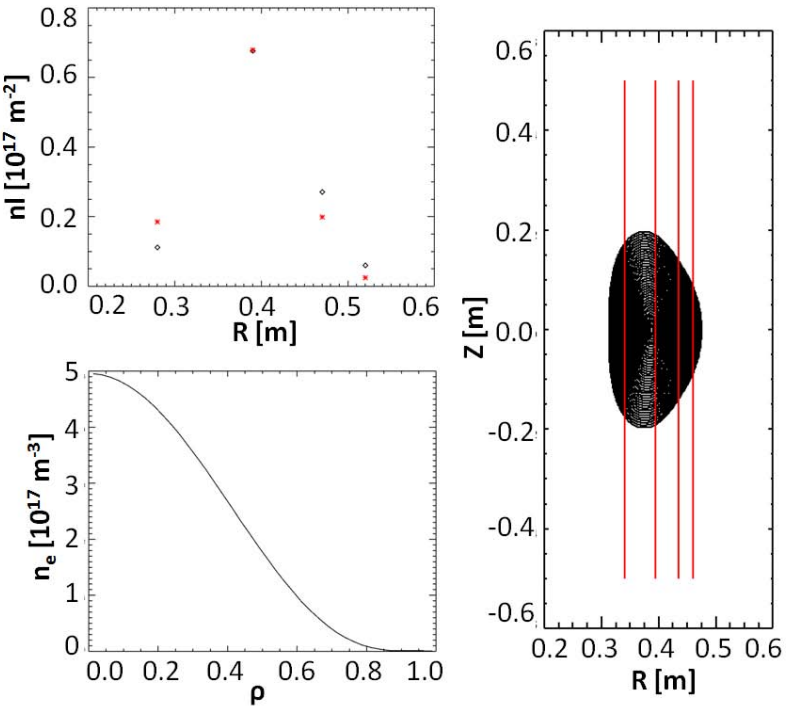

Figure 7.3: Reconstructed density profile.

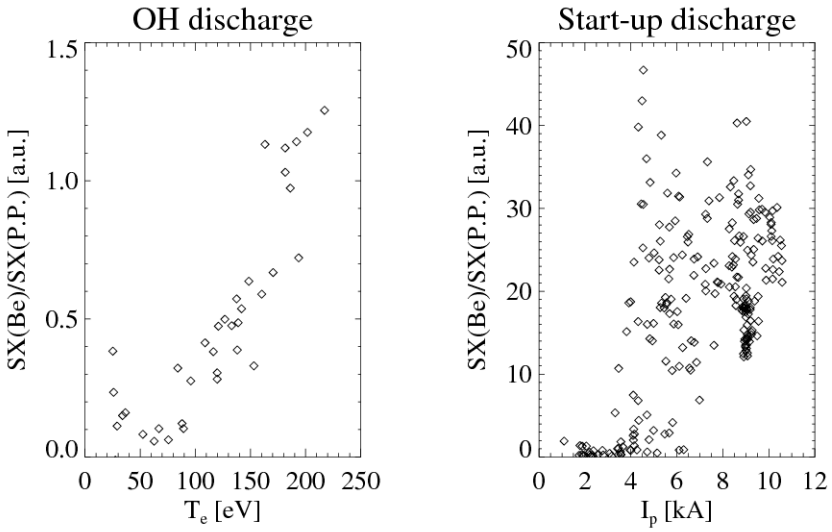

Figure 7.4: Comparison of the ratios of SX radiation strengths.

strengths in three energy ranges between the LHW start-up operation and the inductively sustained operation. As shown in Fig. 7.4, the fraction of the high energy component is higher in the LHW start-up operation.

7.2 Conclusions

An effective plasma current start-up to 15 kA using the LHW was demonstrated on the spherical tokamak. By keeping the plasma density sufficiently low, the problem of LHW accessibility could be avoided. Three types of antennas were used on TST-2 to investigate current drive by the LHW.

First of all, the combline antenna was used and achieved plasma current start-up to 15 kA. By changing the direction of current drive, it was revealed that the effect of direct RF current drive became significant when the plasma current exceeded 4 kA in TST-2. However, the current drive efficiency achieved using this antenna is lower than that obtained using the antennas used later because the polarization of the fields produced by this antenna is not suitable for exciting the LHW.

Next, the dielectric loaded grill antenna was used. This type of LHW launcher is widely used in tokamaks all over the world. A higher current drive efficiency was achieved compared to the combline antenna. This improvement could be attributed to the suitable polarization produced by this antenna. This antenna has the flexibility of changing the $n_{\parallel}$ of the launched

LHW. Therefore, the most efficient $n_{\parallel}$ for plasma current ramp-up for TST-2 was searched. Based on the achieved plasma current and the energy spectrum of the emitted X-rays, $n_{\parallel}$ of less than 6 was found to be favorable. However, the antenna-plasma coupling deteriorated non-linearly when the input power exceeded several kW. This deterioration is believed to be caused by the density depletion due to the ponderomotive force. This assumption was confirmed experimentally and theoretically. The actual density depletion when the input power exceeded several kW was measured by the electrostatic probe installed on the inner wall of the private limiter. The FEM antenna-plasma coupling simulation which takes into account the ponderomotive effect also shows the coupling deterioration due to density depletion. The reflection coefficient starts to increase at the same order of input powers as in the experiment assuming the plasma temperature is 5 – 10 eV, which is consistent with the temperature measured by the mid-plane Langmuir probe. The achieved plasma current using this antenna was restricted to under 10 kA because the coupled power was limited to under 35 kW due to the poor antenna-plasma coupling.

Lastly, the ECC antenna was used. This antenna solved the antenna-plasma coupling problem, and typical reflection coefficients of less than 10 % were achieved. A plasma current start-up to 12 kA was demonstrated using this antenna. The highest current drive figure of merit in TST-2 was achieved by this antenna. This is because the $n_{\parallel}$ spectrum of the LHW launched by the ECC antenna has a sharper peak than the grill antenna. In addition, the $n_{\parallel}$ spectrum of the grill antenna has the reverse going peak whose strength is one-third of the main peak while that of the ECC antenna is less than 5 %. These differences are the consequence of the difference in the number of antenna elements. The ECC antenna has 13 elements while the grill antenna has only 4. Therefore, the ECC antenna can launch a better defined traveling wave than the grill antenna. When the input power exceeded 30 kW, bursts in plasma density and H-α radiation due to impurity and/or neutral gas influx from the antenna were observed, and effective current drive has not been possible in this regime. An extensive antenna conditioning would be required to increase the input power while avoiding the problem described above. Plasma currents of more than 15 kA should be achievable with RF powers of greater than 50 kW delivered by the ECC antenna.

Acknowledgments

First of all, I would like to thank my supervisor, Professor Yuichi Takase for giving me the opportunity to learn a lot about plasma physics, especially the physics associated with waves in plasmas. I would also like to thank Professor Akira Ejiri for giving me many suggestions and advices. His profound insight helped me many times in plasma start-up experiments on TST-2. I would like to thank all of the members of Takase-Ejiri Laboratory, not only for cooperation in experiments but also for giving me many opportunities to have fun in daily life.

Next, I would like to thank some other collaborators who helped me. A special thanks goes to Dr. John Wright. His help on the TORLH simulation is essential for my thesis. Dr. Syunichi Shiraiwa and Dr. Orso Meneghini gave me many advises on the simulation using COMSOL. I would like to thank Dr. Charles Moeller for the collaborative research using the ECC antenna.

Finally, my deepest appreciation goes to my parents and my sister for their love and help. This thesis would not have been possible without their unconditional support.

Bibliography

[1] S. Bernabei, et al., Physical Review Letters **49**, 1255–1258 (1982).

[2] F. Jobes, et al., Physical Review Letters **52**, 1005–1008 (1984).

[3] Y. Takase, et al., Physics of Fluids **28**, 983 (1985).

[4] M. Mayberry, et al., Physical review letters **55**, 829–832 (1985).

[5] J. Wesson and D. Campbell, *Tokamaks*, Oxford University Press, USA (2004).

[6] J. Freidberg, *Plasma physics and fusion energy*, Cambridge Univ Pr (2007).

[7] H. Furth, Nuclear Fusion **15**, 487–534 (1975).

[8] L. Artsimovitch, Nuclear Fusion **12**, 215–252 (1972).

[9] Y. M. Peng and D. J. Strickler, Nuclear Fusion **26**, 769 (1986).

[10] M. Gryaznevich, et al., Physical review letters **80**, 3972 (1998).

[11] A. Sykes, et al., Plasma Physics and Controlled Fusion **39**, B247 (1997).

[12] R. J. Goldston and P. H. Rutherford, *Introduction to plasma physics*, CRC Press (2010).

[13] P. Bellan and M. Porkolab, Physical Review Letters **34**, 124–127 (1975).

[14] F. Leuterer, et al., Plasma Physics and Controlled Fusion **27**, 1399 (1985).

[15] K. Toi, et al., Physical review letters **52**, 2144 (1984).

[16] S. Kubo, et al., Physical Review Letters **50**, 1994 (1983).

[17] K. Ogura, et al., Nuclear Fusion **30**, 611 (1990).

[18] M. Porkolab, et al., Physical Review Letters **53**, 450–453 (1984).

[19] J. Wilson, et al., Nuclear Fusion **49**, 115015 (2009).

[20] Y. Peysson, et al., Plasma Physics and Controlled Fusion **42**, B87 (2000).

[21] T. Kondoh and t JT-60 Team, Physics of Plasmas **1**, 1489 (1994).

[22] A. Ekedahl, et al., Nuclear fusion **38**, 1397 (1998).

[23] G. Tonon, Plasma physics and controlled fusion **26**, 145 (1984).

[24] T. Yoshinaga, et al., Physical review letters **96**, 125005 (2006).

[25] H. Tanaka, et al., Production of high energy tail electrons by electron bernstein waves during the current start-up discharges in the late device, In *AIP Conference Proceedings* (2011).

[26] T. Yoshinaga, et al., Nuclear Fusion **47**, 210 (2007).

[27] M. Uchida, et al., Journal of Plasma and Fusion Research **80**, 83–84 (2004).

[28] T. Maekawa, et al., Nuclear fusion **45**, 1439 (2005).

[29] N. Fisch and A. Boozer, Physical Review Letters **45**, 720 (1980).

[30] T. Yamada, et al., Merging start-up experiments on the utst spherical tokamak, In *Proceedings of ITC19* (2009).

[31] R. Imazawa, et al., Electrical Engineering in Japan **179**, 20–26 (2012).

[32] R. Imazawa, et al., Electrical Engineering in Japan **179**, 18–24 (2012).

[33] R. Raman, et al., Physical review letters **97**, 175002 (2006).

[34] R. Raman, et al., Physical review letters **104**, 095003 (2010).

[35] R. Raman, et al., Nuclear fusion **45**, L15 (2005).

[36] R. Raman, et al., Nuclear Fusion **49**, 065006 (2009).

[37] V. Shevchenko, et al., Fusion science and technology **52**, 202–215 (2007).

[38] V. Shevchenko, et al., Nuclear Fusion **50**, 022004 (2010).

[39] I. B. Bernstein, Physical Review **109**, 10 (1958).

[40] W. Houlberg, et al., Physics of Plasmas **4**, 3230 (1997).

[41] O. Sauter, C. Angioni and Y. Lin-Liu, Physics of Plasmas **6**, 2834 (1999).

[42] S. Shiraiwa, et al., Physical review letters **92**, 035001 (2004).

[43] T. Stix, *Waves in plasmas*, Amer Inst of Physics (1992).

[44] M. Porkolab, et al. Collisional damping of the fast magnetosonic wave in the tokamak edge plasma. 1996.

[45] P. Bonoli, Plasma Science, IEEE Transactions on **12**, 95–107 (2007).

[46] M. Brambilla, Plasma Physics **18**, 669 (1976).

[47] T. Stix, Physical Review Letters **15**, 878–882 (1965).

[48] A. N. Kaufman, Physics of Fluids **15**, 1063 (1972).

[49] J. Wright, et al., Full wave simulations of lower hybrid wave propagation in tokamaks, In *AIP Conference Proceedings* (2009).

[50] R. Harvey and M. McCoy, *The cql3d fokker-planck code*, Advances in Simulation and Modeling of Thermonuclear Plasmas (1992).

[51] J. Wright, C. Phillips and P. Bonoli, Nuclear fusion **37**, 1349 (1997).

[52] Y. Takase, et al., Nuclear Fusion **41**, 1543 (2001).

[53] S. Von Goeler, et al., Nuclear Fusion **15**, 301–311 (1975).

[54] P. Brussaard and H. V. d Hulst, Reviews of Modern Physics **34**, 507–520 (1962).

[55] Ird inc. (http://www.ird-inc.com/axuvope.html).

[56] J. H. Hubbell and S. M. Seltzer. Tables of x-ray mass attenuation coefficients and mass energy-absorption coefficients 1 kev to 20 mev for elements z= 1 to 92 and 48 additional substances of dosimetric interest. 1995.

[57] C. Chantler, et al., *Detailed Tabulation of Atomic Form Factors, Photoelectric Absorption and Scattering Cross Section, and Mass Attenuation Coefficients for Z= 1–92 from E= 1–10 eV to E= 0.4–1.0 MeV, National Institute of Standards and Technology, Version 2.1, 2005*, physics. nist. gov/Phys RefData/FFast/Text/cover. htmlS (2005).

[58] M. Be, et al., *Update of X-ray and Gamma-ray Decay Data Standards for Detector Calibration and Other Applications*, International Atomic Energy Agency (2007).

[59] E. Browne and J. Tuli, Nuclear Data Sheets **108**, 2173–2318 (2007).

[60] M. Bhat, Nuclear Data Sheets **85**, 415–536 (1998).

[61] H. Koch and J. Motz, Reviews of Modern Physics **31**, 920–955 (1959).

[62] J. Stevens, et al., Nuclear fusion **25**, 1529 (1985).

[63] Comsol multiphysics. (http://www.comsol.com/).

[64] J. Sugiyama, et al., Plasma and Fusion Research **3**, 26–26 (2008).

[65] C. Forest, et al., Physics of Plasmas **1**, 1568 (1994).

[66] A. Ejiri and Y. Takase, Nuclear Fusion **47**, 403 (2007).

[67] C. B. Forest, et al., Phys. Rev. Lett. **68**, 3559–3562 (1992).

[68] R. Bickerton, J. Connor and J. Taylor, Nature **229**, 110–112 (1971).

[69] O. Watanabe, et al., Plasma and Fusion Research **3**, 49–49 (2008).

[70] O. Watanabe, et al., J. Plasma Fusion Res. **8**, 1040 (2009).

[71] A. Ejiri, et al., Nuclear Fusion **49**, 065010 (2009).

[72] I. H. Hutchinson, *Principles of plasma diagnostics*, Cambridge university press (2005).

[73] O. Meneghini. Full-wave modeling of lower hybrid waves on alcator c-mod. 2012.

[74] O. Meneghini, et al., Sol effects on lh wave coupling and current drive performance on alcator c-mod, In *AIP Conference Proceedings* (2011).

[75] J. R. Cary and A. N. Kaufman, Physics of Fluids **24**, 1238 (1981).

[76] S. Johnston and A. N. Kaufman, Physical Review Letters **40**, 1266 (1978).

[77] V. Chan and S. Chiu, Physics of Fluids **22**, 1724–1731 (1979).

[78] P. T. Bonoli and R. C. Englade, Physics of Fluids (1958-1988) **29**, 2937–2950 (1986).

[79] V. Petržilka, et al., Nuclear fusion **31**, 1758 (1991).

[80] A. Ekedahl, et al., Non-linear effects on the lh wave coupling in tore supra and impact on the lh current drive efficiency, In *AIP Conference Proceedings* (2009).

[81] M. Preynas, et al., Nuclear Fusion **53**, 013012 (2013).

[82] P. Jacquet, et al., Lhcd antenna coupling experiments on the tdev tokamak, In *AIP Conference Proceedings* (1996).

[83] C. Gormezano and D. Moreau, Plasma physics and controlled fusion **26**, 553 (1984).

[84] V. Pericoli-Ridolfini, Nuclear Fusion **31**, 351 (1991).

[85] A. Kaye, Plasma physics and controlled fusion **35**, A71 (1993).

[86] Y. Ikeda, et al., Fusion Engineering and Design **13**, 209–217 (1990).

[87] V. P. Ridolfini, et al., Nuclear fusion **45**, 1085 (2005).

[88] D. Bora, et al., Fusion engineering and design **82**, 141–152 (2007).